

Chiral control of spin-crossover dynamics in Fe(II) complexes

Malte Oppermann^{*1}, Francesco Zinna^{2,3}, Jérôme Lacour³, and Majed Chergui¹

¹Laboratoire de Spectroscopie Ultrarapide, École Polytechnique Fédérale de Lausanne, ISIC-FSB, 1015 Lausanne, Switzerland

²Dpto. di Chimica, Università di Pisa, Via Giuseppe Moruzzi 13, 56124 Pisa, Italy

³Département de chimie organique, Université de Genève, Quai Ernest Ansermet 30, 1211 Genève 4, Switzerland

*malte.oppermann@epfl.ch

ABSTRACT

Iron-based spin-crossover (SCO) complexes hold tremendous promise as multifunctional switches in molecular devices. However, real-world technological applications require the excited high-spin (HS) state to be kinetically stable – a feature that has only been achieved at cryogenic temperatures in the light-induced excited spin-state trapping effect. Here we demonstrate HS state trapping by controlling the chiral configuration of Fe^{II}(4,4'-dimethyl-2,2'-bipyridine)₃ in solution, associated for stereocontrol with enantiopure Δ - or Λ -TRISPHAT anions. We characterize the HS state relaxation using a newly developed ultrafast circular dichroism technique in combination with transient absorption and anisotropy measurements. We find that the decay of the HS state is accompanied by ultrafast changes of its optical activity, reflecting the coupling to a symmetry-breaking torsional twisting mode, contrary to the commonly assumed picture. Furthermore, we show that the diastereoselective ion-pairing with the enantiopure anions suppresses the vibrational population of the identified twisting mode, thereby achieving a four-fold extension of the HS lifetime. Transferred to the solid state, this novel strategy may thus significantly improve the kinetic stability of iron(II)-based magnetic switches at room temperature.

1 The exquisite magnetic switching capabilities of transition metal complexes with energetically close-lying
2 spin states are highly attractive for technological applications in information storage and processing¹.
3 In this respect, Fe^{II}-based polypyridine complexes are particularly promising, due to their low cost
4 and toxicity, earth-abundance, rich photochemistry and an efficient spin-crossover (SCO) transition that
5 can be triggered by various external stimuli including light, pressure and temperature². However, the
6 excited paramagnetic spin states are notoriously short-lived at room temperature, which limits their use in
7 molecular devices³.

8 The tris-chelate iron(II)tris(bipyridine) ([Fe^{II}(bpy)₃]²⁺) has emerged as a prototypical model complex,
9 whose light-induced SCO mechanism serves as a reference for assessing the spin-switching dynamics of
10 other Fe^{II} complexes⁴. To this end, ultrafast spectroscopies in the optical^{5–8} and X-Ray domain^{9–13} have
11 determined that the initially excited singlet metal-to-ligand charge-transfer (MLCT) state is deactivated

12 in <50 fs with near unity efficiency via an essentially barrierless passage through the triplet MLCT and
13 metal-centered (MC) states to the lowest-energy MC 5T_2 state. The latter high-spin (HS, $S = 2$) state
14 then converts back to the low-spin (LS, $S = 0$) 1A_1 ground state on the sub-nanosecond scale in aqueous
15 solution. As the forward-SCO involves the transfer of two electrons from formally non-bonding t_{2g}
16 to antibonding e_g ligand-field orbitals, the resulting weakening and elongation of the Fe-N bonds by
17 approximately 0.2 Å has been established as the dominant reaction coordinate of the SCO³. Indeed, a
18 so-called single reaction coordinate model has been proposed for Fe^{II}-SCO complexes, describing the
19 non-radiative $^5T_2 \rightarrow ^1A_1$ back-SCO in a framework akin to semi-classical Marcus theory^{14,15}, with the
20 structural re-organization proceeding via a symmetric breathing mode of the Fe-N bonds and the electronic
21 coupling mediated by the (thermally inaccessible) 3T_1 state. In this picture, thermal HS deactivation
22 is suppressed at sufficiently low temperatures, famously known as the light-induced spin-state trapping
23 (LIESST) effect¹⁶.

24 However, it is now well established that the single reaction coordinate model fails to describe the SCO
25 dynamics of Fe^{II} systems with constrained ligand systems, where anisotropic expansions of the Fe-N bond
26 network couple to dynamic angular distortions of the primary coordination sphere^{4,13,17-20}. Importantly,
27 it has been suggested that it is precisely the *deviations* from a single active Fe-N breathing coordinate that
28 may provide a route to spin-state trapping at room temperature, as the coupling of the spin-relaxation
29 to a distorted coordination environment can be manipulated through the mechanical properties of the
30 ligand system^{21,22}. Perhaps surprisingly, it has long been speculated that such distortions may also play
31 a role in the SCO mechanism of unconstrained tris-chelate complexes, such as $[Fe^{II}(bpy)_3]^{2+}$, due to a
32 fundamental link between the SCO process and their chiral three-bladed propeller structure: the entropy-
33 driven racemization of enantiopure or enantioenriched solutions at room temperature (RT) is accompanied
34 by a change in spin-state²³. This was rationalized at the end of the 1970s through calculations by Purcell
35 and Vanquickenborne^{24,25}, showing that the low-frequency torsional twisting modes associated with the
36 racemization result in a surface crossing of the 1A_1 and 5T_2 states, whilst stabilizing the 3T_1 state and
37 thus increasing the associated spin-orbit coupling term. However, despite an early synthetic design study
38 correlating the HS deactivation barrier with the flexibility of a hexadentate ligand framework along a
39 torsional twisting coordinate²⁶, conclusive experimental evidence for the fundamental role of this reaction

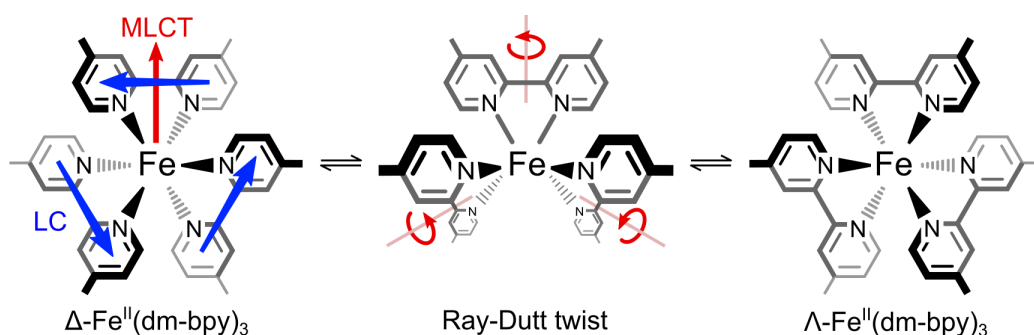


Figure 1. Due to the lability of its Fe-N bonds, an enantiomerization of the Λ and Δ configurations of $\text{Fe}^{\text{II}}(\text{dm-bpy})_3$ occurs in solution via the intramolecular Ray-Dutt twist.

Molecular structure of $\Lambda, \Delta\text{-Fe}^{\text{II}}(\text{dm-bpy})_3$, including its metal-to-ligand charge transfer (MLCT) and ligand-centred (LC) long-axis $\pi\pi^*$ transition dipoles. The Ray-Dutt twist proceeds via a transition state structure with C_{2v} symmetry.

40 coordinate in Fe^{II} -based SCO complexes is still lacking.

41 In this study we reverse the perspective developed by Purcell and Vanquickenborne and investigate
 42 whether suppressing the enantiomerization of $[\text{Fe}^{\text{II}}(\text{dm-bpy})_3]^{2+}$ (dm-bpy = 4,4'-dimethyl-2,2'-bipyridine)
 43 in RT solutions kinetically stabilizes the HS state. Fig. 1 displays the chiral structure of the three-bladed
 44 propeller complex with Λ and Δ configurations and the transition dipoles for its singlet MLCT and
 45 ligand-centered (LC) long-axis $\pi\pi^*$ transitions. As other hexacoordinated tris-chelate complexes, the
 46 enantiomerization process may proceed via two possible non-dissociative pathways, which pass through
 47 trigonal prismatic transition states with different symmetries: the Bailar twist via a D_{3h} and the Ray-Dutt
 48 twist via a C_{2v} symmetry (see fig. 1). Whilst the dominant mechanism depends on both the metal center
 49 and the ligand system, a recent DFT study on $[\text{Fe}^{\text{II}}(\text{bpy})_3]^{2+}$ found the Ray-Dutt twist to be energetically
 50 favorable, both on the singlet and the quintet surface²⁷. Due to the lability of the Fe-N bonds, torsional
 51 twists have a low kinetic barrier in RT solutions, resulting in the formation of racemic mixtures with
 52 equal amounts of Λ and Δ enantiomers and no detectable optical activity. However, diastereomeric
 53 interactions with enantiopure counterions (TT = TRISPHAT, Λ - or Δ -enantiomers) are known to shift the
 54 configurational equilibrium: $\text{Fe}^{\text{II}}(\text{dm-bpy})_3(\Lambda\text{- or } \Delta\text{-TT})_2$ dissolved in the apolar CHCl_3 forms contact ion
 55 pairs (CIP) with preferential homochiral association, e.g. $\Delta^+(\Delta^-)_2$, leading to very high diastereomeric
 56 excess ($de > 96\%$) over any heterochiral $\Lambda^+(\Delta^-)_2$ pairs present in the solution^{28,29}. We compare the
 57 SCO dynamics of this sample (Fe^{CIP}) to two reference systems: 1) $\text{Fe}^{\text{II}}(\text{dm-bpy})_3(\Lambda\text{- or } \Delta\text{-TT})_2$ dissolved

58 in the more polar CH_2Cl_2 (Fe^{SIP}), which forms a large proportion of solvent-separated ion pairs (SIP)
59 with, consequently, a reduced diastereomeric interaction ($de \approx 68\%$)³⁰, and 2) $\text{Fe}^{\text{II}}(\text{dm-bpy})_3(\text{PF}_6)_2$ in
60 CH_2Cl_2 (Fe^{RIP}), which forms racemic ion-pairs (RIP) with the achiral PF_6 anions. The sample synthesis
61 is described in the Methods section.

62 It has been well established that photoexcitation of the HS state red-shifts the LC absorption band of
63 the complex, providing an unambiguous spectroscopic signature of the HS state and therefore a probe of
64 the SCO dynamics in the deep ultraviolet (UV) region (270-350 nm)^{7,8}. Through a unique combination
65 of ultrafast spectroscopic techniques in the deep-UV, we now exploit the polarization sensitivity of the
66 LC transition dipoles in the HS state to directly resolve the structural mechanism of the back-SCO and
67 its chiral control through the diastereomeric ion-pairing interaction. The associated optical setups and
68 measurement conditions are described in the Methods section. We first establish a four-fold extension
69 of the HS lifetime of Fe^{CIP} compared to the racemic ion-pair Fe^{RIP} using ultrafast broadband transient
70 absorption (TA). Second, we use transient absorption anisotropy (TAA) to extract the conformational
71 ensemble of the ligands, showing that the diastereomeric ion-pairing strongly narrows the width of their
72 angular distribution around an ideal octahedral configuration. Finally, we employ a newly developed
73 time-resolved circular dichroism (TRCD) technique with artifact-free broadband deep-UV detection^{31,32},
74 delivering an unprecedented absolute sensitivity of $\pm 1 \cdot 10^{-5}$ OD. This breakthrough opens the avenue to
75 spectrally resolve the excited state CD of photochemical systems in solution and to track its evolution with
76 sub-picosecond resolution.

77 In this study we apply these novel capabilities to extract the excited state CD of the HS state and
78 the structural dynamics it encodes. We identify the Ray-Dutt twist as a key reaction coordinate for the
79 back-SCO, driving an asymmetric distortion of the Fe^{II} -centered coordination sphere on the picosecond
80 time scale. Accounting for the TA and TAA experiments, we correlate the intrinsic rate of the distortion
81 with the intersystem crossing rate to the ground state and the lability of the metal-ligand bonds. We
82 thus find that the diastereomeric ion-pairing traps the HS state by cooling the vibrational population of
83 the Ray-Dutt twist. Quite remarkably, this highlights the central importance of the associated torsional
84 distortion in the back-SCO of Fe^{II} complexes and implies that even in the prototypical $[\text{Fe}^{\text{II}}(\text{bpy})_3]^{2+}$
85 more than a single active reaction coordinate is needed to fully describe its SCO mechanism.

86 Results

87 Chiral Fe^{II} complexes

88 The three investigated samples display qualitatively similar steady-state absorption spectra (for details
89 see section S.1 in the Supplementary Information) with a strong band near 295 nm consisting of LC
90 $\pi\pi^*$ transitions and a weaker MLCT band near 500 nm (see fig. S.1). Both bands display a double
91 peak structure, which in the LC region is most pronounced for the racemic ion-pair Fe^{RIP} and has been
92 attributed to a vibrational progression localized on the ligands^{33,34}. The deep-UV CD spectra of Fe^{CIP} and
93 Fe^{SIP} (fig. S.2) display a characteristic bisignate structure resulting mostly from the excitonically coupled
94 long-axis LC transitions, with the expected sign inversion for the Λ and Δ configurations^{35,36}. A spectral
95 decomposition of the CD spectra (fig. S.3) shows that changing the solvent from CHCl₃ to CH₂Cl₂ for
96 Fe^{II}(dm-bpy)₃(Λ - or Δ -TT)₂ leads to a minor hypsochromic shift and a global reduction of the molar
97 ellipticity with an enhanced suppression of the high-energy CD band centred near 285 nm.

98 In the following we monitor different aspects of the back-SCO mechanism. We track the population
99 dynamics of the HS state with TA and measure the linear dichroism of the photoexcited molecular
100 ensemble with TAA. Note that TAA tracks the spatial distribution of LC transition dipoles in the HS
101 state as a function of time, thus encoding the conformational ensemble of the ligands. Furthermore, we
102 measure the chiral properties of excited HS state with TRCD, which is sensitive to changes in the excitonic
103 coupling of the LC transition dipoles in the photoexcited complex. It is thus possible to directly resolve
104 the structural changes that drive the relaxation dynamics of the HS state.

105 Transient absorption

106 Fig. 2a displays the TA spectrum of Λ -Fe^{CIP} following MLCT excitation at 530 nm as a function of
107 pump-probe delay. A pronounced ground state bleach (GSB) band centered at 295 nm takes the inverted
108 shape of the steady-state absorption spectrum and overlaps with an excited state absorption (ESA) band
109 centred at 315 nm. This ESA band has previously been identified as the red-shifted LC absorption of
110 the photoexcited complex in its HS state and has been well-established as a marker for its electronic
111 and vibrational relaxation dynamics^{7,8}. To this end, fig. 2b displays the TA amplitude as a function of
112 pump-probe delay for the HS absorption and the GSB bands near the spectral positions indicated by the

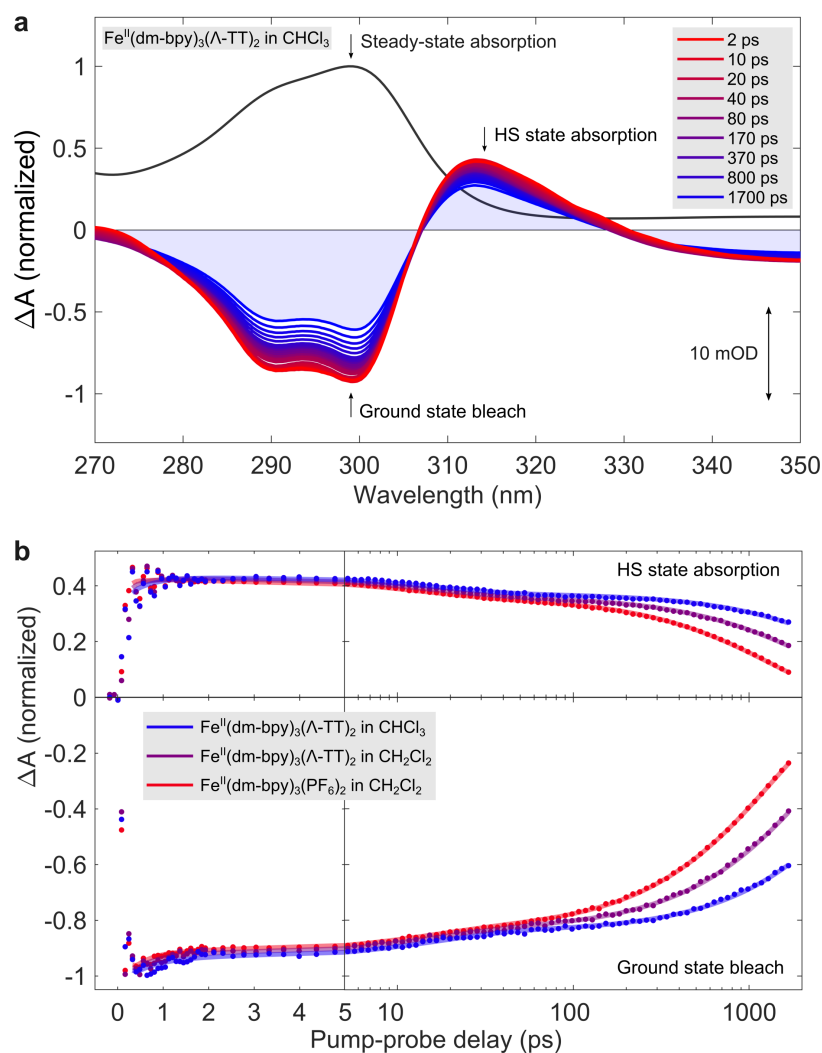


Figure 2. Transient absorption measurements show that diastereoselective ion-pairing extends the high-spin state lifetime of $\text{Fe}^{\text{II}}(\text{dm-bpy})_3$. **a**, Deep ultraviolet steady-state and transient absorption of the ligand-centered transitions of the homochiral contact ion-pair $\text{Fe}^{\text{II}}(\text{dm-bpy})_3(\Lambda\text{-TT})_2$ involving enantiopure counterions in CHCl_3 after photoexcitation of its MLCT transition at 530 nm. The probed spectral region simultaneously resolves the spectral fingerprints of the ground state bleach and the excited high-spin (HS) state. **b**, Multi-exponential HS state decay (top panel) and simultaneous ground state recovery dynamics (bottom panel) for ion-pairs with successively reduced diastereoselectivity: homochiral contact ion-pairs with maximum selectivity (blue), large proportion of separated ion-pairs in CH_2Cl_2 with reduced selectivity (purple), and racemic ion-pairs with achiral counterions in CH_2Cl_2 (red). To improve the visibility of the data, the vertical trace positions have been minimally adjusted and some data points at negative time delays have been omitted (the original traces are shown in the SI). A global analysis (solid lines) of the data (solid dots) determines an extension of the HS state lifetime to 5.0 ns in the contact ion-pair compared to 2.4 ns in the separated and 1.3 ns in the racemic ion-pair.

113 arrows in fig. 2a for Fe^{CIP} , Fe^{SIP} , and Fe^{RIP} . Note that the spectral positions were adapted to the band
 114 positions in each sample as indicated in fig. S.8 in the SI. We now observe a pronounced impact of the

115 ion-pairing interaction on the TA kinetics: the HS state lives longest in Fe^{CIP} with successively shorter
116 lifetimes for Fe^{SIP} and Fe^{RIP}. We quantified the dynamics through a detailed spectro-kinetic analysis
117 presented in section S.2, assuming a sequential decay model with three exponential components. For each
118 sample, the HS state decay is dominated by the slowest component τ_3 , with $\tau_3^{\text{CIP}} = 4970 \pm 50$ ps for Fe^{CIP},
119 $\tau_3^{\text{SIP}} = 2370 \pm 20$ ps for Fe^{SIP}, and $\tau_3^{\text{RIP}} = 1330 \pm 10$ ps for Fe^{RIP}. The complete set of time constants is
120 listed in table S.3, along with the decay constants obtained from the TAA and TRCD experiments.

121 **Transient anisotropy**

122 Fig. 3 displays the TAA measured for all three samples as a function of the pump-probe delay near the
123 spectral positions corresponding to the TA kinetic traces presented in fig. 2b (the sample-adapted positions
124 are displayed in fig. S.12 in the SI). In the HS absorption region, TAA probes the relative orientation of
125 LC transition dipoles in the HS state with respect to the initially excited MLCT transition. The initial TAA
126 value r_0 at the earliest pump-probe delay displays a pronounced dependence on the ion-pairing interaction:
127 the lowest value is obtained for $r_0^{\text{CIP}} = -0.96$, compared to $r_0^{\text{SIP}} = -0.87$ and $r_0^{\text{RIP}} = -0.66$. The TAA
128 of the samples converges to zero on the 100 ps time scale with increasingly faster kinetics going from
129 Fe^{CIP} to Fe^{SIP} and Fe^{RIP}. Similar observations can be made for the TAA in the GSB region, however the
130 differences in the initial TAA values are less pronounced and an additional decay component on the 10 ps
131 scale is clearly visible.

132 As TA bands typically contain contributions from different transition dipoles, the TAA across each
133 TA band may vary strongly. In addition, zero crossings between GSB and ESA bands cause the TAA to
134 diverge to infinity (see mathematical definition in Methods), which may distort the observed TAA kinetics.
135 Fig. S.10 in the SI therefore displays the spectrally resolved TAA data for all three samples. Just as the TA
136 spectrum, the TAA spectrum in the GSB region <295 nm is composed of two bands with slightly different
137 amplitudes. In the HS state absorption band no significant spectral variation can be observed, other than
138 the divergence near its zero crossings. Both the presence of several transition dipoles and the dynamic
139 changes of the TAA divergence near zero-crossings may be obscured in the TAA kinetics obtained from
140 single-wavelength traces. Through suitably adapted global fits (for details see section S.3 in the SI), we
141 found that the broadband data can be adequately fit with a minimum number of two exponential decays, in

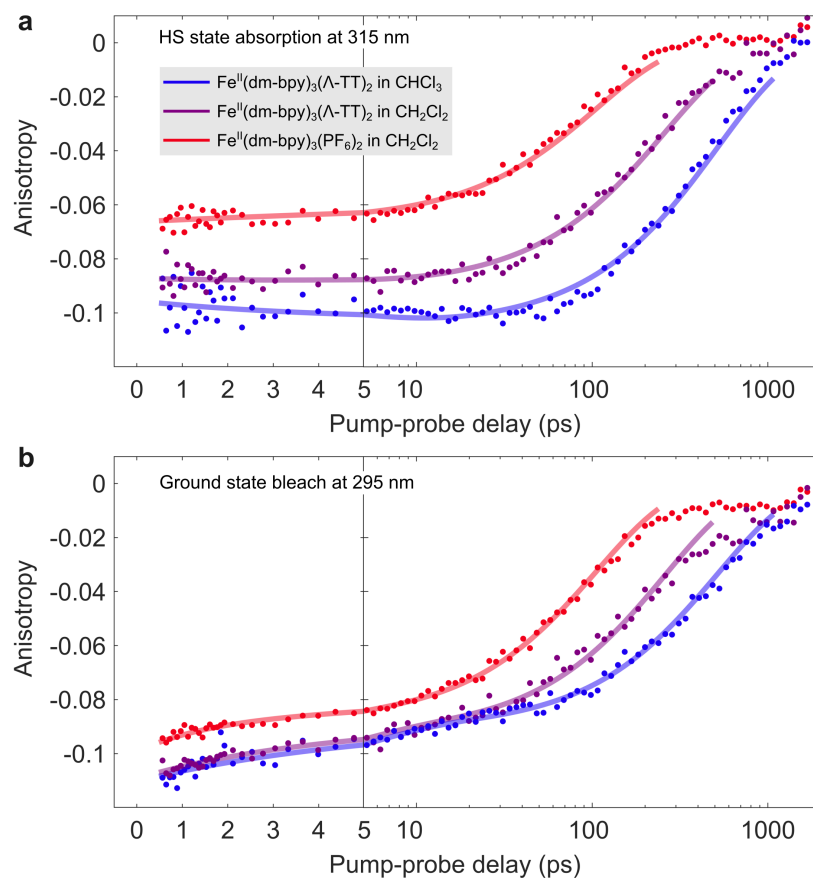


Figure 3. Transient absorption anisotropy experiments correlate the diastereoselective interaction with the conformational flexibility of $\text{Fe}^{\text{II}}(\text{dm-bpy})_3$'s ligand system. **a,b** Transient absorption anisotropy after photoexcitation of the MLCT band at 530 nm as a function of the pump-probe delay in the HS state absorption (a) and ground state bleach region (b), as indicated in fig. 2a, for the contact (blue), the separated (purple), and the racemic ion-pair (red). Model calculations (see SI) correlate the measured initial anisotropy of the HS state (<1 ps) with the width of the ligand system's conformational ensemble and find that the contact pair has a near-rigid octahedral ligand configuration with a three-times narrower conformational ensemble compared to the racemic pair. A global analysis of the multi-exponential anisotropy decays extracts picosecond structural dynamics in each sample's conformational ensemble and a characteristic rotational diffusion time as a global decay to zero. We observe that both processes are slowed down with increasing diastereoselective interaction.

142 line with the qualitative observations made above. With the time constants separated by more than an order
 143 of magnitude, both a sum and a sequential series of exponential functions can be employed to fit the data,
 144 resulting in identical time constants and exponential pre-factors for each sample. Fig. S.11 therefore only
 145 reports the results from the sequential model, whereas fig. S.12 shows the corresponding residuals. The
 146 exponential fits are included as solid lines in fig. 3 and display a very good correspondence with the data.
 147 The global analysis shows that the TAA dynamics across the chosen probe window can be described by

148 the same two exponential processes, independent of the spectral position within the HS absorption or GSB
149 band. For Fe^{CIP}, we obtained the time constants $\rho_1^{\text{CIP}} = 4.8 \pm 0.2$ ps and $\rho_2^{\text{CIP}} = 520 \pm 10$ ps. The shorter
150 constant displays a minor amplitude across the probed spectral range and causes the TAA to decrease in
151 the HS absorption band and to increase in the GSB band. The TAA then converges globally to zero with
152 the longer time constant. Again, whilst qualitatively similar signatures are observed for Fe^{SIP} and Fe^{RIP},
153 the ion-pairing interaction has a clear impact on their relative amplitudes and time scales: both processes
154 become gradually faster for Fe^{SIP} and Fe^{RIP}, whereas the contribution of ρ_1 is successively decreased - as
155 can be observed in the DAS and SAS in fig. S.11. For the time constants, we obtained $\rho_1^{\text{SIP}} = 3.6 \pm 0.2$ ps
156 and $\rho_2^{\text{SIP}} = 260 \pm 10$ ps for Fe^{SIP}, and $\rho_1^{\text{RIP}} = 1.6 \pm 0.2$ ps and $\rho_2^{\text{RIP}} = 110 \pm 10$ ps for Fe^{RIP}.

157 Time-resolved circular dichroism

158 We conducted TRCD experiments on Fe^{CIP} and Fe^{SIP} in both their Λ and Δ configurations and fig. 4a
159 shows the time evolution of Λ -Fe^{CIP} as an example, while the complete data sets are displayed in fig. S.17.
160 The excellent signal-to-noise enables a detailed spectral analysis of the TRCD kinetics. Analogous to
161 TA, the sign-inverted steady-state CD of the sample will appear in the TRCD spectrum as a GSB feature
162 superimposed with the CD spectrum of the photoexcited HS state. However, whilst the decay of the GSB
163 has to follow the ground state recovery dynamics observed in TA, the time evolution of the HS CD will
164 also encode structural changes in the excited state. We thus identify GSB bands centered at 285 nm and
165 305 nm and a positive HS CD band near 315 nm. In addition, the low initial amplitude of the GSB band
166 at 285 nm compared to the steady-state CD and its weak decay dynamics suggest the presence of an
167 overlapping HS CD band with a negative amplitude. In Λ -Fe^{SIP} (fig. S.17c), the same spectral features
168 are observed, yet with a faster global decay and a pronounced decay in the high-energy GSB band near
169 285 nm. Importantly, we observe identical spectral dynamics with an inverted sign in the respective Δ
170 configurations (fig. S.17b,d), demonstrating the consistency of the results.

171 We extracted the temporal evolution of the HS CD through a global fitting procedure (see Methods),
172 showing that only two Gaussian HS CD bands with constrained fit parameters are needed to fit all data
173 sets (for details see section S.4 in the SI). Fig. 4b displays the obtained time evolution of the HS CD
174 for Λ -Fe^{CIP} and $-\text{Fe}^{\text{SIP}}$, with fig. S.20 showing the associated residuals and the results obtained for the Δ

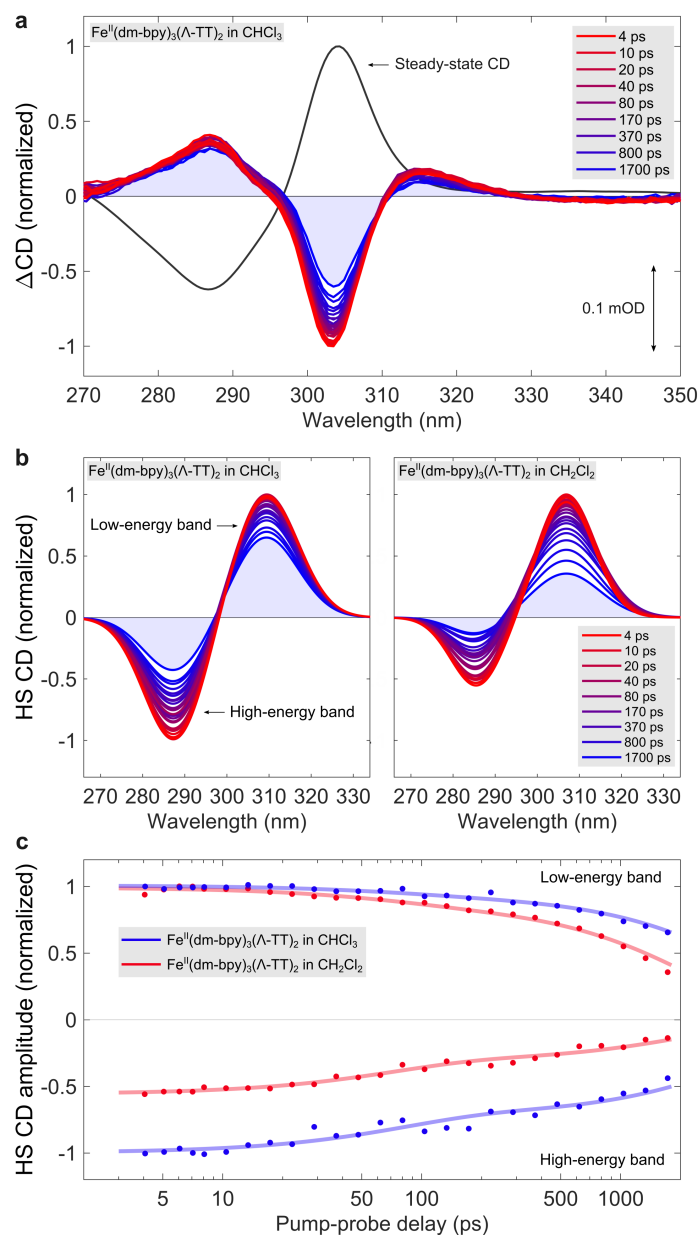


Figure 4. Time-resolved circular dichroism (CD) resolves an asymmetric decay of the high-spin state CD of $\text{Fe}^{\text{II}}(\text{dm-bpy})_3$, indicating a symmetry-breaking structural distortion. **a**, Steady-state and time-resolved CD of the ligand-centered transitions of the homochiral contact ion-pair $\text{Fe}^{\text{II}}(\text{dm-bpy})_3(\Delta\text{-TT})_2$ in CHCl_3 after MLCT excitation at 530 nm. Ground state bleach bands near 285 nm and 305 nm overlap with the CD spectrum of the excited HS state, with a positive band emerging near 315 nm. **b**, We extracted the temporal evolution of the HS state's excitonic CD via a constrained global fit (for details see text and SI): in the contact ion-pair (left) an asymmetric decay of the HS CD bands strongly suppresses its high-energy band, whereas the separated ion-pair in CH_2Cl_2 (right) shows a similar, yet significantly enhanced effect. **c**, Normalized HS CD band amplitudes as a function of pump-probe delay. A double exponential fit (solid line) shows that the low-energy band mostly decays with the excited state population, whereas the high-energy band requires an additional 70 ps component, whose contribution is $\sim 28\%$ in the contact and $\sim 43\%$ in the separated ion-pair.

175 configurations. In all cases, the bisignate HS CD bands follow the sign inversion of the steady-state CD,
176 as expected from the chiral ligand framework. For Fe^{CIP} , the band amplitudes are mostly identical at early
177 times, yet for increasing pump-probe delays the high-energy band decays more strongly, resulting in a
178 significant reduction of the band ratio. For Fe^{SIP} , the reduced contact ion-pairing interaction enhances
179 these effects: already at the earliest pump-probe delay, the high-energy band is much weaker than the
180 low-energy band and its amplitude is suppressed more strongly with increasing pump-probe delay. In
181 addition, a slight broadening of the low-energy band is observed. We thus note that the spectral evolution
182 of the HS CD is dominated by an asymmetric decay of its bands, which is significantly more pronounced
183 in Fe^{SIP} compared to Fe^{CIP} .

184 To quantify the decay kinetics, fig. 4c plots the normalized band amplitudes as a function of pump-
185 probe delay. For both samples, the low-energy band decays nearly mono-exponentially, whereas an
186 additional decay component on the 10 ps scale is clearly observed for the high-energy band. We thus
187 simultaneously fitted the time evolution of the high- and low-energy band amplitudes with a sum of two
188 exponential decays and accounted for the decay of the excited state population by setting one of the time
189 constants to τ_3 , the longest decay constant obtained from the TA experiments. The fit curves are the solid
190 lines in fig. 4c and are in excellent agreement with the data (see residuals in fig. S.22). The obtained
191 fit parameters are displayed in table S.5 in the SI and reveal a decay component ϕ on the picosecond
192 scale that is neither observed in the TA, nor in the TAA dynamics and takes the values $\phi^{\text{CIP}} = 70 \pm 10$
193 ps and $\phi^{\text{SIP}} = 80 \pm 10$ ps for Fe^{CIP} and Fe^{SIP} , respectively. Whilst the time constants agree within their
194 error ranges, their contribution to the decay of the high-energy HS CD band amplitude depends on the
195 ion-pairing interaction: in Fe^{CIP} , the picosecond component contributes $\sim 28\%$ to the total decay, whereas
196 in Fe^{SIP} this contribution is found to be $\sim 43\%$. In the low-energy HS CD band, the contribution of the
197 picosecond component accounts for $\sim 10\%$ of the decay dynamics in both samples, implying that this
198 band mostly decays as the excited state population.

199 Discussion

200 The diastereomeric interactions with either Λ - or Δ -TT counterions shift the configurational equilibrium
201 of Λ - and Δ - $\text{Fe}^{\text{II}}(\text{dm-bpy}_3)$ enantiomers towards the thermodynamically favorable homochiral Λ - $\text{Fe}^{\text{II}}(\text{dm-}$

202 $\text{bpy})_3(\Lambda\text{-TT})_2$ or $\Delta\text{-Fe}^{\text{II}}(\text{dm-bpy})_3(\Delta\text{-TT})_2$ pairs³⁷: whilst Fe^{RIP} is racemic, the homochiral ion-pairs
203 $\Lambda, \Delta\text{-Fe}^{\text{CIP}}$ and $-\text{Fe}^{\text{SIP}}$ display a strong CD. Reddy *et al.*³⁰ have determined that changing the solvent from
204 CHCl_3 to CH_2Cl_2 reduces the diastereomeric excess of homo- over heterochiral ion-pairs from >96% to
205 approximately 68%. This is reflected in the reduction of the molar ellipticity of Fe^{SIP} compared to Fe^{CIP} ,
206 which is larger than the observed reduction in the associated molar extinction of the LC transitions. In
207 the less polar CHCl_3 (dielectric constant $\epsilon = 4.81$), the association with fluorinated TT counterions has
208 further shown that Fe^{CIP} is best described as a supramolecular complex with contact ion-pairing along the
209 C_3 axis of the Fe^{II} complex²⁹. However, due to a large degree of solvent-separated ion-pairing in the more
210 polar CH_2Cl_2 ($\epsilon = 8.93$) of Fe^{SIP} , we cannot exclude the presence of structurally different supramolecular
211 complexes, i.e. in the form of heterochiral ion-pairs with a less efficient pairing interaction along the
212 C_2 axes³⁸. However, in all reported experiments, Fe^{SIP} displays the same qualitative spectral kinetics as
213 Fe^{CIP} , suggesting equivalent excited state evolution without any evidence for the presence of additional,
214 differently behaved species. We therefore assume that the higher proportion of heterochiral ion-pairs in
215 Fe^{SIP} displays the same electronic and mechanical properties as their homochiral counterparts, consistent
216 with a simple inversion of the chiral structure of the Fe^{II} complex within the ion-pair.

217 Through comparison with the well-characterized case of $\text{Fe}^{\text{II}}(\text{bpy})_3\text{Cl}_2$ in H_2O (see details in section S.2
218 in the SI), we directly assign the TA decay components τ_2 and τ_3 to the vibrational cooling and electronic
219 decay of the HS state, respectively (the time constants obtained from all time-resolved experiments are
220 listed in table S.3). Consequently, we can infer that the diastereomeric ion-pairing slows down both the
221 vibrational cooling and the electronic decay of the HS state, whereas the latter effect is more strongly
222 pronounced with a four-fold lengthening of the HS state lifetime when comparing Fe^{CIP} to Fe^{RIP} . In
223 this respect, the chosen series of investigated samples rules out simple solvation effects as the dominant
224 cause: Fe^{RIP} and Fe^{SIP} have the same solvation environment, yet display strikingly different HS state
225 dynamics. Whilst the much larger $\Lambda\text{-TT}$ counterions may provide some shielding from the solvent, we
226 note that this effect is minimized by the solvent-separated ion-pairing in CH_2Cl_2 . This is consistent with
227 recent findings by Miller and McCusker³⁹ who found no significant difference in the HS state lifetime of
228 $[\text{Fe}^{\text{II}}(\text{bpy})_3]^{2+}$ paired with differently sized counterions in acetonitrile. The same study reports relatively
229 small variations in the HS state lifetime with respect to the solvent polarity such that direct solvation

230 differences are insufficient to explain the HS lifetimes obtained for Fe^{SIP} and Fe^{CIP}. Instead, we conclude
231 that the diastereomeric interaction with Λ, Δ -TT controls the excited state lifetime through the manipulation
232 of ligand system's configurational flexibility. This is a natural choice, since the enantiomerizing motion
233 of the ligands is known to increase the spin-orbit coupling through the accompanying distortion of the
234 metal-centered coordination sphere.

235 Concerning the vibrational cooling, we note that the rapid ¹MLCT–³MLCT–³MC–⁵T₂ SCO cascade
236 leaves the HS state with approximately 1.3 eV excess vibrational energy. Intramolecular vibrational energy
237 redistribution (IVR) coupled to energy dissipation to the solvent then traps the HS state in a minimum
238 energy conformation. It is well-established that the forward-SCO impulsively excites the totally symmetric
239 breathing mode of the Fe-N bonds and local ligand bending and stretching modes^{7,8,13,17}. The observed
240 vibrational cooling times, with $\tau_2^{\text{CIP}} > \tau_2^{\text{SIP}} > \tau_2^{\text{RIP}}$, therefore indicate that the diastereomeric ion-pairing
241 decelerates the IVR process, most likely by reducing the anharmonic coupling terms through a reduced
242 flexibility of the ligand system⁴⁰.

243 The TAA experiments now enable a direct assessment of the ligand system's mechanical properties,
244 as the measured spatial distribution of LC transition dipoles encodes the conformational ensemble of
245 the ligands. To this end, photoexcitation of the isotropic sample in solution preferentially selects MLCT
246 transition dipoles aligned parallel to the pump laser polarization. This creates an ensemble of excited
247 molecules that is partially aligned within the laboratory frame of reference, following a $\cos^2 \alpha$ distribution,
248 where α denotes the angle between the selected MLCT transition dipole and the pump polarization axis.
249 TAA in the deep-UV then measures the relative orientation of the bleached ground state and excited
250 HS state LC transition dipoles. Assuming an octahedral complex structure, a long-axis LC transition
251 associated with the same ligand as the excited MLCT transition will result in the minimum anisotropy
252 value of $r = -0.2$ due to its perpendicular arrangement, whereas the remaining two ligands each result in
253 $r = -0.05$ ⁴¹. Due to the back-electron transfer involved in forming the HS state, the three ligands become
254 indistinguishable, such that the measured TAA in a rigid octahedral structure takes the average value
255 $\langle r \rangle = -0.1$. In order to correlate the experimental TAA with the conformational lability of the metal-ligand
256 bonds, we introduced two spatial degrees of freedom in the calculation of the average anisotropy: a
257 rotation angle θ of each ligand around the metal-ligand bond and a rotation around the metal-center in

258 the ligand plane by an angle δ . Note that $\theta = \delta = 0^\circ$ corresponds to the octahedral configuration. In
259 section S.3 we calculated $\langle r \rangle$ as a function of the standard deviation σ of a two-dimensional Gaussian
260 distribution over both rotational degrees of freedom. The results are displayed in fig. S.13 and demonstrate
261 that the value $\langle r \rangle = -0.1$, obtained for a rigid ligand system with $\sigma = 0^\circ$, is the minimum possible TAA
262 value, whereas any broadening of the ligands' conformational distribution leads to an increase of $\langle r \rangle$. The
263 observed decrease in initial TAA values in the HS state absorption region, $r_0^{\text{RIP}} > r_0^{\text{SIP}} > r_0^{\text{CIP}}$, therefore
264 shows that the diastereomeric ion-pairing interaction narrows the conformational distribution of the ligands
265 around an octahedral structure of the complex, thereby counteracting the lability of the metal-ligand bonds.
266 From the model calculations we obtained the standard deviations of the associated angular distributions
267 $\sigma_0^{\text{CIP}} \approx 7^\circ$, $\sigma_0^{\text{SIP}} \approx 13^\circ$, and $\sigma_0^{\text{RIP}} \approx 21^\circ$. We note that these results are based on a simplified model that
268 does not consider possible steric interactions between the ligands at large angular displacements from the
269 octahedral configuration. However, knowing that the ligands in Fe^{RIP} can undergo large conformational
270 changes upon its enantiomerization, we believe these contributions to be negligible over the obtained
271 angular distributions. We further note that the experimentally obtained initial TAA values may be distorted
272 by the TAA band divergences near 305 nm and 325 nm and by minor contributions from the TAA of the
273 overlapping GSB band (for a spectral decomposition of the TA see fig. S.18). However, the broad width of
274 the HS TAA band minimizes the impact of the divergences (see fig. S.10a,c,e) and the TAA values in the
275 GSB band >290 nm closely match those in the HS state absorption region, such that their overlap becomes
276 negligible.

277 To assess the time dependent evolution of the TAA we note that it must eventually converge to zero due
278 to rotational diffusion of the photoselected molecular ensemble. The slowest time constant ρ_2 thus denotes
279 the rotational diffusion time of each sample. As expected, Fe^{RIP} displays the fastest rotational diffusion due
280 to the smaller volume of the PF_6 counterions and the lower viscosity of CH_2Cl_2 ($\eta = 0.41$ cP) compared
281 to CHCl_3 ($\eta = 0.54$ cP). However, the difference in solvent viscosity is too small to explain the difference
282 between ρ_2^{CIP} and ρ_2^{SIP} . As the global TAA decay to zero is well described by a single exponential in both
283 cases, we apply the Stokes-Einstein-Debye diffusion equation for spherical particles in solution, such that
284 $\rho_2 \propto \eta V$, where V is the rotational volume of the particle. We thus obtain $V^{\text{CIP}} \approx 1.5V^{\text{SIP}}$, which suggests
285 that the contact ion-pair has a larger rotational volume than the separated ion-pair. We thus speculate

286 that the larger interionic distance results in an increased global flexibility of the supramolecular complex,
287 which may thus accelerate its diffusion in solution.

288 The second time constant ρ_1 is too fast to be associated with a rotational diffusion process. In
289 the HS state absorption region it describes a minor, yet notable decrease in the measured TAA, which
290 is most strongly pronounced in Fe^{CIP} . In view of the preceding discussion and the sub-10 ps time
291 scale, we assign this process to a narrowing of the ligand system's conformational ensemble, due to the
292 intramolecular vibrational energy redistribution in the HS state. In this respect, the value obtained for
293 Fe^{RIP} , $\rho_1^{\text{RIP}} = 1.6 \pm 0.2$ ps, agrees reasonably well with recent results from ultrafast electron diffraction
294 experiments on $\text{Fe}^{\text{II}}(\text{bpy})_3(\text{PF}_6)_2$ single crystals, which determined a structural relaxation time of 2.4 ± 0.4
295 ps for the photoexcited HS state⁴². Surprisingly, ρ_1 describes an increase of the TAA in the GSB region
296 with a much larger contribution to the dynamics compared to the HS state absorption region. We thus
297 propose that the vibronic progression in the ground state absorption renders the GSB region more sensitive
298 to the IVR process, albeit with a complex contribution to the obtained TAA value, as indicated by its
299 variation across the GSB band.

300 We now turn to the TRCD experiments to determine the structural evolution of the HS state. For
301 $\Lambda\text{-Fe}^{\text{CIP}}$, the sign inversion and equal band amplitudes of the HS CD at early pump-probe delays are
302 consistent with an excitonic CD originating from the coupled long-axis LC transitions of the HS state,
303 arranged in a near-rigid octahedral configuration. This assignment may seem at odds with the asymmetry
304 of the corresponding steady-state CD bands, which are also known to be dominated by excitonically
305 coupled LC transitions. In this case, however, the asymmetry is commonly assigned to overlapping
306 electronic ground state transitions^{43,44}, whereas for the HS state we found its absorption to be well
307 described by a single absorption band (see fig. S.18a). Furthermore, its spectral position agrees very well
308 with the zero-crossing of the bisignate HS CD, as expected from an excitonic coupling case.

309 In this view, the observed asymmetric decay of the HS CD is particularly striking, as it indicates a
310 structural change that breaks the octahedral symmetry of the complex. Quite remarkably, this excludes the
311 symmetric stretching mode of the metal-ligand bonds, which has commonly been assumed to be the single
312 active reaction coordinate in the HS state decay of $[\text{Fe}^{\text{II}}(\text{bpy})_3]^{2+4}$. This is supported by excitonic coupling
313 and TDDFT calculations by Rudolph and co-workers⁴⁴, which suggest that the steady-state LC CD band

314 ratio is preserved for structural changes that maintain the three-fold rotation axis of the complex. These
315 include equal changes in the three metal-ligand bond lengths, and equal out-of-plane ligand rotations
316 around the bonds (θ in the preceding discussion). We therefore propose that the asymmetric band
317 decay requires a reaction coordinate that breaks the C_3 axis. In fact, it has previously been suggested
318 that the resulting Jahn-Teller (JT) and pseudo Jahn-Teller (PJT) interactions may lead to a significant
319 re-distribution of CD band intensities⁴⁵. In the trigonal structure of $[\text{Fe}^{\text{II}}(\text{dm-bpy})_3]^{2+}$, the high-energy
320 CD band is of non-degenerate A_2 symmetry and the low-energy band of doubly degenerate E symmetry.
321 Zgierski and Pawlikowski then calculated the impact of a vibronically coupled JT- and PJT-active mode of
322 doubly degenerate e -symmetry on the steady-state CD⁴⁶. The results show that the PJT interaction has
323 a particularly strong impact on the CD band shapes with a pronounced suppression of the high-energy
324 band compared to the low-energy band. On this basis, the asymmetric HS CD decay unambiguously
325 identifies the racemizing Ray-Dutt twist with its e -symmetry⁴⁷ as a reaction coordinate in the HS state
326 decay of $[\text{Fe}^{\text{II}}(\text{dm-bpy})_3]^{2+}$. This assignment thus leads to a consistent mechanistic picture, where the
327 diastereomeric ion-pairing controls the configurational equilibrium and lengthens the lifetime of the HS
328 state of $[\text{Fe}^{\text{II}}(\text{dm-bpy})_3]^{2+}$ by counteracting the rotational lability of the metal-ligand bonds.

329 In this respect, the comparison with the HS CD evolution in Λ - Fe^{SIP} offers further insights into the
330 proposed reaction mechanism. At the earliest pump-probe delay, its HS CD is already asymmetric. This
331 can now be explained by its broader angular conformational ensemble containing a larger fraction of
332 distorted octahedral structures. We note that this is consistent with the spectral changes observed in the
333 steady-state CD, where a similar suppression of the high-energy band was found for the solvent change
334 from Fe^{CIP} to Fe^{SIP} (see fig. S.3 in the SI). From the time evolution of the HS CD band amplitudes we then
335 extracted approximately the same time constant of 70 ps for both Fe^{CIP} and Fe^{SIP} , however with a larger
336 relative pre-exponential factor for Fe^{SIP} . Surprisingly, this suggests that the associated structural dynamics
337 are largely equivalent for Fe^{CIP} and Fe^{SIP} , whereas a stronger diastereomeric interaction mainly decreases
338 the frequency of their occurrence.

339 In light of the obtained results, we now propose a refined reaction scheme for the back-SCO of tris-
340 chelate Fe^{II} complexes, illustrated in fig. 5. Upon photoexcitation of the LS ground state, a vibrationally
341 excited HS state with elongated Fe-N bonds (HS*) is formed via an ultrafast forward-SCO. The HS*

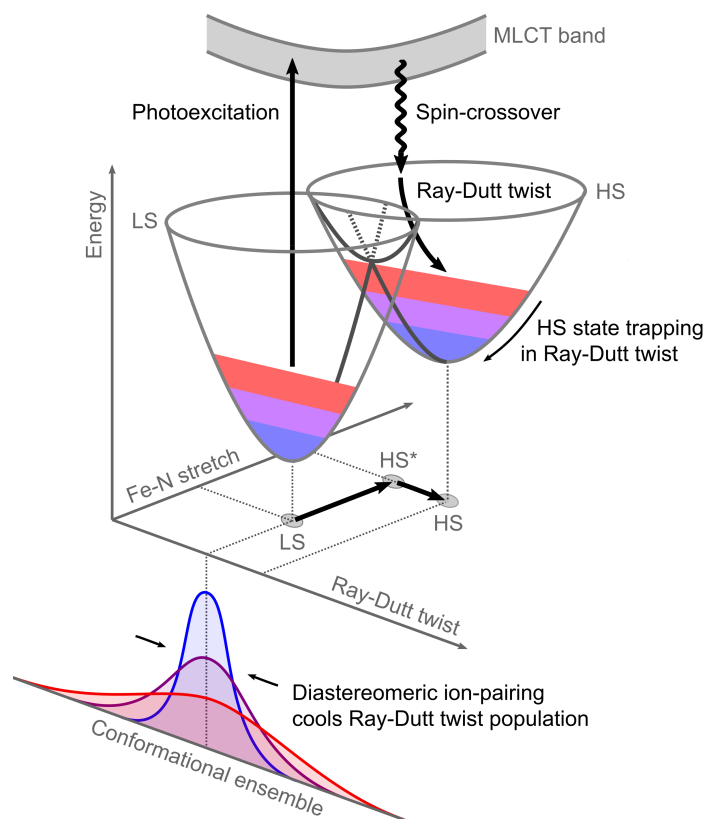


Figure 5. As the spin-relaxation of $\text{Fe}^{\text{II}}(\text{dm-bpy})_3$ is driven by the Ray-Dutt twist, the diastereomeric ion-pairing traps the HS state in its vibrational potential. The TRCD experiments show that $\text{Fe}^{\text{II}}(\text{dm-bpy})_3$ is a two-mode system: photoexcitation of its ground state (LS) creates a vibrationally excited HS state with expanded Fe-N bonds (HS^*), which then evolves along the Ray-Dutt twisting coordinate to a distorted coordination configuration (HS), where an increased spin-orbit coupling facilitates the conversion back to the ground state. The diastereomeric ion-pairing narrows the conformational distribution of the ligands along the twisting coordinate, thus effectively cooling its vibrational population below the LS-HS barrier and extending the lifetime of the HS state.

342 state then evolves along the Ray-Dutt twisting coordinate towards its minimum energy configuration (HS)
 343 in an entropy driven process with a 70 ps time constant. The resulting distortion of the Fe^{II} -centered
 344 coordination sphere enhances the spin-orbit coupling with the ground state and thus facilitates the decay
 345 of the HS state. Without any diastereomeric interaction, the lability of the Fe-N bonds implies a broad
 346 vibrational population of the Ray-Dutt twist in the LS ground state, as suggested by the broad angular
 347 conformational ensemble of the ligands. As illustrated in fig. 5, the forward-SCO transfers the broad
 348 vibrational population to the HS state. In the non-adiabatic multiphonon spin-relaxation mechanism
 349 developed by Buhks *et al.*¹⁴, this facilitates an efficient non-radiative coupling of the HS with the ground
 350 state. In this picture, the diastereomeric ion-pairing effectively cools the population of the Ray-Dutt twist,

351 thus narrowing the angular conformational ensemble of the ligands. In direct analogy to the cryogenic
352 cooling of vibrational modes in LIESST, the photoexcited HS state population then remains trapped in the
353 potential of the Ray-Dutt twist. In this picture, the reduced diastereomeric interactions in CH₂Cl₂ increase
354 the population of higher-order vibrational states without affecting the vibrational potential, thus increasing
355 the rate of spin-relaxation, without any observable change in the time scale of the associated structural
356 dynamics.

357 Along with the symmetric stretch mode of the Fe-N bonds, this establishes the symmetry-breaking
358 Ray-Dutt twist as a key vibrational mode in the non-radiative coupling of the HS ⁵T₂ and the LS ¹A₁
359 state in octahedral Fe^{II} SCO complexes. [Fe^{II}(bpy)₃]²⁺ thus becomes a two-mode system, much like the
360 constrained [Fe^{II}(terpy)₂]²⁺, where anisotropic bond expansions also drive a Jahn-Teller active distortion
361 of the coordination sphere in the HS state¹⁹. In this view, it may seem somewhat surprising that this
362 mechanism has previously escaped direct detection in unconstrained tris-chelate Fe^{II} complexes. However,
363 already Purcell suggested that only a minor displacement along a torsional twisting coordinate would be
364 required to induce a SCO²⁴.

365 Almost 20 years after Hauser established [Fe^{II}(bpy)₃]²⁺ as the archetypal SCO system following a
366 single active reaction coordinate model⁴, we can now conclude that this complex has become an exception
367 to its own rule. However, the additional torsional twisting coordinate opens novel avenues for efficient
368 spin-state trapping at RT of Fe^{II}-based SCO complexes by tuning the mechanical properties of their
369 ligand system. Through the diastereomeric ion-pairing introduced in this study, we demonstrated that
370 this can even be achieved without any chemical engineering of ligands. This novel diastereoselective
371 supramolecular approach thus promises to become a particularly attractive strategy for trapping spin-states
372 of chiral SCO complexes in both the liquid and the solid state, where it may directly complement existing
373 ligand-field engineering approaches. Moreover, a similar strategy was recently pursued by Paulus *et*
374 *al.*, who reduced the intersystem crossing rate from the MLCT manifold by suppressing the vibrational
375 modes coupled to the HS state formation in a bridge-stabilized Fe^{II} polypyridine complex⁴⁸. Our results
376 may thus also inform new strategies for kinetically stabilizing the photo-redox active MLCT and LMCT
377 states of Fe^{II} and Fe^{III} complexes, respectively^{49,50}. In a broader context, the presented results refine
378 our understanding of SCO-induced structural dynamics at Fe sites, which play a fundamental role in the

379 oxygen binding mechanism of heme-proteins and their function in the mammalian respiratory system, for
380 example^{51,52}.

381 Finally, this work enhances the scope of TRCD for resolving ultrafast structural dynamics of molecular
382 systems in solution and demonstrates the unique advantages of this approach: due to the broad conforma-
383 tional ensemble determined for Fe^{RIP}, we speculate that the ensemble-averaged ligand twisting motions
384 may currently be difficult to capture with established ultrafast X-Ray solution scattering techniques⁵³.
385 TRCD on the other hand is highly sensitive to the chiral properties of the excited state, such that even
386 minor symmetry-breaking structural distortions can have a detectable impact on the excited state CD.

387 **Methods**

388 **Sample preparation**

389 Following literature procedures^{54,55}, (NH₄)₂Fe(SO₄)₂·6 H₂O (78 mg, 0.2 mmol) and 4,4'-dimethyl-2,2'-
390 dipyridyl (111 mg, 0.6 mmol) were dissolved in 10 mL of an EtOH/water mixture (2/1) and refluxed for
391 30 minutes. The solution was cooled down and then added to a saturated solution of KPF₆ in water. The
392 precipitate was collected by filtration, washed with water and dried under reduced pressure. 145 mg (yield
393 81%) of Fe^{II}(dm-bpy)₃(PF₆)₂ were recovered. For the preparation of Fe^{II}(dm-bpy)₃(Λ,Δ-TT)₂, 2 equiv. of
394 P(V) TRISPHAT anions (Λ,Δ-TT)^{56,57} were added to Fe^{II}(dm-bpy)₃(PF₆)₂ in a CH₂Cl₂/acetone mixture
395 (2:1) and the resulting complex was purified by column chromatography over silica gel (CH₂Cl₂ as eluent).
396 The observed diastereomeric ratio in CDCl₃ was determined by ¹H-NMR spectroscopy and it was in
397 agreement with literature data (diastereomeric ratio *dr*>50:1)²⁸. For the ultrafast optical measurements,
398 the sample was dissolved in spectroscopy grade CHCl₃ and CH₂Cl₂ with a total volume of approximately
399 8 mL per experiment. Since Fe^{II}(dm-bpy)₃(Λ-TT)₂ contained trace amounts of tributylamine (<1 mol%)
400 from the preparation of the Λ-TT salt, 0.3 mol% of tributylamine was added to the Fe^{II}(dm-bpy)₃(Δ-TT)₂
401 solutions, increasing the solubility of the compound. The sample concentration was adapted to achieve a
402 maximum sample absorbance of approximately 0.7 OD near 300 nm for each measurement. For transient
403 absorption (TA) and anisotropy (TAA) measurements, a 0.2 mm pathlength flow cell with ultrathin drilled
404 windows (Starna) was used whereas for the time-resolved circular dichroism (TRCD) measurements, an
405 equivalent 0.5 mm pathlength flow cell from low-strain quartz was employed. For all experiments, the

406 sample was continuously circulated in a closed loop via a micro annular gear pump (HNP Mikrosysteme).

407 **Transient absorption and anisotropy in the deep-UV**

408 The laser setup for the ultrafast optical measurements has been described in detail elsewhere^{58,59}. Briefly, a
409 customized cryogenic Ti:Sapphire amplifier (KM Lasers) with an exceptional shot-to-shot stability of 0.1%
410 root-mean-square, pumps a commercial non-collinear optical parametric amplifier (Light Conversion) at 20
411 kHz. The broadband visible femtosecond pulses (520-720 nm) are split into a pump and probe arm via an
412 ultrafast thin-film beamsplitter. The probe pulses are achromatically doubled in a thin BBO crystal⁶⁰ and
413 cover 260–360 nm. The pump pulses are spectrally filtered via several reflections off ultrafast multilayer
414 mirrors, which limit the reflected bandwidth to approximately 520-575 nm at full-width-half-maximum
415 (FWHM) (the spectrum is displayed in fig. S.1). The pump pulses are compressed via several reflections
416 on a chirped mirror pair to compensate for any transmissive optics prior to the sample. The resulting pulse
417 duration was determined with a commercial FROG system (Swamp Optics) to be approximately 15 fs.

418 For the transient absorption (TA) and anisotropy (TAA) experiments, the probe pulse was set to
419 S-polarization with an achromatic half-wave plate before splitting the beam into a probe and a reference
420 arm with a 1 mm thick reflective neutral density filter (0.3 OD). The probe was focussed into the sample
421 with a 10 cm focal-length off-axis parabolic mirror, resulting in a focal spot diameter of approximately 70
422 μm ($1/e^2$). The probe polarization was cleaned with a high-quality Glan-Laser polarizer prior to detection
423 with a fiber-coupled imaging spectrograph, equipped with two CMOS chips for recording the probe and
424 reference simultaneously shot-to-shot. The pump polarization was cleaned via a Glan-Laser polarizer
425 and switched between S- and P-polarization via a motorized achromatic half-wave plate. The pump was
426 focussed via a 75 cm focal-length concave mirror to a spot diameter of approximately 270 μm ($1/e^2$),
427 where an energy of 0.8 μJ per pulse was used to photoexcite the sample. The resulting peak fluence
428 of approximately 2.8 $\text{mJ } \mu\text{m}^{-2}$ was confirmed to be in the linear excitation regime of the sample (see
429 section S.2). At a given pump-probe delay t , 30,000 consecutive probe shots were acquired for each
430 pump-polarization state, resulting in a TA spectrum for parallel pump and probe polarizations (TA^{\parallel}) and a
431 second for perpendicular polarizations (TA^{\perp}). The isotropic magic-angle TA and the TAA spectrum were
432 then calculated as:

$$\text{TA}(\lambda, t) = \frac{1}{3} \left(\text{TA}^{\parallel}(\lambda, t) + 2\text{TA}^{\perp}(\lambda, t) \right), \quad \text{TAA}(\lambda, t) = \frac{1}{3} \left(\text{TA}^{\parallel}(\lambda, t) - \text{TA}^{\perp}(\lambda, t) \right) \times \left(\text{TA}(\lambda, t) \right)^{-1}$$

433 For the reported experiments, each pump-probe scan consisted of 104 pump-probe delays and was repeated
434 17 times for averaging. The instrument response function (IRF) of the measurements was determined in
435 neat CHCl_3 to be approximately 0.3 ps on average over the probed spectral region, with the data provided
436 in the SI. To quantify the TA and TAA kinetics, we performed a global analysis for each data set with the
437 OPTIMUS software package⁶¹, simultaneously fitting multi-exponential functions convoluted with the
438 Gaussian IRF over the probed spectral window.

439 **Time-resolved circular dichroism in the deep-UV**

440 Circular dichroism (CD) denotes the differential absorption of left- and right-handed circularly polarized
441 light and is sensitive to the spatial arrangement of excitonically coupled transition dipoles within a chiral
442 molecular system⁶². However, its translation to the time domain for tracking the ultrafast structural
443 dynamics of photochemical systems has remained a formidable challenge⁶³, due to characteristically low
444 signal levels in solution phase: the CD of common chiral molecules is 10^{-3} of their absorbance, such that
445 time-resolved CD (TRCD) requires a sensitivity on the order of 10^{-5} to record photoinduced changes.
446 On this level, polarization-sensitive optics easily distort broadband TRCD spectra, thus preventing their
447 spectro-kinetic analysis and obscuring the relevant chiral dynamics. Our TRCD setup is described in
448 detail in ref.³¹ and overcomes these issues through a broadband, artifact-free detection scheme with an
449 unprecedented absolute sensitivity of $\pm 1 \cdot 10^{-5}$ OD. Briefly, the setup employs the same pump and probe
450 pulses and detection system as the TA and TAA experiments. In addition, a photoelastic modulator is used
451 to switch the probe pulse polarization shot-to-shot from left- to right-circularly polarized. Transmitted
452 through a chiral sample, the intensity difference of consecutive probe pulses thus denotes the CD spectrum,
453 which can be recorded for ground and excited state species in a pump-probe scheme analogous to TA
454 spectroscopy. A TRCD spectrum is calculated by subtracting the ground state CD from the CD spectrum
455 of the photoexcited sample. To acquire clean TRCD spectra, the suppression of polarization artifacts
456 caused by static and pump-induced birefringence in the probe beam path is critical. Through the use of low-

457 birefringence optics, probe-polarization scrambling prior to dispersive detection and careful calibration of
458 the linear pump-polarization orientation, we measure an absolute sensitivity of $\pm 1 \cdot 10^{-5}$ OD and verified
459 the absence of any artifact before each TRCD measurement through a baseline measurement with racemic
460 $[\text{Fe}^{\text{II}}(\text{bpy})_3]^{2+}$ (for the procedure and results see S.4). Due to the large amount of glass from the employed
461 photoelastic modulator, lenses and polarizers, the probe pulses are stretched to approximately 500 fs. The
462 IRF of the TRCD measurements was determined in neat CHCl_3 to be approximately 0.5 ps on average
463 over the probed spectral region, with the data provided in the SI. The focal spot diameters of the probe and
464 pump pulses were $70 \mu\text{m}$ and $270 \mu\text{m}$ ($1/e^2$), respectively and an energy of $1.0 \mu\text{J}$ per pulse was used to
465 photoexcite the sample. The corresponding peak fluence of $3.5 \text{ mJ } \mu\text{m}^{-2}$ was determined to be within the
466 linear excitation regime (for details see section S.4). In order to reach the high signal-to-noise required
467 for the presented spectral analysis, the probe pulse referencing was performed via a recently developed
468 B-Matrix methodology^{64,65}, which results in superior noise suppression compared to common ratiometric
469 pixel-by-pixel referencing schemes. For the reported experiments, 30,000 probe shots were acquired per
470 pump-probe delay to calculate a TRCD spectrum, with 30 delay points forming a full pump-probe scan.
471 For the the Λ -diastereoisomers, 800 scans were performed for averaging, taking about 18 hours in total.
472 Due to the long data acquisition time, cross-checks with the Δ -diastereoisomers were restricted to 10 time
473 points and 600 scans. In order to extract the temporal evolution of the excited state CD, we developed a
474 global fitting procedure constrained by the expected GSB dynamics and a minimum number of excited
475 state CD bands. A detailed discussion of this procedure is presented in section S.4 in the SI.

476 **Acknowledgements**

477 We thank J. Spekowius and J. Helbing (Zürich University) for adapting and sharing the B-Matrix refer-
478 encing methodology and S. Grass (Geneva University) for the preparation of the enantiopure ammonium
479 TRISPHAT salts. We also thank L. Müller and B. Bauer (EPFL) for assistance in the laboratory and X.
480 Kong and C. Heinis (EPFL) for providing access to a steady-state CD spectrometer. Finally, we thank L. M.
481 Lawson Daku (Geneva University), G. Pescitelli and F. Santoro (Pisa University) for helpful discussions.
482 This work was supported by the Swiss NSF through the NCCR-MUST and by a fellowship within the
483 Postdoc-Program of the German Academic Exchange Service (DAAD).

484 Author contributions statement

485 JL and MO conceived the original idea. MO coordinated and carried out all aspects of the research
486 (experiments, data analysis and interpretation), discussing them regularly with MC. FZ and JL contributed
487 to sample preparation and manipulation. MO wrote the manuscript with contributions from all authors.

488 Data availability statement

489 The data that support the findings of this study are available from the corresponding author upon reasonable
490 request.

491 References

- 492 **1.** Molnár, G., Rat, S., Salmon, L., Nicolazzi, W. & Bousseksou, A. Spin Crossover Nanomaterials:
493 From Fundamental Concepts to Devices. *Adv. Mater.* **30**, 1703862, DOI: [https://doi.org/10.1002/adma.](https://doi.org/10.1002/adma.201703862)
494 [201703862](https://doi.org/10.1002/adma.201703862) (2018).
- 495 **2.** Halcrow, M. A. (ed.) *Spin-Crossover Materials: Properties and Applications* (Wiley, Chichester, West
496 Sussex, United Kingdom, 2013), 1st edition edn.
- 497 **3.** Hauser, A. Light-Induced Spin Crossover and the High-Spin→Low-Spin Relaxation. In *Spin Crossover*
498 *in Transition Metal Compounds II*, vol. 234, 155–198, DOI: [10.1007/b95416](https://doi.org/10.1007/b95416) (Springer Berlin Heidel-
499 berg, Berlin, Heidelberg, 2004). Series Title: Topics in Current Chemistry.
- 500 **4.** Hauser, A., Enachescu, C., Daku, M. L., Vargas, A. & Amstutz, N. Low-temperature lifetimes
501 of metastable high-spin states in spin-crossover and in low-spin iron(II) compounds: The rule and
502 exceptions to the rule. *Coord. Chem. Rev.* **250**, 1642–1652, DOI: [10.1016/j.ccr.2005.12.006](https://doi.org/10.1016/j.ccr.2005.12.006) (2006).
- 503 **5.** Gawelda, W. *et al.* Ultrafast Nonadiabatic Dynamics of [FeII(bpy)3]2+ in Solution. *J. Am. Chem. Soc.*
504 **129**, 8199–8206, DOI: [10.1021/ja070454x](https://doi.org/10.1021/ja070454x) (2007).
- 505 **6.** Smeigh, A. L., Creelman, M., Mathies, R. A. & McCusker, J. K. Femtosecond Time-Resolved Optical
506 and Raman Spectroscopy of Photoinduced Spin Crossover: Temporal Resolution of Low-to-High Spin
507 Optical Switching. *J. Am. Chem. Soc.* **130**, 14105–14107, DOI: [10.1021/ja805949s](https://doi.org/10.1021/ja805949s) (2008). Publisher:
508 American Chemical Society.
- 509 **7.** Consani, C. *et al.* Vibrational Coherences and Relaxation in the High-Spin State of Aqueous
510 [FeII(bpy)3]2+. *Angewandte Chemie Int. Ed.* **48**, 7184–7187, DOI: [10.1002/anie.200902728](https://doi.org/10.1002/anie.200902728) (2009).
- 511 **8.** Auböck, G. & Chergui, M. Sub-50-fs photoinduced spin crossover in [Fe(bpy)3]2+. *Nat. Chem.* **7**,
512 629–633, DOI: [10.1038/nchem.2305](https://doi.org/10.1038/nchem.2305) (2015).
- 513 **9.** Gawelda, W. *et al.* Structural Determination of a Short-Lived Excited Iron(II) Complex by Picosecond
514 X-Ray Absorption Spectroscopy. *Phys. Rev. Lett.* **98**, 057401, DOI: [10.1103/PhysRevLett.98.057401](https://doi.org/10.1103/PhysRevLett.98.057401)
515 (2007). Publisher: American Physical Society.

- 516 **10.** Bressler, C. *et al.* Femtosecond XANES Study of the Light-Induced Spin Crossover Dynamics in an
517 Iron(II) Complex. *Science* **323**, 489–492, DOI: [10.1126/science.1165733](https://doi.org/10.1126/science.1165733) (2009).
- 518 **11.** Huse, N. *et al.* Femtosecond Soft X-ray Spectroscopy of Solvated Transition-Metal Complexes:
519 Deciphering the Interplay of Electronic and Structural Dynamics. *The J. Phys. Chem. Lett.* **2**, 880–884,
520 DOI: [10.1021/jz200168m](https://doi.org/10.1021/jz200168m) (2011). Publisher: American Chemical Society.
- 521 **12.** Zhang, W. *et al.* Tracking excited-state charge and spin dynamics in iron coordination complexes.
522 *Nature* **509**, 345–348, DOI: [10.1038/nature13252](https://doi.org/10.1038/nature13252) (2014). Number: 7500 Publisher: Nature Publishing
523 Group.
- 524 **13.** Lemke, H. T. *et al.* Coherent structural trapping through wave packet dispersion during photoinduced
525 spin state switching. *Nat. Commun.* **8**, 15342, DOI: [10.1038/ncomms15342](https://doi.org/10.1038/ncomms15342) (2017).
- 526 **14.** Buhks, E., Navon, G., Bixon, M. & Jortner, J. Spin conversion processes in solutions. *J. Am. Chem.*
527 *Soc.* **102**, 2918–2923, DOI: [10.1021/ja00529a009](https://doi.org/10.1021/ja00529a009) (1980).
- 528 **15.** Sutin, N. Nuclear, electronic, and frequency factors in electron transfer reactions. *Accounts Chem.*
529 *Res.* **15**, 275–282, DOI: [10.1021/ar00081a002](https://doi.org/10.1021/ar00081a002) (1982).
- 530 **16.** Decurtins, S., Gülich, P., Köhler, C. P., Spiering, H. & Hauser, A. Light-induced excited spin
531 state trapping in a transition-metal complex: The hexa-1-propyltetrazole-iron (II) tetrafluoroborate
532 spin-crossover system. *Chem. Phys. Lett.* **105**, 1–4, DOI: [10.1016/0009-2614\(84\)80403-0](https://doi.org/10.1016/0009-2614(84)80403-0) (1984).
- 533 **17.** Cammarata, M. *et al.* Sequential Activation of Molecular Breathing and Bending during Spin-
534 Crossover Photoswitching Revealed by Femtosecond Optical and X-Ray Absorption Spectroscopy.
535 *Phys. Rev. Lett.* **113**, 227402, DOI: [10.1103/PhysRevLett.113.227402](https://doi.org/10.1103/PhysRevLett.113.227402) (2014).
- 536 **18.** Nance, J., Bowman, D. N., Mukherjee, S., Kelley, C. T. & Jakubikova, E. Insights into the Spin-
537 State Transitions in [Fe(tpy)₂]²⁺: Importance of the Terpyridine Rocking Motion. *Inorg. Chem.* **54**,
538 11259–11268, DOI: [10.1021/acs.inorgchem.5b01747](https://doi.org/10.1021/acs.inorgchem.5b01747) (2015). Publisher: American Chemical Society.
- 539 **19.** Zhang, W. & Gaffney, K. J. Mechanistic Studies of Photoinduced Spin Crossover and Electron
540 Transfer in Inorganic Complexes. *Accounts Chem. Res.* **48**, 1140–1148, DOI: [10.1021/ar500407p](https://doi.org/10.1021/ar500407p)
541 (2015). Publisher: American Chemical Society.
- 542 **20.** Stock, P. *et al.* Molecular Spin Crossover in Slow Motion: Light-Induced Spin-State Transitions in
543 Trigonal Prismatic Iron(II) Complexes. *Inorg. Chem.* **55**, 5254–5265, DOI: [10.1021/acs.inorgchem.
544 6b00238](https://doi.org/10.1021/acs.inorgchem.6b00238) (2016). Publisher: American Chemical Society.
- 545 **21.** Marchivie, M., Guionneau, P., Létard, J.-F. & Chasseau, D. Photo-induced spin-transition: the
546 role of the iron(II) environment distortion. *Acta Crystallogr. Sect. B Struct. Sci.* **61**, 25–28, DOI:
547 [10.1107/S0108768104029751](https://doi.org/10.1107/S0108768104029751) (2005).
- 548 **22.** Halcrow, M. Structure: function relationships in molecular spin-crossover complexes. *Chem. Soc. Rev.*
549 **40**, 4119–4142, DOI: [10.1039/C1CS15046D](https://doi.org/10.1039/C1CS15046D) (2011). Publisher: Royal Society of Chemistry.
- 550 **23.** Purcell, K. F. & Zapata, J. P. Magnetic isomers. *cis-*
551 *Bis(cyanotriphenylborato)bisphenanthrolineiron(II)*. *J. Chem. Soc. Chem. Commun.* 497–499,
552 DOI: [10.1039/C39780000497](https://doi.org/10.1039/C39780000497) (1978). Publisher: The Royal Society of Chemistry.
- 553 **24.** Purcell, K. F. Pseudorotational intersystem crossing in d₆ complexes. *J. Am. Chem. Soc.* **101**,
554 5147–5152, DOI: [10.1021/ja00512a005](https://doi.org/10.1021/ja00512a005) (1979). Publisher: American Chemical Society.

- 555 **25.** Vanquickenborne, L. G. & Pierloot, K. Role of spin change in the stereomobile reactions of strong-
556 field d6 transition-metal complexes. *Inorg. Chem.* **20**, 3673–3677, DOI: [10.1021/ic50225a018](https://doi.org/10.1021/ic50225a018) (1981).
557 Publisher: American Chemical Society.
- 558 **26.** McCusker, J. K., Rheingold, A. L. & Hendrickson, D. N. Variable-Temperature Studies of Laser-
559 Initiated 5T2 → 1A1 Intersystem Crossing in Spin-Crossover Complexes: Empirical Correlations
560 between Activation Parameters and Ligand Structure in a Series of Polypyridyl Ferrous Complexes.
561 *Inorg. Chem.* **35**, 2100–2112, DOI: [10.1021/ic9507880](https://doi.org/10.1021/ic9507880) (1996). Publisher: American Chemical Society.
- 562 **27.** Ashley, D. C. & Jakubikova, E. Ray-Dutt and Bailar Twists in Fe(II)-Tris(2,2'-bipyridine): Spin States,
563 Sterics, and Fe–N Bond Strengths. *Inorg. Chem.* **57**, 5585–5596, DOI: [10.1021/acs.inorgchem.8b00560](https://doi.org/10.1021/acs.inorgchem.8b00560)
564 (2018). Publisher: American Chemical Society.
- 565 **28.** Lacour, J., Jodry, J. J., Ginglinger, C. & Torche-Haldimann, S. Diastereoselective Ion Pairing of
566 TRISPHAT Anions and Tris(4,4'-dimethyl-2,2'-bipyridine)iron(II). *Angewandte Chemie Int. Ed.* **37**,
567 2379–2380, DOI: [10.1002/\(SICI\)1521-3773\(19980918\)37:17<2379::AID-ANIE2379>3.0.CO;2-C](https://doi.org/10.1002/(SICI)1521-3773(19980918)37:17<2379::AID-ANIE2379>3.0.CO;2-C)
568 (1998).
- 569 **29.** Frantz, R., Pinto, A., Constant, S., Bernardinelli, G. & Lacour, J. Fluorinated TRISPHAT Anions:
570 Spectroscopic Probes for Detailed Asymmetric Ion Pairing Studies. *Angewandte Chemie Int. Ed.* **44**,
571 5060–5064, DOI: [10.1002/anie.200500862](https://doi.org/10.1002/anie.200500862) (2005).
- 572 **30.** Reddy, G. M., Ballesteros-Garrido, R., Lacour, J. & Caldarelli, S. Determination of Labile Chiral
573 Supramolecular Ion Pairs by Chromatographic NMR Spectroscopy. *Angewandte Chemie Int. Ed.* **52**,
574 3255–3258, DOI: [10.1002/anie.201209616](https://doi.org/10.1002/anie.201209616) (2013).
- 575 **31.** Oppermann, M. *et al.* Ultrafast broadband circular dichroism in the deep ultraviolet. *Optica* **6**, 56–60,
576 DOI: [10.1364/OPTICA.6.000056](https://doi.org/10.1364/OPTICA.6.000056) (2019).
- 577 **32.** Oppermann, M. *et al.* Broad-Band Ultraviolet CD Spectroscopy of Ultrafast Peptide Backbone
578 Conformational Dynamics. *The J. Phys. Chem. Lett.* **10**, 2700–2705, DOI: [10.1021/acs.jpcllett.9b01253](https://doi.org/10.1021/acs.jpcllett.9b01253)
579 (2019).
- 580 **33.** Mason, S. F., Peart, B. J. & Waddell, R. E. Optical rotatory power of co-ordination compounds. Part
581 XVI. Intermediate exciton coupling in the circular dichroism of trisbipyridyl complexes. *J. Chem. Soc.*
582 *Dalton Transactions* **0**, 944–949, DOI: [10.1039/DT9730000944](https://doi.org/10.1039/DT9730000944) (1973). Publisher: Royal Society of
583 Chemistry.
- 584 **34.** Castellucci, E., Salvi, P. R. & Foggi, P. Two-photon excitation spectra of the lowest electronic states
585 of 2,2'-bipyridine. *Chem. Phys.* **66**, 281–291, DOI: [10.1016/0301-0104\(82\)88027-0](https://doi.org/10.1016/0301-0104(82)88027-0) (1982).
- 586 **35.** Mason, S. F. The electronic spectra and optical activity of phenanthroline and dipyridyl metal
587 complexes. *Inorganica Chimica Acta Rev.* **2**, 89–109, DOI: [10.1016/0073-8085\(68\)80016-6](https://doi.org/10.1016/0073-8085(68)80016-6) (1968).
- 588 **36.** Bosnich, B. Application of exciton theory to the determination of the absolute configurations of
589 inorganic complexes. *Accounts Chem. Res.* **2**, 266–273, DOI: [10.1021/ar50021a002](https://doi.org/10.1021/ar50021a002) (1969).
- 590 **37.** Reist, M., Testa, B., Carrupt, P.-A., Jung, M. & Schurig, V. Racemization, enantiomerization,
591 diastereomerization, and epimerization: Their meaning and pharmacological significance. *Chirality* **7**,
592 396–400, DOI: [10.1002/chir.530070603](https://doi.org/10.1002/chir.530070603) (1995).
- 593 **38.** Jodry, J. J., Frantz, R. & Lacour, J. Supramolecular Stereocontrol of Octahedral Metal-Centered
594 Chirality. Ligand Modulation. *Inorg. Chem.* **43**, 3329–3331, DOI: [10.1021/ic049661d](https://doi.org/10.1021/ic049661d) (2004).

- 595 **39.** Miller, J. N. & McCusker, J. K. Outer-sphere effects on ligand-field excited-state dynamics: solvent
596 dependence of high-spin to low-spin conversion in [Fe(bpy)₃]²⁺. *Chem. Sci.* **11**, 5191–5204, DOI:
597 [10.1039/D0SC01506G](https://doi.org/10.1039/D0SC01506G) (2020). Publisher: Royal Society of Chemistry.
- 598 **40.** Bethardy, G., Wang, X. & Perry, D. S. The role of molecular flexibility in accelerating intramolecular
599 vibrational relaxation. *Can. J. Chem.* **72**, 652–659, DOI: [10.1139/v94-090](https://doi.org/10.1139/v94-090) (1994).
- 600 **41.** Wallin, S., Davidsson, J., Modin, J. & Hammarström, L. Femtosecond Transient Absorption
601 Anisotropy Study on [Ru(bpy)₃]²⁺ and [Ru(bpy)(py)₄]²⁺. Ultrafast Interligand Randomization of the
602 MLCT State. *The J. Phys. Chem. A* **109**, 4697–4704, DOI: [10.1021/jp0509212](https://doi.org/10.1021/jp0509212) (2005).
- 603 **42.** Jiang, Y. *et al.* Direct observation of nuclear reorganization driven by ultrafast spin transitions.
604 *Nat. Commun.* **11**, 1–8, DOI: [10.1038/s41467-020-15187-y](https://doi.org/10.1038/s41467-020-15187-y) (2020). Number: 1 Publisher: Nature
605 Publishing Group.
- 606 **43.** Fan, J., Autschbach, J. & Ziegler, T. Electronic Structure and Circular Dichroism of Tris(bipyridyl)
607 Metal Complexes within Density Functional Theory. *Inorg. Chem.* **49**, 1355–1362, DOI: [10.1021/
608 ic9011586](https://doi.org/10.1021/ic9011586) (2010). Publisher: American Chemical Society.
- 609 **44.** Rudolph, M. & Autschbach, J. Calculation of Optical Rotatory Dispersion and Electronic Circular
610 Dichroism for Tris-bidentate Groups 8 and 9 Metal Complexes, With Emphasis on Exciton Coupling.
611 *The J. Phys. Chem. A* **115**, 2635–2649, DOI: [10.1021/jp111484z](https://doi.org/10.1021/jp111484z) (2011). Publisher: American Chemical
612 Society.
- 613 **45.** Richardson, F., Caliga, D., Hilmes, G. & Jenkins, J. Vibronic effects in the chiroptical spectra of
614 dissymmetric trigonal systems. *Mol. Phys.* **30**, 257–280, DOI: [10.1080/00268977500101931](https://doi.org/10.1080/00268977500101931) (1975).
- 615 **46.** Zgierski, M. Z. & Pawlikowski, M. Jahn–Teller, pseudo Jahn–Teller coupling, and circular dichroism
616 spectra of (E+A) e systems. *The J. Chem. Phys.* **70**, 3444–3452, DOI: [10.1063/1.437879](https://doi.org/10.1063/1.437879) (1979).
617 Publisher: American Institute of Physics.
- 618 **47.** Rodger, A. Template symmetry restrictions on reaction mechanisms. *Inorganica Chimica Acta* **185**,
619 193–200, DOI: [10.1016/S0020-1693\(00\)85444-4](https://doi.org/10.1016/S0020-1693(00)85444-4) (1991).
- 620 **48.** Paulus, B. C., Adelman, S. L., Jamula, L. L. & McCusker, J. K. Leveraging excited-state coherence
621 for synthetic control of ultrafast dynamics. *Nature* **582**, 214–218, DOI: [10.1038/s41586-020-2353-2](https://doi.org/10.1038/s41586-020-2353-2)
622 (2020). Number: 7811 Publisher: Nature Publishing Group.
- 623 **49.** McCusker, J. K. Electronic structure in the transition metal block and its implications for light
624 harvesting. *Science* **363**, 484–488, DOI: [10.1126/science.aav9104](https://doi.org/10.1126/science.aav9104) (2019). Publisher: American
625 Association for the Advancement of Science Section: Review.
- 626 **50.** Wenger, O. S. Is Iron the New Ruthenium? *Chem. - A Eur. J.* **25**, 6043–6052, DOI: [https://doi.org/10.
627 1002/chem.201806148](https://doi.org/10.1002/chem.201806148) (2019).
- 628 **51.** Kepp, K. P. Heme: From quantum spin crossover to oxygen manager of life. *Coord. Chem. Rev.* **344**,
629 363–374, DOI: [10.1016/j.ccr.2016.08.008](https://doi.org/10.1016/j.ccr.2016.08.008) (2017).
- 630 **52.** Kinschel, D. *et al.* Femtosecond X-ray emission study of the spin cross-over dynamics in haem
631 proteins. *Nat. Commun.* **11**, 4145, DOI: [10.1038/s41467-020-17923-w](https://doi.org/10.1038/s41467-020-17923-w) (2020).
- 632 **53.** Ki, H., Oang, K. Y., Kim, J. & Ihee, H. Ultrafast X-Ray Crystallography and Liquidography. *Annu.*
633 *Rev. Phys. Chem.* **68**, 473–497, DOI: [10.1146/annurev-physchem-052516-050851](https://doi.org/10.1146/annurev-physchem-052516-050851) (2017). Publisher:
634 Annual Reviews.

- 635 **54.** Pomeranc, D., Heitz, V., Chambron, J.-C. & Sauvage, J.-P. Octahedral Fe(II) and Ru(II) Complexes
636 Based on a New Bis 1,10-Phenanthroline Ligand That Imposes a Well Defined Axis. *J. Am. Chem. Soc.*
637 **123**, 12215–12221, DOI: [10.1021/ja011250y](https://doi.org/10.1021/ja011250y) (2001). Publisher: American Chemical Society.
- 638 **55.** Cazzanti, S., Caramori, S., Argazzi, R., Elliott, C. M. & Bignozzi, C. A. Efficient Non-corrosive
639 Electron-Transfer Mediator Mixtures for Dye-Sensitized Solar Cells. *J. Am. Chem. Soc.* **128**, 9996–
640 9997, DOI: [10.1021/ja062087f](https://doi.org/10.1021/ja062087f) (2006). Publisher: American Chemical Society.
- 641 **56.** Lacour, J., Ginglinger, C., Grivet, C. & Bernardinelli, G. Synthesis and Resolution of the Configura-
642 tionally Stable Tris(tetrachlorobenzenediolato)phosphate(V) Ion. *Angewandte Chemie Int. Ed. Engl.*
643 **36**, 608–610, DOI: <https://doi.org/10.1002/anie.199706081> (1997).
- 644 **57.** Favarger, F., Goujon-Ginglinger, C., Monchaud, D. & Lacour, J. Large-Scale Synthesis and Resolution
645 of TRISPHAT [Tris(tetrachlorobenzenediolato) Phosphate(V)] Anion. *The J. Org. Chem.* **69**, 8521–
646 8524, DOI: [10.1021/jo048641q](https://doi.org/10.1021/jo048641q) (2004). Publisher: American Chemical Society.
- 647 **58.** Auböck, G. *et al.* Femtosecond pump/supercontinuum-probe setup with 20 kHz repetition rate. *Rev.*
648 *Sci. Instruments* **83**, 093105, DOI: [10.1063/1.4750978](https://doi.org/10.1063/1.4750978) (2012).
- 649 **59.** Auböck, G., Consani, C., Mourik, F. v. & Chergui, M. Ultrabroadband femtosecond two-dimensional
650 ultraviolet transient absorption. *Opt. Lett.* **37**, 2337–2339, DOI: [10.1364/OL.37.002337](https://doi.org/10.1364/OL.37.002337) (2012).
- 651 **60.** Baum, P., Lochbrunner, S. & Riedle, E. Tunable sub-10-fs ultraviolet pulses generated by achromatic
652 frequency doubling. *Opt. Lett.* **29**, 1686–1688, DOI: [10.1364/OL.29.001686](https://doi.org/10.1364/OL.29.001686) (2004).
- 653 **61.** Slavov, C., Hartmann, H. & Wachtveitl, J. Implementation and Evaluation of Data Analysis Strategies
654 for Time-Resolved Optical Spectroscopy. *Anal. Chem.* **87**, 2328–2336, DOI: [10.1021/ac504348h](https://doi.org/10.1021/ac504348h)
655 (2015).
- 656 **62.** Berova, N., Polavarapu, P. L., Nakanishi, K. & Woody, R. W. *Comprehensive Chiroptical Spec-*
657 *troscopy: Instrumentation, Methodologies, and Theoretical Simulations* (Wiley, Hoboken, NJ, 2012),
658 volume 1 edition edn.
- 659 **63.** Meyer-Ilse, J., Akimov, D. & Dietzek, B. Recent advances in ultrafast time-resolved chirality
660 measurements: perspective and outlook: Ultrafast transient molecular chirality. *Laser & Photonics Rev.*
661 **7**, 495–505, DOI: [10.1002/lpor.201200065](https://doi.org/10.1002/lpor.201200065) (2013).
- 662 **64.** Feng, Y., Vinogradov, I. & Ge, N.-H. General noise suppression scheme with reference detection
663 in heterodyne nonlinear spectroscopy. *Opt. Express* **25**, 26262–26279, DOI: [10.1364/OE.25.026262](https://doi.org/10.1364/OE.25.026262)
664 (2017). Publisher: Optical Society of America.
- 665 **65.** Feng, Y., Vinogradov, I. & Ge, N.-H. Optimized noise reduction scheme for heterodyne spectroscopy
666 using array detectors. *Opt. Express* **27**, 20323–20346, DOI: [10.1364/OE.27.020323](https://doi.org/10.1364/OE.27.020323) (2019). Publisher:
667 Optical Society of America.

668 Supporting Information

669 Contents

670	S.1 Steady-state sample characterization	28
671	S.2 Transient absorption data and analysis	32
672	S.3 Transient anisotropy data and analysis	41
673	S.4 Time-resolved circular dichroism data and analysis	49
674	References Supporting Information	61

675 S.1 Steady-state sample characterization

676 Three samples were investigated: 1) $\text{Fe}^{\text{II}}(\text{dm-bpy})_3(\Lambda, \Delta\text{-TT})_2$ dissolved in CHCl_3 ($\Lambda, \Delta\text{-Fe}^{\text{CIP}}$), 2) $\text{Fe}^{\text{II}}(\text{dm-}$
677 $\text{bpy})_3(\Lambda, \Delta\text{-TT})_2$ dissolved in CH_2Cl_2 ($\Lambda, \Delta\text{-Fe}^{\text{SIP}}$), and 3) $\text{Fe}^{\text{II}}(\text{dm-bpy})_3(\text{PF}_6)_2$ dissolved in CH_2Cl_2
678 (Fe^{RIP}). Their steady-state absorption and CD spectra were obtained with a JASCO J-1100 CD spec-
679 trometer using a 1 mm pathlength cuvette. The maximum absorption of the samples in the ultraviolet
680 (UV) region was kept between 0.8 and 1.5 OD in order to achieve a good signal-to-noise whilst avoiding
681 saturation of the detector. All spectra were baseline-corrected via a solvent blank. Fig. S.1 displays the
682 absorption spectra of all three samples normalized to their respective absorption maxima in the plotted
683 spectral region. The left panel displays the absorption in the deep-UV region, which is dominated by
684 the ligand-centred (LC) $\pi\pi^*$ transitions of the complexes. Fe^{CIP} and Fe^{SIP} display nearly identical band
685 shapes with a maximum near 300 nm and a shoulder near 290 nm. Changing the solvent from CHCl_3
686 to CH_2Cl_2 results in a minor hypsochromic shift of about 1 nm. In direct comparison, Fe^{RIP} displays a
687 more pronounced hypsochromic shift, a reduced shoulder, a strongly enhanced absorption <270 nm, and
688 an additional broad shoulder at 320 nm. We attribute the latter to the absorption of the PF_6 counterions.
689 The right panel displays the absorption in the visible region and shows the metal-to-ligand charge-transfer
690 (MLCT) band. The amplitude of this band is about 10% of the LC band and shows a similar spectral shape.
691 It has been suggested that the double peak structure in the LC band stems from a vibrational progression
692 localized on the ligands^{si1, si2}. For the MLCT band, similar interpretations have been proposed, pointing to
693 a skeletal mode at 1607 cm^{-1} ^{si3}. However, Decurtins et al. have suggested that its double band structure

694 results from two partially overlapping electronic transitions^{si4}.

695 Fig. S.2 displays the steady-state CD spectra of Fe^{CIP} and Fe^{SIP}. Both display near identical spectral
696 shapes, dominated by two bands of opposite signs: 1) a high-energy band near 285 nm, and 2) a low-energy
697 band near 303 nm. This bisignate spectral structure is a typical signature of excitonically coupled electronic
698 transitions and for tris-bipyridyl complexes it has been established that the CD in this region is dominated
699 by the long-axis transitions of the bpy ligands^{si5,si6}. Due to the D₃ symmetry of the ligand system, the
700 high-energy band is of A₂ symmetry, whilst the low-energy band is degenerate with E-symmetry. In this
701 environment, the excitonic transitions from the coupled short-axis transitions are not optically active. The
702 observed absence of any vibronic structure in the CD spectra is a known effect in tris-bipyridyl complexes,
703 where the exciton splitting energy is typically much larger than the energy of the vibronically coupled
704 mode (see for example the discussion in ref.^{si1}).

705 In order to assess the impact of the solvent change on the diastereomeric ion pairs, we analyze their
706 CD spectra in more detail. The rotational strengths R_{A₂,E} of the two main bands are strongly reduced,
707 such that for the high-energy band R_{A₂}^{SIP}/R_{A₂}^{CIP} ≈ 0.52 and for the low-energy band R_E^{SIP}/R_E^{CIP} ≈ 0.64. In
708 both cases, the reduction in amplitude is larger than the reduction in the maximum absorption coefficient
709 ε (see fig. S.3a), which gives ε^{SIP}/ε^{CIP} ≈ 0.75. This is to be expected, since the diastereomeric ratio
710 decreases when the solvent polarity is increased. However, this does not rationalize the change in band
711 ratio, which is directly visible when the CD spectra are normalized to their maximum amplitude as shown
712 in fig. S.3b. For a quantitative comparison, we decomposed the normalized absorption and CD spectra
713 into a sum of Gaussian functions of the type G_n(λ) = A_nexp[−((λ − λ_n)/c_n)²]. The fits for Fe^{CIP} are
714 displayed in figure S.3c and S.3d, with near identical results obtained for Fe^{SIP}. Tables S.1 and S.2 display
715 the fit parameters corresponding to the Gaussian functions constituting the bands associated with the
716 LC transitions. For the absorption spectra, a hypsochromic shift of approximately 1 nm is apparent,
717 in addition to a minor increase of the amplitude of the higher Fe^{SIP} energy band. The hypsochromic shift is
718 similarly observed in the CD bands, yet it is striking that only the high-energy band significantly changes
719 in amplitude, displaying a pronounced reduction.

Sample	R^2	A_1	λ_1 (nm)	c_1 (nm)	A_2	λ_2 (nm)	c_2 (nm)
Fe ^{CIP}	0.9999	0.81	294.4	13.7	0.26	302.1	5.6
Fe ^{SIP}	0.9999	0.81	293.3	13.6	0.29	301.3	5.7

Table S.1. Fit parameters obtained from fitting a sum of four Gaussian functions to the normalized absorption spectra of Fe^{CIP} and Fe^{SIP}. Only the parameters associated with the LC absorption band are displayed with A_n referring to the amplitude, λ_n to the center wavelength and c_n to the width of the n^{th} Gaussian function, as defined in the text.

Sample	R^2	A_1	λ_1 (nm)	c_1 (nm)	A_2	λ_2 (nm)	c_2 (nm)	A_3	λ_3 (nm)	c_3 (nm)
Fe ^{CIP}	0.9997	-0.61	286.6	10.0	0.62	303.7	4.8	0.41	305.0	8.3
Fe ^{SIP}	0.9997	-0.49	285.7	9.2	0.62	302.6	4.8	0.40	303.8	8.6

Table S.2. Fit parameters obtained from fitting a sum of six Gaussian functions to the normalized CD spectra of Fe^{CIP} and Fe^{SIP}. Only the parameters associated with the LC absorption band are displayed with A_n referring to the amplitude, λ_n to the center wavelength and c_n to the width of the n^{th} Gaussian function, as defined in the text.

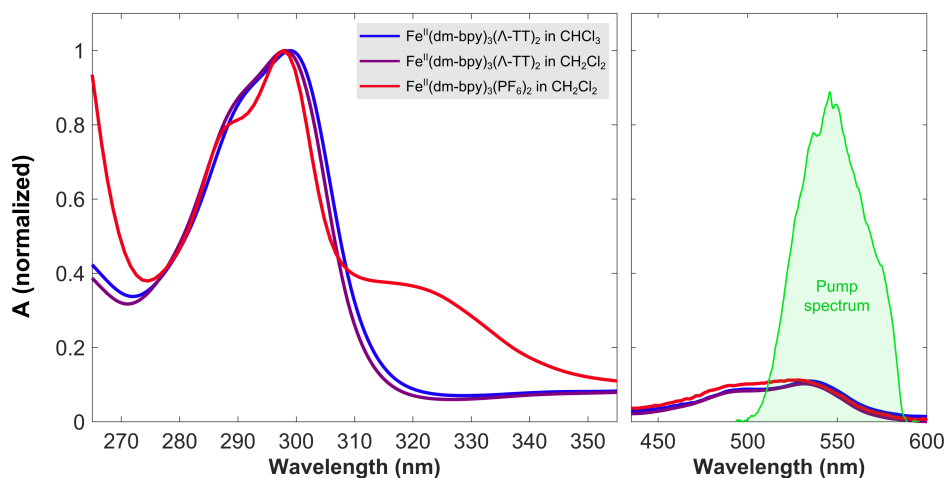


Figure S.1. Steady-state absorption spectra of the three samples investigated in this study. Each spectrum is normalized to its maximum amplitude within the displayed wavelength range. The right panel also includes the spectrum of the excitation pulse employed in the pump-probe experiments.

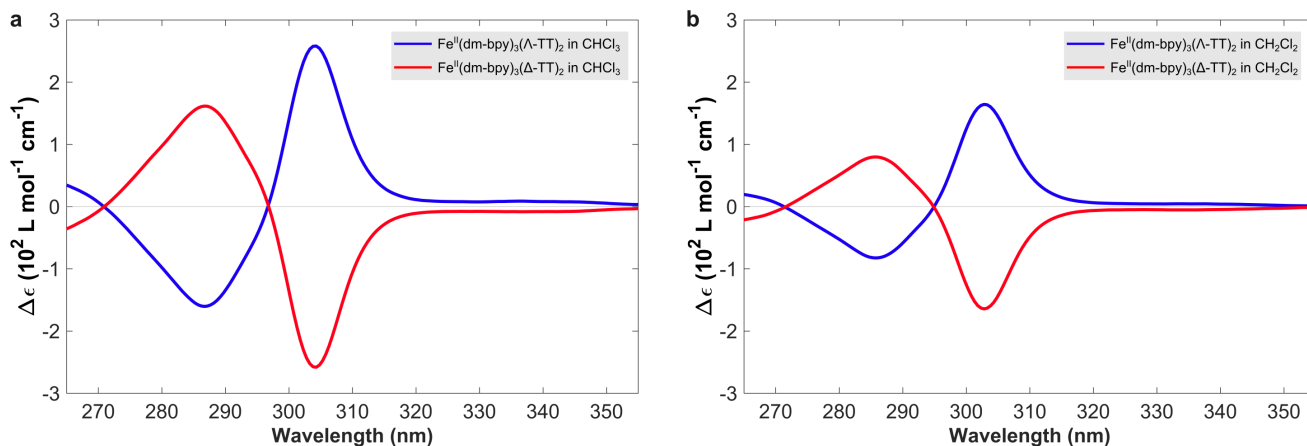


Figure S.2. Steady-state CD spectra of the Λ and Δ configurations of the diastereomeric ion pairs dissolved in CHCl_3 (a) and CH_2Cl_2 (b).

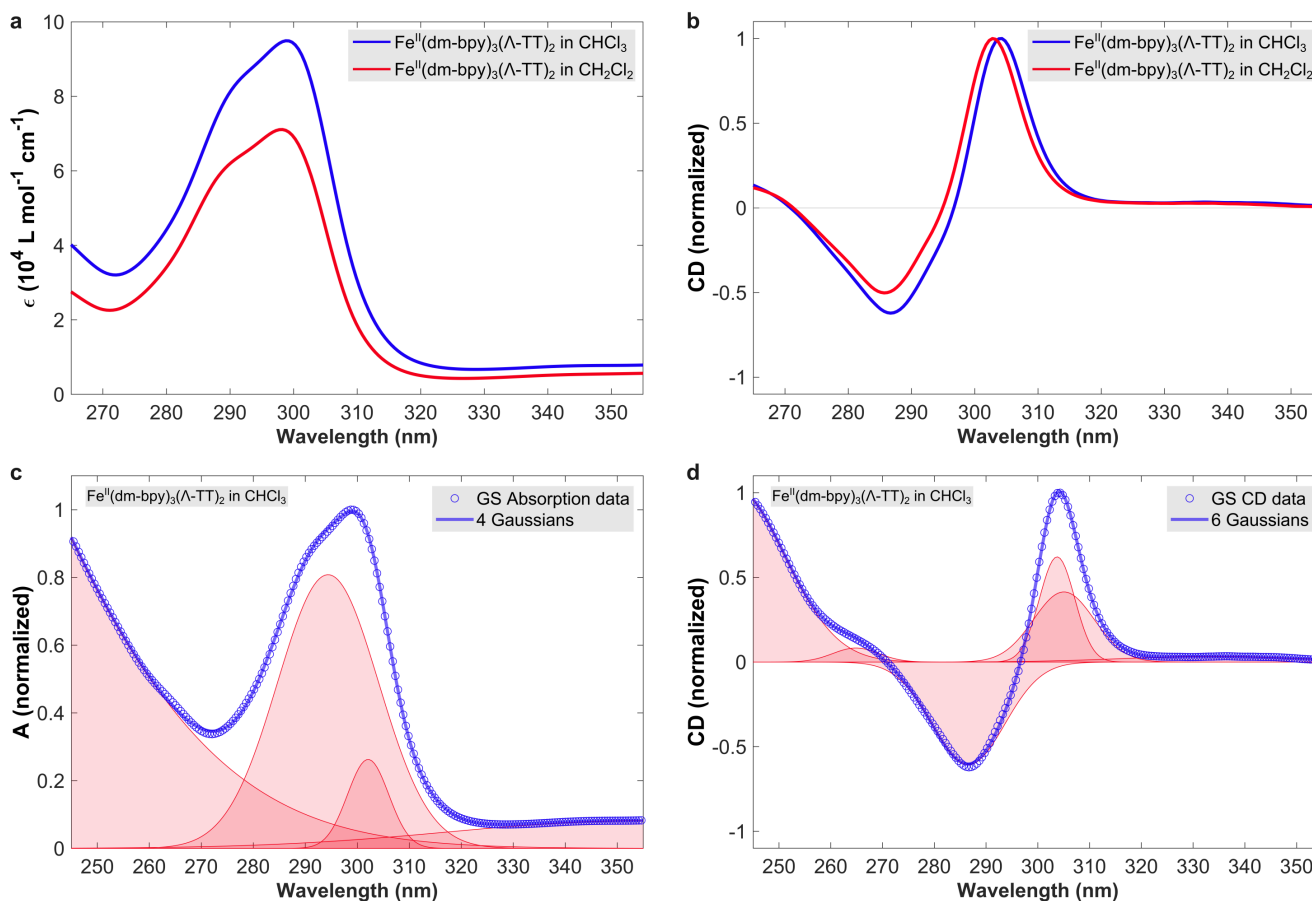


Figure S.3. Detailed comparison of the spectroscopic properties of the diastereomeric ion pair in its Λ configuration when dissolved in CHCl_3 and CH_2Cl_2 : Comparison of molar extinction as a function of wavelength (a), Comparison of CD spectra normalized to their maximum amplitude (b), spectral decomposition of the normalized absorption spectrum in CHCl_3 (c), and spectral decomposition of the normalized CD spectrum in CHCl_3 (d).

720 **S.2 Transient absorption data and analysis**

721 The experimental setup and measurement conditions for the transient absorption (TA) experiments are
722 reported in the Methods section. Here, technical details and further data sets are presented to support the
723 discussion in the main article.

724 **Instrument response function.** In order to characterize the instrument response function (IRF) of the
725 TA measurements, fig. S.4a displays the instantaneous response of pure CHCl_3 during the temporal overlap
726 of the pump and probe pulses. The onset of the response as a function of probe wavelength describes the
727 chirp of the probe pulse due to the group-velocity dispersion (GVD) from any transmissive optics in the
728 probe beam path and is routinely corrected in the post-processing of TA data^{si7}. At each probe wavelength,
729 the nonlinear solvent response is referred to as a coherent artifact (CA), which consists of the two-photon
730 absorption and cross-phase modulation caused by the temporal and spatial overlap of the pump and probe
731 pulses. Fig. S.4c,d displays the CA as a function of pump-probe delay at 290 nm and 335 nm. To quantify
732 the temporal width of the CA, the absolute value is taken of the TA signal and its local maxima are
733 determined. After cutting the data points between the two outermost maxima, the remaining data is fitted
734 with a Gaussian function. The data points prepared for the fit and the resulting fit functions are displayed
735 in fig. S.4c,d, whereas the associated full-width-half-maximum (FWHM) and fit quality (R^2) are plotted
736 as a function of probe wavelength in fig. S.4b. The figure displays an average FWHM of approximately
737 0.3 ps over the whole spectral range, starting at 0.5 ps near 270 nm and decreasing to 0.2 ps for probe
738 wavelengths >300 nm. We attribute the larger FWHM at shorter wavelengths to the higher dispersion of
739 transmissive optics in this spectral regime. Note that the fit quality around the chirp's inflection point near
740 310 nm is very poor due to additional oscillations and a phase flip in the CA, such that the estimate of the
741 IRF is not very reliable in this region. In this spectral region, we also observe high-frequency oscillations
742 with a low amplitude that persist beyond the probed time window. Fitting the oscillations with a damped
743 sine function results in an oscillation period of approximately 91 fs, corresponding to a frequency of 367
744 cm^{-1} . We attribute this oscillation to the impulsive excitation of a symmetric vibrational mode of the
745 solvent ($\nu_3 = 365 \text{ cm}^{-1}$), which is known to have a lifetime on the picosecond scale^{si8}. Due to the average
746 IRF of 0.3 ps associated with the CA, we excluded any pump-probe delays shorter than 0.3 ps for the
747 analysis of our TA experiments.

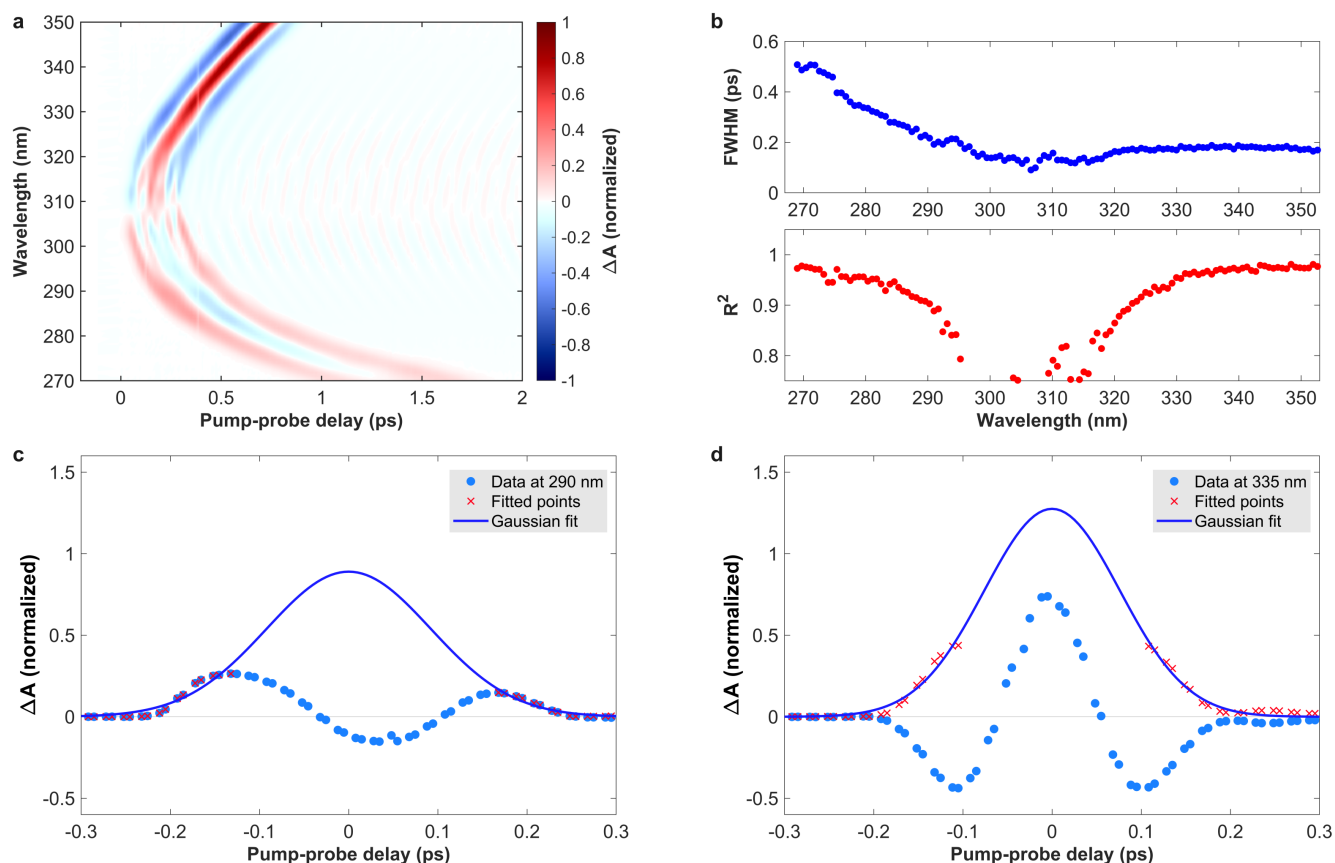


Figure S.4. Transient absorption of pure CHCl₃ excited at 530 nm. a) Time-wavelength map of the obtained data without any chirp correction. b) Results from Gaussian fits of the kinetic traces at individual probe wavelengths, displaying the resulting full-width-at-half-maximum (FWHM) and R^2 value. c,d) Selected kinetic traces, selected data points to be fitted and the resulting Gaussian fits.

748 **Pump fluence dependence.** In order to ensure that the excitation of the MLCT transition takes place
 749 in a linear regime with respect to the pump fluence, we recorded TA spectra in Fe^{CIP} as a function of pump
 750 pulse energy. The pump-probe delay was fixed at 10 ps and the pump pulse energy E was converted to
 751 peak fluence F via $F = 8E/(w^2\pi)$, assuming a Gaussian beam with a diameter w at $1/e^2$ intensity. Here
 752 we measured $w = 270\mu\text{m}$. Fig. S.5a displays the acquired spectra, which show isosbestic points at the
 753 zero crossings between the GSB and ESA bands and no observable spectral distortions for increasing
 754 pump fluence. Fig. S.5b plots the maximum TA amplitude of the main GSB and ESA band averaged over
 755 a 2 nm wide interval as a function of the pump fluence. We performed a linear fit on the data setting the
 756 y-intercept to zero and obtained an excellent correspondence with the data as evidenced by the high R^2
 757 values displayed in the figure. This confirms that the photoexcitation of the MLCT band takes place in a
 758 linear regime for the range of pump fluences measured here.

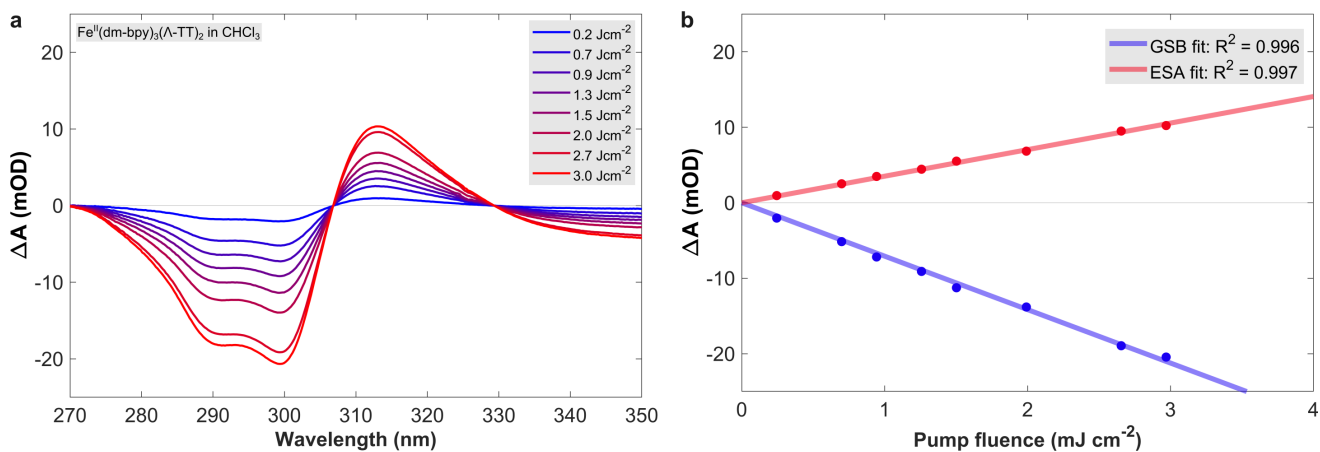


Figure S.5. a) Transient absorption of $\text{Fe}^{\text{II}}(\text{dm-bpy})_3(\Lambda\text{-TT})_2$ in CHCl_3 as a function of pump fluence at a pump-probe delay of 10 ps. b) Maximum transient absorption amplitude of the GSB and ESA band as a function of pump fluence including a linear fit of the data.

759 **TA data.** TA measurements of Fe^{CIP} , Fe^{SIP} , and Fe^{RIP} were performed back to back under identical
760 conditions. The pump pulse was centred at approximately 530 nm (the spectrum is displayed in fig. S.1)
761 and focussed to an average focal spot diameter of 270 μm with a peak fluence of 2.8 mJ cm^{-2} . The
762 TA spectrum at the so-called magic angle configuration was calculated from consecutively acquired TA
763 spectra with parallel and perpendicular pump and probe polarization configurations. Fig. S.6 displays the
764 GVD-corrected data for all three investigated samples. All samples display a pronounced ground state
765 bleach (GSB) band centred at 295 nm, taking the inverted shape of the steady-state absorption spectrum.
766 Centred near 315 nm, an excited state absorption (ESA) band is observed with a smaller amplitude and
767 an isosbestic point with the GSB band near 305 nm. This ESA band has previously been identified as
768 the red-shifted LC absorption of the photoexcited complex in its HS state^{si9, si10} and thus probes both its
769 population and the ligand system of the excited complex. Similar to the reported case of $[\text{Fe}^{\text{II}}(\text{bpy})_3]^{2+}$ in
770 aqueous solution, the absorption band of the HS state decays simultaneously with the GSB features for all
771 three samples. At wavelengths >330 nm a weak and flat GSB band emerges, which extends out of the
772 probed spectral region. The complete time-wavelength maps in fig. S.6b,d,f show pronounced coherent
773 oscillations on the main ESA band and an additional short-lived ESA band <280 nm.

774 **TA fits.** For the quantitative analysis of the TA data the OPTIMUS software package was used to
775 perform global multi-exponential fits^{si11}. Accounting for the reported photocycle in $[\text{Fe}^{\text{II}}(\text{bpy})_3]^{2+}$, a
776 sequential decay model was employed. To this end, pump-probe delays <0.3 ps were excluded from

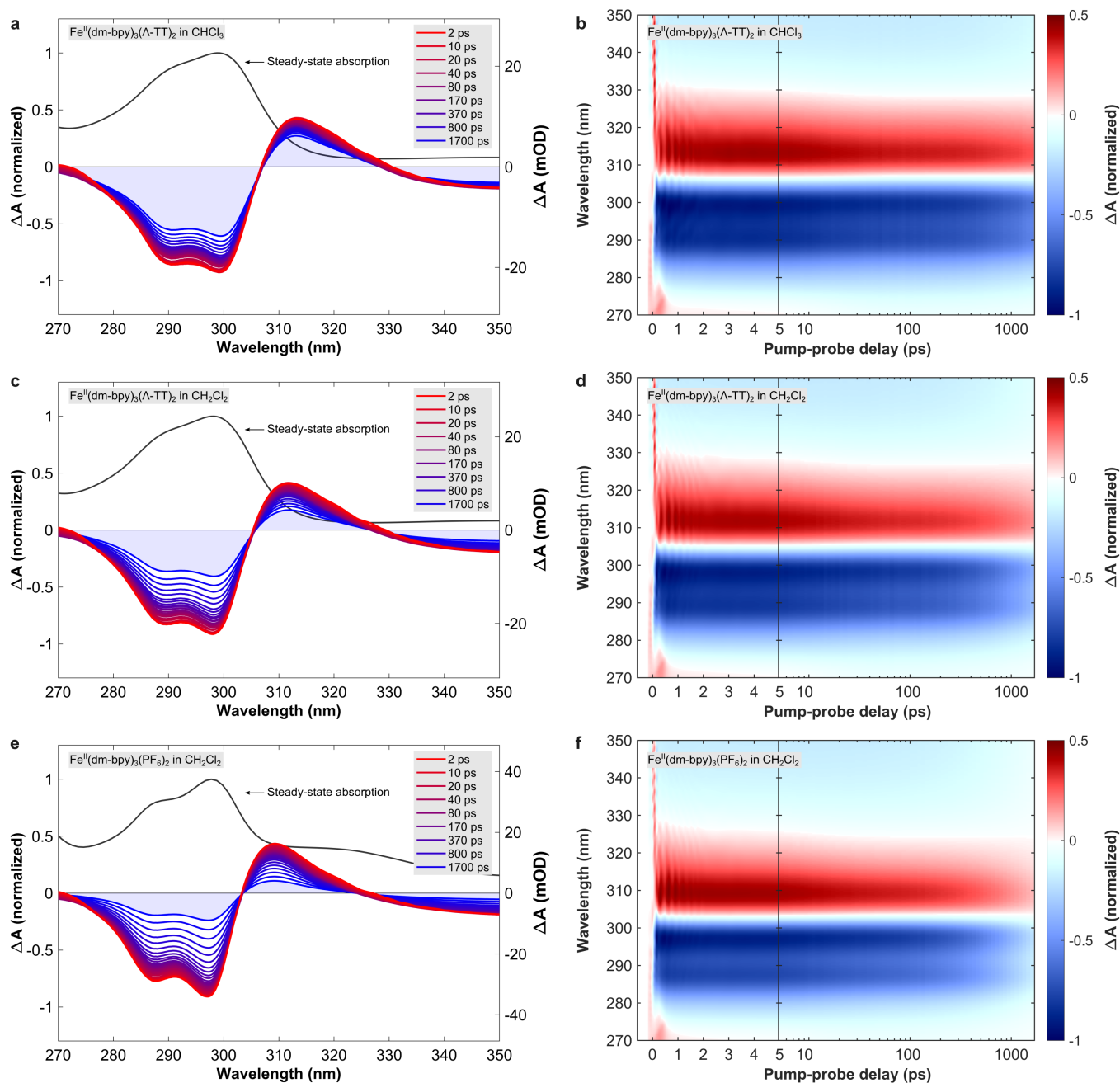


Figure S.6. Transient absorption of $\text{Fe}^{\text{II}}(\text{dm-bpy})_3(\Lambda\text{-TT})_2$ in CHCl_3 (a,b), in CH_2Cl_2 (c,d), and $\text{Fe}^{\text{II}}(\text{dm-bpy})_3(\text{PF}_6)_2$ in CH_2Cl_2 (e,f) after photoexcitation of the MLCT band.

777 the fit and the GVD-corrected TA data was fit with a series of exponential functions, convoluted with
 778 a Gaussian function corresponding to the average IRF of 0.3 ps. We found that a minimum number of
 779 three exponential functions is required to adequately fit the data. Fig. S.7 displays the obtained decay-
 780 associated spectra (DAS) and species-associated spectra (SAS), each associated with a time constant.
 781 Whereas the DAS of a decay component displays its pre-exponential amplitude as a function of probe

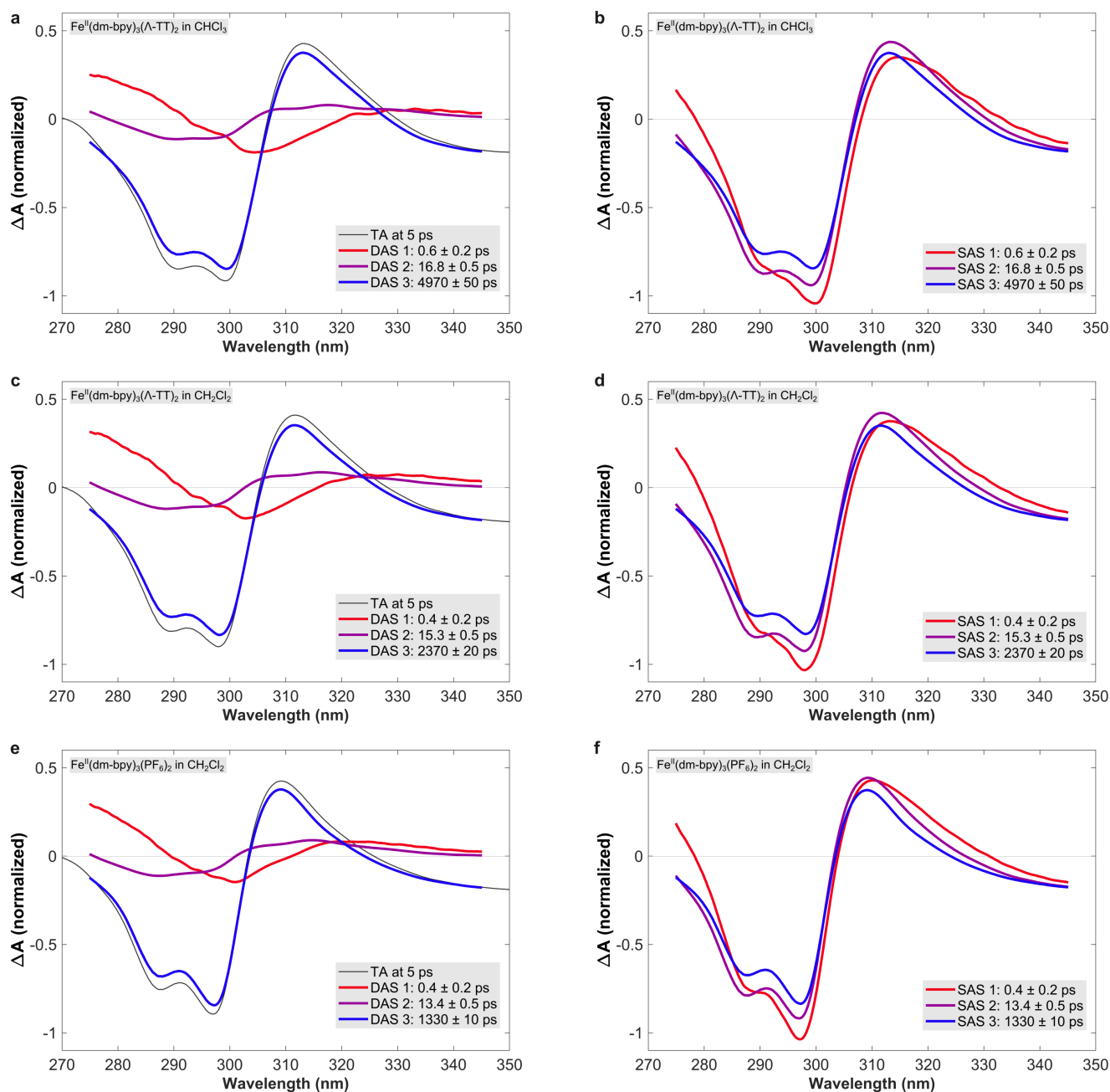


Figure S.7. Decay-associated spectra (left panels) and species-associated spectra (right panels) obtained from a global analysis of the TA data of $\text{Fe}^{\text{II}}(\text{dm-bpy})_3(\Lambda\text{-TT})_2$ in CHCl_3 (a,b), in CH_2Cl_2 (c,d), and $\text{Fe}^{\text{II}}(\text{dm-bpy})_3(\text{PF}_6)_2$ in CH_2Cl_2 (e,f) after photoexcitation of the MLCT band. For the plots of the DAS, a TA spectrum at 5 ps is included to show the positions of the GSB and ESA bands.

782 wavelength, its SAS represents the steady-state TA spectrum of the corresponding intermediate state in
 783 the sequential model. For the shortest time-constant, an error of ± 0.2 ps was estimated, accounting for
 784 the IRF and the exclusion of pump-probe delays < 0.3 ps. For the remaining two time constants, the error
 785 was estimated based on the observed variation in the fit parameters resulting from different starting values

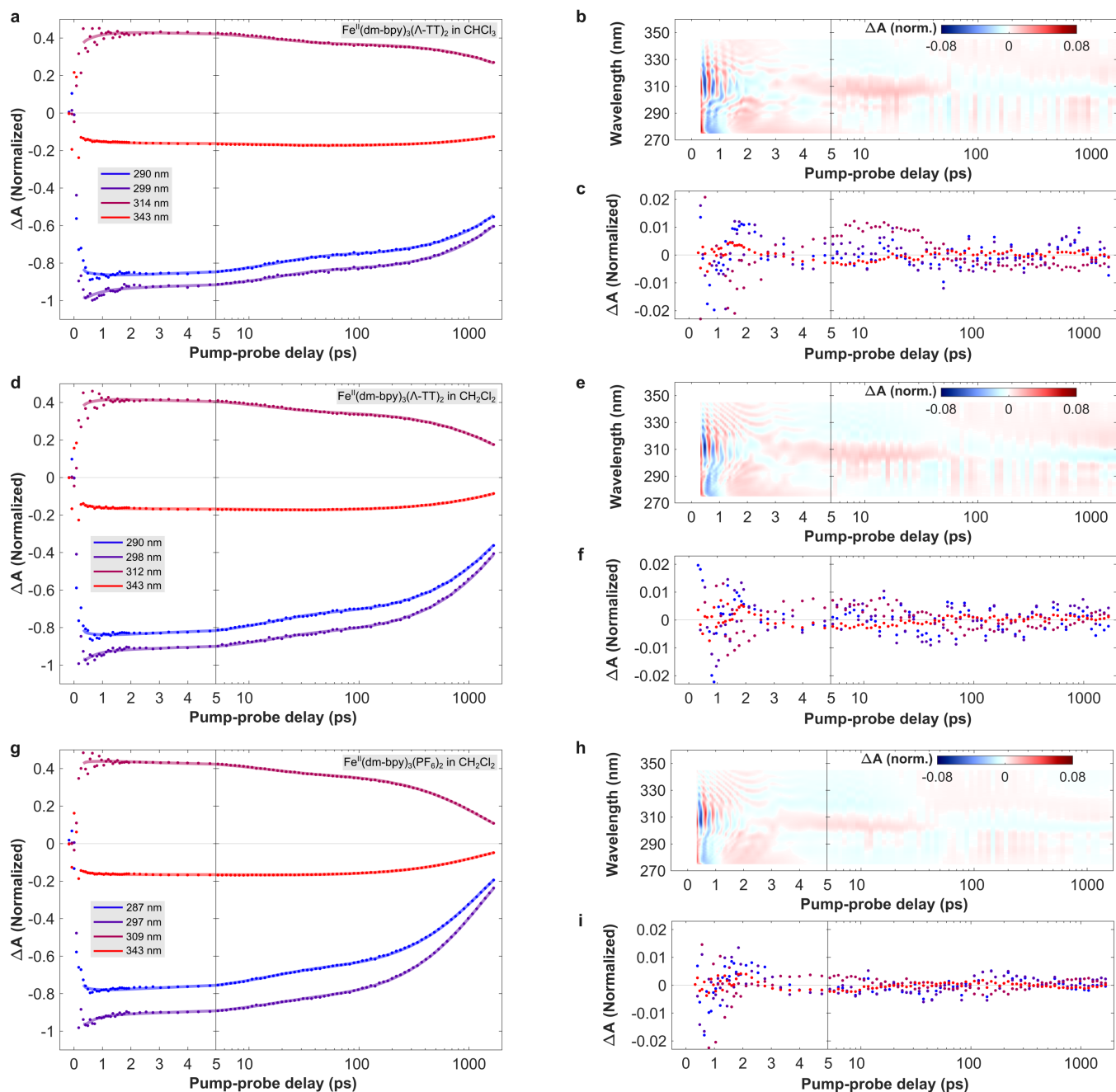


Figure S.8. Evaluation of the quality of the obtained global fits of the TA data for $\text{Fe}^{\text{II}}(\text{dm-bpy})_3(\Lambda\text{-TT})_2$ in CHCl_3 (a,b,c), in CH_2Cl_2 (d,e,f), and $\text{Fe}^{\text{II}}(\text{dm-bpy})_3(\text{PF}_6)_2$ in CH_2Cl_2 (h,i,j). The left panels display the TA amplitude as a function of pump-probe delay at selected probe wavelengths (dots) and the obtained fits (solid lines), whereas the right panels display the time-wavelength map of the residuals (top right) and the residuals for the selected kinetic traces (bottom right).

786 for the algorithm. Fig. S.8 evaluates the quality of the obtained fits through direct comparison with the
 787 data at selected probe wavelengths and through the fit residuals. For the kinetic traces displayed in fig.
 788 S.8a,d,g, probe wavelengths near the maximum of the probed GSB and ESA bands were selected. The

789 corresponding TA amplitude was averaged over three adjacent detector pixels, corresponding to a spectral
790 width of approximately 0.5 nm. The chosen spectral positions were adapted for each sample and are
791 indicated in the figure legend. In all cases, an excellent correspondence between the data and the fits
792 is observed. Fig. S.8b,e,h displays the obtained residuals over the entire probe wavelength spectrum,
793 whereas fig. S.8c,f,i shows the residuals for the selected kinetic traces. Their low value across the probed
794 spectral and temporal range confirms the high quality of the obtained global fits. Note that the fits do not
795 account for the coherent oscillations in the ESA band for pump-probe delays < 2 ps, which are therefore
796 present in the residuals. For Fe^{CIP} , the obtained time constants are $\tau_1^{\text{CIP}} = 0.6 \pm 0.2$ ps, $\tau_2^{\text{CIP}} = 16.8 \pm 0.5$
797 ps, and $\tau_3^{\text{CIP}} = 4970 \pm 50$ ps. Fig. S.7a,b displays the associated DAS and SAS, with DAS_1 showing a
798 negative band near 305 nm and positive bands on either side. The associated spectral changes in the TA
799 data correspond to the transition from SAS_1 to SAS_2 : a decay of a positive feature > 290 nm coupled to the
800 rise of a positive feature between 290 nm and 320 nm, which leads to slight blue-shift of the zero-crossing
801 between the GSB and ESA bands. DAS_2 displays a negative band in the GSB region and a positive band
802 in the ESA region, thereby describing a minor decay of both bands with minor changes of their spectral
803 shapes. DAS_3 then takes a shape close to the TA spectrum, implying a simultaneous decay of all TA
804 features to zero with the time constant τ_3 . Due to the much larger amplitude of DAS_3 compared to the
805 other two components, τ_3 accounts for most of the decay in the probed TA bands. Compared to Fe^{CIP} ,
806 the global analysis of the TA data for Fe^{SIP} and Fe^{RIP} gives DAS and SAS with identical spectral features
807 yet successively shorter time constants. For their values we obtain $\tau_1^{\text{SIP}} = 0.4 \pm 0.2$, $\tau_2^{\text{SIP}} = 15.3 \pm 0.5$ ps
808 and $\tau_3^{\text{SIP}} = 2370 \pm 20$ ps for Fe^{SIP} , and $\tau_1^{\text{RIP}} = 0.4 \pm 0.2$, $\tau_2^{\text{RIP}} = 13.4 \pm 0.5$ ps and $\tau_3^{\text{RIP}} = 1330 \pm 10$ ps
809 for Fe^{RIP} . This indicates that the same relaxation processes are taking place on faster time scales.

810 **TA of $\text{Fe}^{\text{II}}(\text{bpy})_3\text{Cl}_2$ in H_2O .** In order to unambiguously assign the excited state dynamics in the
811 investigated samples, we conducted benchmark measurements of the well-studied $\text{Fe}^{\text{II}}(\text{bpy})_3\text{Cl}_2$ in H_2O .
812 The experimental conditions and data analysis procedures were identical to those for Fe^{CIP} , Fe^{SIP} , and
813 Fe^{RIP} . Fig. S.9a displays the TA time-wavelength map, normalized to the maximum GSB signal,
814 whereas fig. S.9b shows the DAS obtained from a sequential multi-exponential fit convoluted with the
815 IRF of the measurement. Fig. S.9c displays the TA amplitude as a function of pump-probe delay at
816 selected probe wavelengths and includes the obtained fit functions as solid lines, whereas fig. S.9d,e

817 shows the corresponding fit residuals. The agreement between the data and the fit is excellent, which is
 818 further supported by the low amplitude of the residuals. For the three decay components we obtained
 819 $\tau_1^{\text{H}_2\text{O}} = 0.4 \pm 0.2$ ps, $\tau_2^{\text{H}_2\text{O}} = 3.3 \pm 0.2$ ps, and $\tau_3^{\text{H}_2\text{O}} = 680 \pm 10$ ps. These values agree very well with a
 820 study by Consani *et al.*^{si9}, who found two components on the picosecond scale in the same spectral region
 821 with the values 3.4 ± 1.2 ps and 675 ± 25 ps. These were assigned to vibrational cooling and electronic
 822 decay of the HS state, respectively. The one-to-one correspondence of the associated DAS with those
 823 obtained for Fe^{CIP} , Fe^{SIP} , and Fe^{RIP} enables a direct assignment of the excited state dynamics with τ_2 and
 824 τ_3 denoting the vibrational cooling and electronic decay of the HS state, respectively. This is consistent
 825 with the spectral shape of the respective DAS components, as DAS_3 describes a simultaneous decay of all
 826 GSB and HS absorption features to zero, whereas the sign change of DAS_2 is consistent with a narrowing
 827 of the HS absorption band due to vibrational energy redistribution^{si9}. The sub-picosecond component τ_1
 828 is thus assigned to the HS state formation dynamics. However, the quantitative information contained in
 829 τ_1 is limited by the 0.3 ps average IRF and the data analysis procedure of the TA experiments and is thus
 830 omitted from this discussion.

Sample	τ_1 (ps)	τ_2 (ps)	τ_3 (ps)	ρ_1 (ps)	ρ_2 (ps)	ϕ (ps)
$\Lambda\text{-Fe}^{\text{CIP}}$	0.6 ± 0.2	16.8 ± 0.5	4970 ± 50	4.8 ± 0.2	520 ± 10	80 ± 10
$\Lambda\text{-Fe}^{\text{SIP}}$	0.4 ± 0.2	15.3 ± 0.5	2370 ± 20	3.6 ± 0.2	260 ± 10	70 ± 10
Fe^{RIP}	0.4 ± 0.2	13.4 ± 0.5	1330 ± 10	1.6 ± 0.2	110 ± 10	-
$\text{Fe}^{\text{II}}(\text{bpy})_3\text{Cl}_2$ in H_2O	0.4 ± 0.2	3.3 ± 0.2	680 ± 10	-	-	-

Table S.3. Time constants obtained from various multi-exponential fits of the time-resolved data from all conducted experiments. The constants τ_i ($i = 1,2,3$) were obtained from the TA experiments, whereas ρ_i and ϕ were obtained from the TAA and TRCD experiments, respectively.

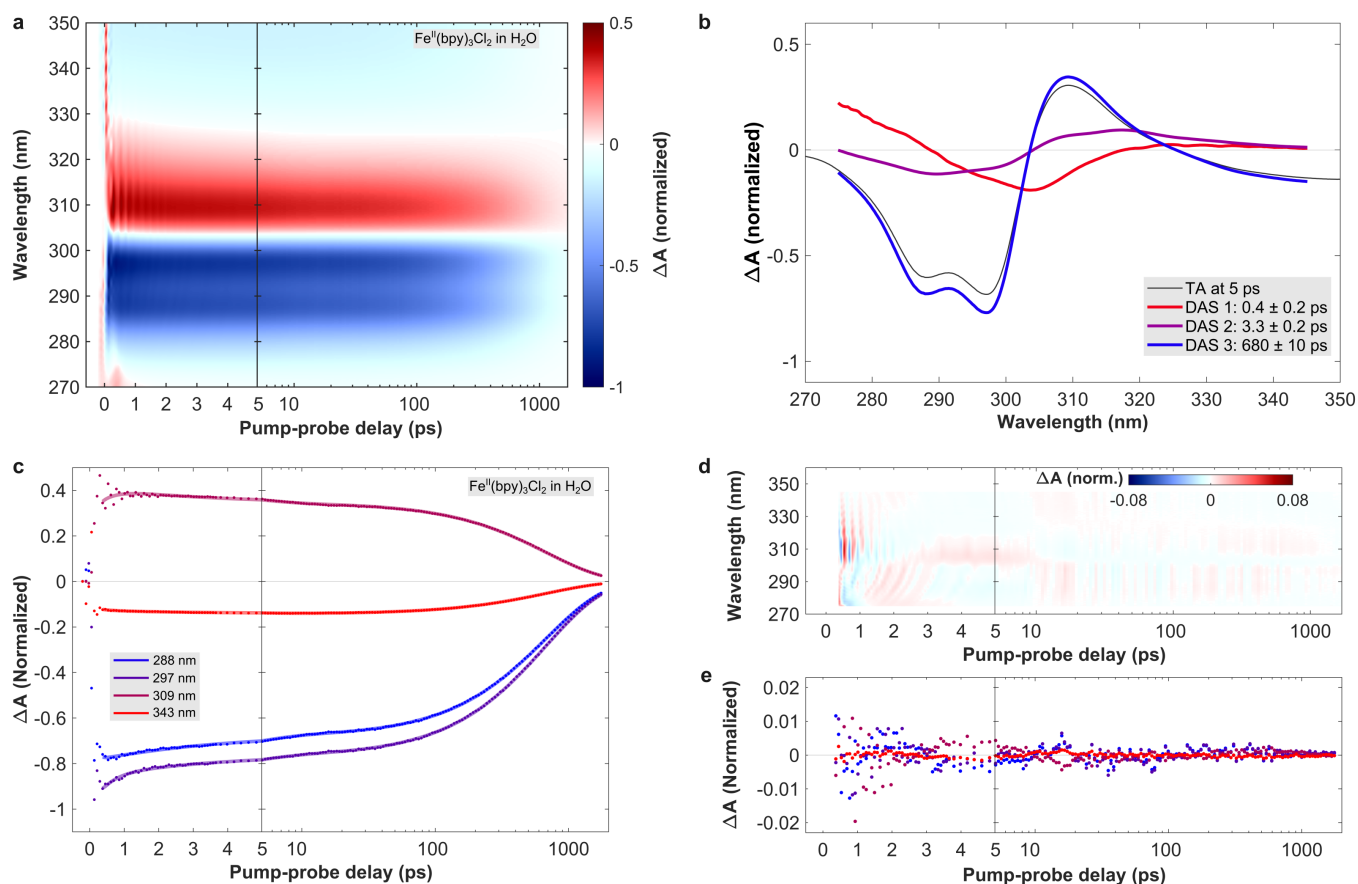


Figure S.9. Transient absorption of $\text{Fe}^{\text{II}}(\text{bpy})_3\text{Cl}_2$ in H_2O , after photoexcitation of the MLCT band near 530 nm (a) and the decay-associated spectra obtained from a global analysis of the TA data (b). Evaluation of the quality of the obtained global fits by comparing the TA data at selected probe wavelengths (dots) to the fits (solid lines) (c) and by displaying the obtained fit residuals (d,e).

831 **S.3 Transient anisotropy data and analysis**

832 **TAA data.** As pointed out in the Methods section, the TAA spectra of Fe^{CIP} , Fe^{SIP} , and Fe^{RIP} were
 833 calculated from the same data sets that were used to calculate the TA spectra presented in the previous
 834 section. Fig. S.10 thus displays the obtained TAA spectra as a function of pump-probe delay for all three
 samples.

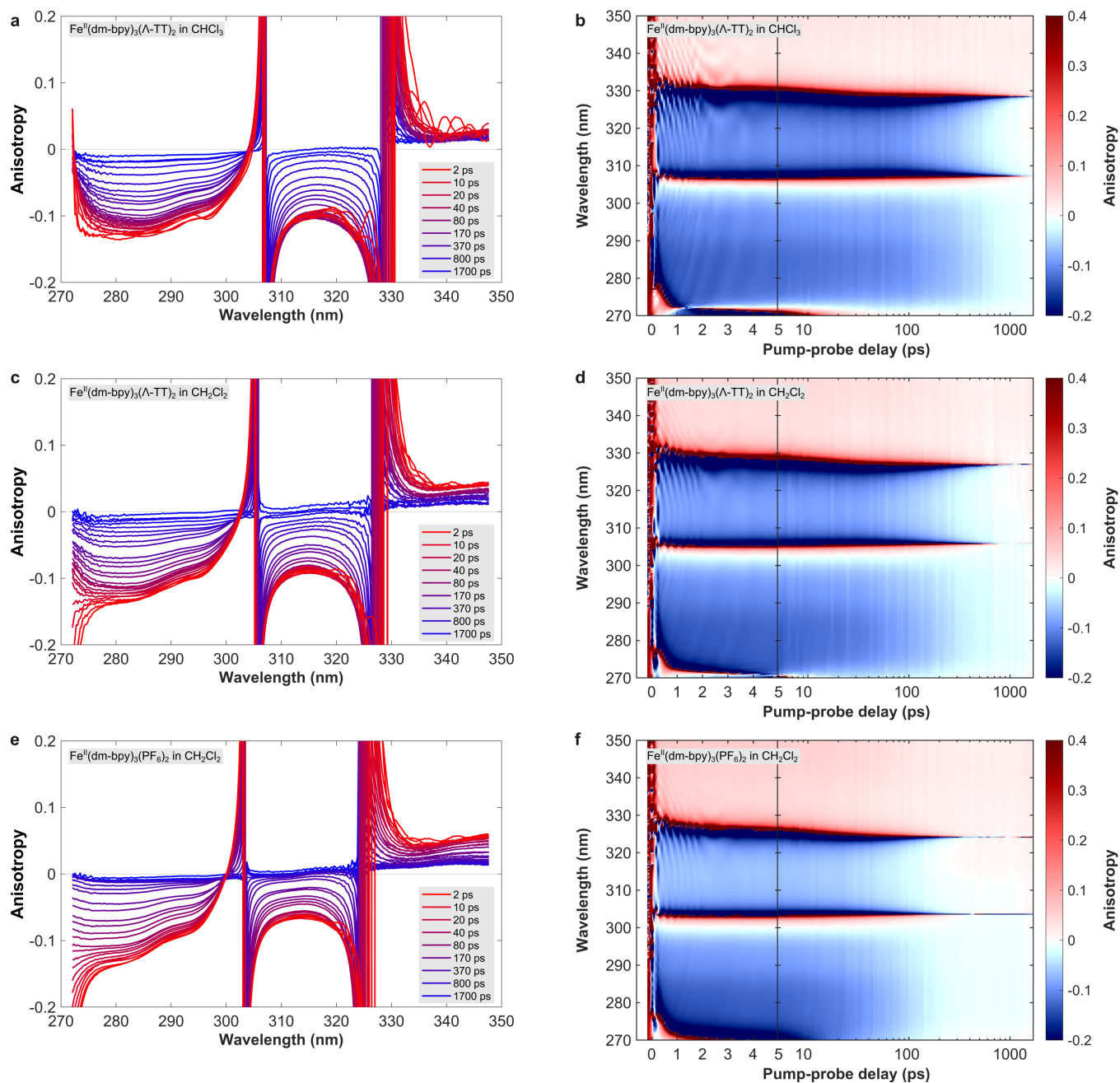


Figure S.10. Transient absorption anisotropy of $\text{Fe}^{\text{II}}(\text{dm-bpy})_3(\Delta\text{-TT})_2$ in CHCl_3 (a,b), in CH_2Cl_2 (c,d), and $\text{Fe}^{\text{II}}(\text{dm-bpy})_3(\text{PF}_6)_2$ in CH_2Cl_2 (e,f) after photoexcitation of the MLCT band.

836 **TAA fits.** For the quantitative analysis of the TAA data the OPTIMUS software package was used to
837 perform global multi-exponential fits. As the calculation of the TAA spectra involves the TA spectrum as
838 a denominator, the TAA amplitude diverges when the TA amplitude takes values close to zero. This is the
839 case at probe wavelengths near zero-crossings between GSB and ESA bands, at early pump-probe delays
840 due to cross-phase modulation (see section on the IRF determination) and at late pump-probe delays where
841 the excited state population approaches zero. For the performed global fits we accounted for all three
842 factors by excluding probe wavelengths near zero-crossings and by excluding pump-probe delays <0.4 ps.
843 Since each sample displayed different excited state lifetimes, the longest pump-probe delay t_{\max} included
844 in the global fit was adapted accordingly, such that $t_{\max}^{\text{CIP}} \approx 1000$ ps, $t_{\max}^{\text{SIP}} \approx 500$ ps, and $t_{\max}^{\text{RIP}} \approx 200$ ps. We
845 found that a minimum number of two exponential functions are required to fit the TAA data, both in a fit
846 model with parallel and sequential decays. Here we found identical time constants and DAS independent
847 of the fit model, which is typically the case when the obtained time constants differ by more than an order
848 of magnitude. Fig. S.11 thus only displays the obtained DAS and SAS for a sequential fit model. Note that
849 their spectral widths directly denote the probe wavelength ranges that were included in the global fits of
850 each sample. The error ranges for the obtained time constants were estimated by observing their variation
851 when shifting the included probe wavelength region and pump-probe delay t_{\max} . Fig. S.12 evaluates the
852 quality of the obtained fits through direct comparison with the data at selected probe wavelengths and the
853 fit residuals. For the kinetic traces displayed in fig. S.12a,d,g, probe wavelengths near the maximum of the
854 probed GSB and ESA bands were selected. The corresponding TAA amplitude was averaged over three
855 adjacent detector pixels, corresponding to a spectral width of approximately 0.5 nm. The chosen spectral
856 positions were adapted for each sample and are indicated in the figure legend. In all cases, a very good
857 correspondence between the data and the fits is observed. Fig. S.8b,e,h displays the obtained residuals
858 over the included probe wavelength ranges, whereas fig. S.8c,f,i shows the residuals for the selected
859 kinetic traces. Their comparatively low values across the included spectral and temporal range confirms
860 the high quality of the obtained global fits. Note that the residuals in the ESA band display oscillations for
861 pump-probe delays <2 ps, which are also visible in the raw data in fig. S.10. We attribute these oscillations
862 to the coherent oscillations observed in the ESA band's TA kinetics, which are not accounted for by the
863 global fits of the TAA data.

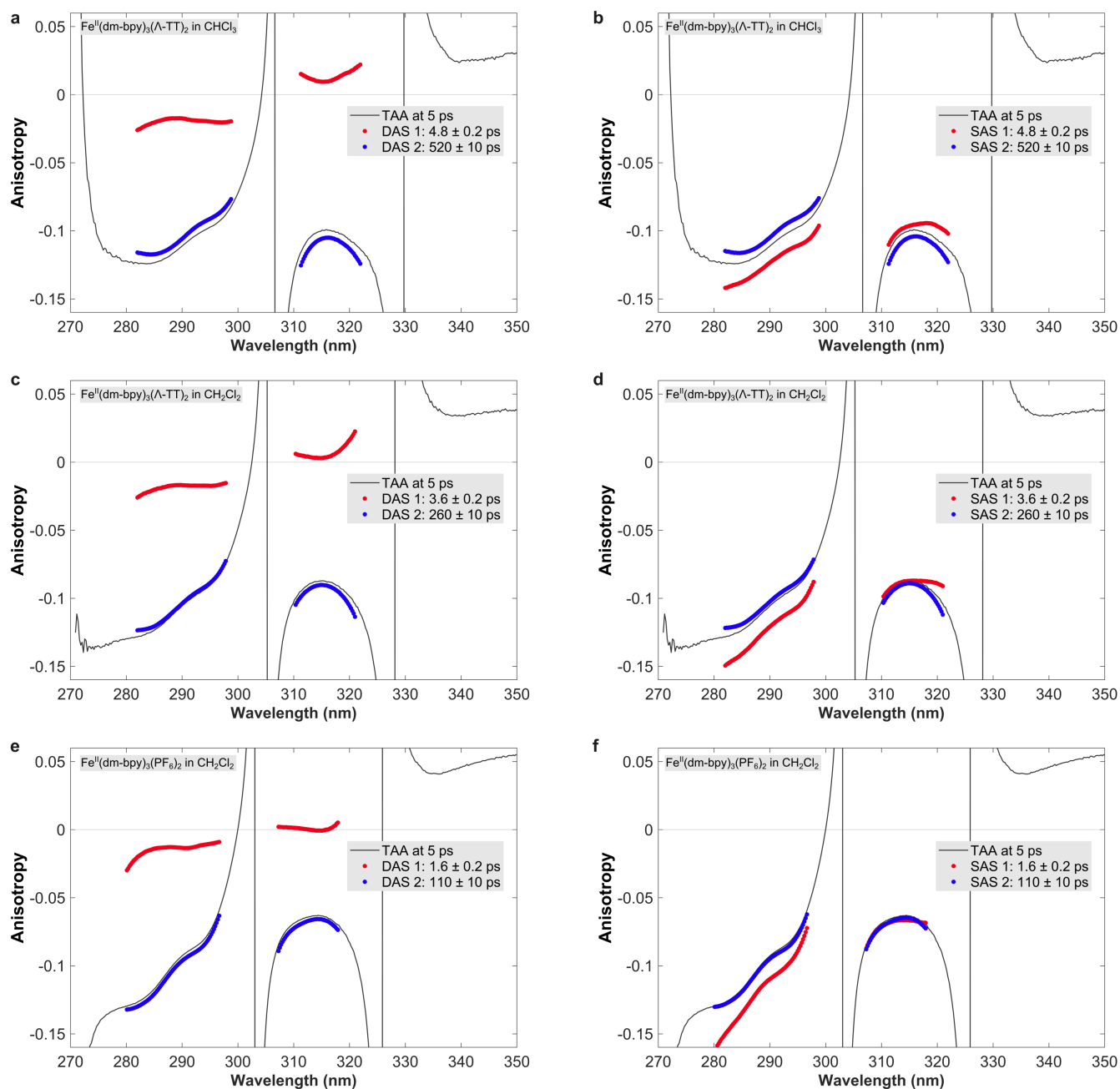


Figure S.11. Decay-associated spectra (left panels) and species-associated spectra (right panels) obtained from a global analysis of the TAA data of $\text{Fe}^{\text{II}}(\text{dm-bpy})_3(\Lambda\text{-TT})_2$ in CHCl_3 (a,b), in CH_2Cl_2 (c,d), and $\text{Fe}^{\text{II}}(\text{dm-bpy})_3(\text{PF}_6)_2$ in CH_2Cl_2 (e,f) after photoexcitation of the MLCT band. For both the DAS and the SAS, a TAA spectrum at 5 ps is included to show the positions of the main TAA bands and zero-crossings.

864 **TAA calculations.** For the interpretation of the TAA data, we calculated the TAA values expected
 865 from the octahedral coordination environment of a tris-chelate complex. We then calculated the TAA as a
 866 function of the angular deviation of the ligands from this configuration and estimated the average TAA

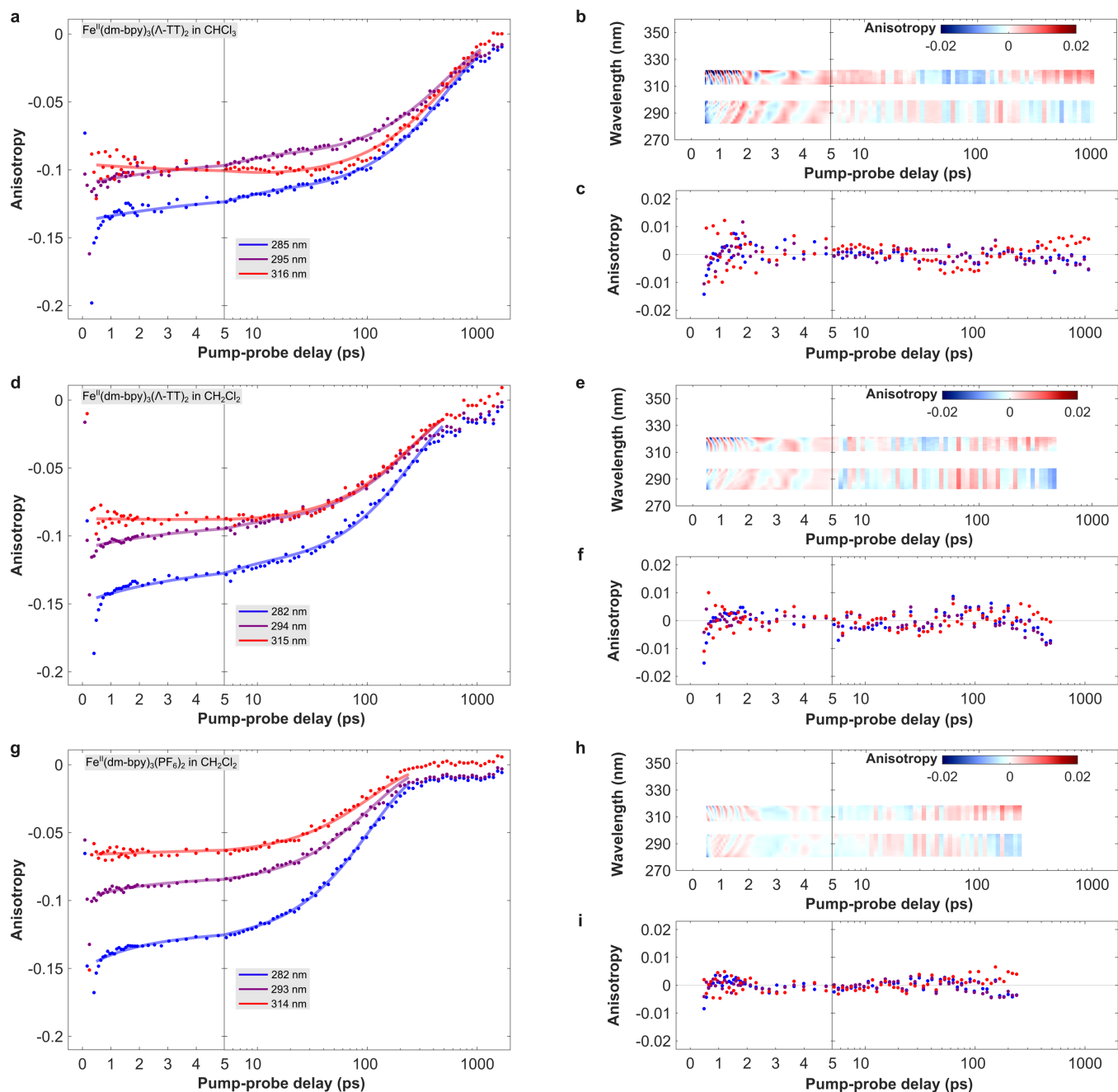


Figure S.12. Evaluation of the quality of the obtained global fits of the TAA data for $\text{Fe}^{\text{II}}(\text{dm-bpy})_3(\Lambda\text{-TT})_2$ in CHCl_3 (a,b,c), in CH_2Cl_2 (d,e,f), and $\text{Fe}^{\text{II}}(\text{dm-bpy})_3(\text{PF}_6)_2$ in CH_2Cl_2 (g,h,i). The left panels display the TA amplitude as a function of pump-probe delay at selected probe wavelengths (dots) and the obtained fits (solid lines), whereas the right panels display the time-wavelength map of the residuals (top right) and the residuals for the selected kinetic traces (bottom right).

867 resulting from an increasingly broader conformational distribution. To this end, we take the procedure
 868 developed by Wallin and co-workers for an iso-structural $[\text{Ru}(\text{bpy})_3]^{2+}$ complex as a starting point^{si12} and
 869 then add the required rotational degrees of freedom. The inset in fig. S.13a displays the chosen coordinate

870 system and the resulting arrangement of the relevant MLCT and LC transition dipoles denoted as \vec{M}_i and
 871 \vec{L}_i , respectively. Here subscript $i = 1, 2, 3$ is associated with the ligands of the tris-chelate complex as
 872 shown in the coordinate system. Note that for each ligand, both the MLCT and LC transition dipoles are
 873 confined to the ligand plane and are oriented perpendicularly to each other. Whilst the MLCT transition is
 874 directed away from the metal centre, the LC transition is assumed to be aligned along the long-axis of
 875 the bipyridine ligand. Within this reference frame, we obtain the following vector expressions for the
 876 transition dipoles in their original octahedral arrangement:

$$\vec{M}_1 = \frac{1}{\sqrt{2}}(\hat{e}_x - \hat{e}_y), \quad \vec{L}_1 = \frac{1}{\sqrt{2}}(\hat{e}_x + \hat{e}_y) \quad (1)$$

$$\vec{M}_2 = \frac{1}{\sqrt{2}}(-\hat{e}_x + \hat{e}_z), \quad \vec{L}_2 = \frac{1}{\sqrt{2}}(\hat{e}_x + \hat{e}_z) \quad (2)$$

$$\vec{M}_3 = \frac{1}{\sqrt{2}}(\hat{e}_y - \hat{e}_z), \quad \vec{L}_3 = \frac{1}{\sqrt{2}}(\hat{e}_y + \hat{e}_z) \quad (3)$$

877 Note that all vectors are of unit length. We now introduce two rotational degrees of freedom to each LC
 878 transition dipole: 1) a rotation angle θ of \vec{L}_i out of its ligand plane with \vec{M}_i as the rotation axis, and 2) a
 879 rotation angle δ of \vec{L}_i in its ligand plane around the metal-centre. We can then use the standard rotation
 880 matrices $\mathbf{R}_x(\delta)$, $\mathbf{R}_y(\delta)$, $\mathbf{R}_z(\delta)$ to perform the rotation of \vec{L}_i by δ around the respective coordinate axes,
 881 and apply the well known Rodrigues' rotation formula to perform a rotation of \vec{L}_i around \vec{M}_i by an angle
 882 θ . We then obtain the following expressions for the rotated LC transition dipoles $\vec{L}_i(\theta, \delta)$:

$$\vec{L}_1(\theta, \delta) = \mathbf{R}_z(\delta) \cdot \left(\vec{L}_1 \cos \theta + (\vec{M}_1 \times \vec{L}_1) \sin \theta + \vec{M}_1 (\vec{M}_1 \cdot \vec{L}_1) (1 - \cos \theta) \right) \quad (4)$$

$$\vec{L}_2(\theta, \delta) = \mathbf{R}_y(\delta) \cdot \left(\vec{L}_2 \cos \theta + (\vec{M}_2 \times \vec{L}_2) \sin \theta + \vec{M}_2 (\vec{M}_2 \cdot \vec{L}_2) (1 - \cos \theta) \right) \quad (5)$$

$$\vec{L}_3(\theta, \delta) = \mathbf{R}_x(\delta) \cdot \left(\vec{L}_3 \cos \theta + (\vec{M}_3 \times \vec{L}_3) \sin \theta + \vec{M}_3 (\vec{M}_3 \cdot \vec{L}_3) (1 - \cos \theta) \right) \quad (6)$$

883 Without loss of generality, we now assume that the initial photoexcitation takes place via \vec{M}_1 . The
 884 expected TAA value obtained from a single LC transition dipole rotated by θ and δ from its original

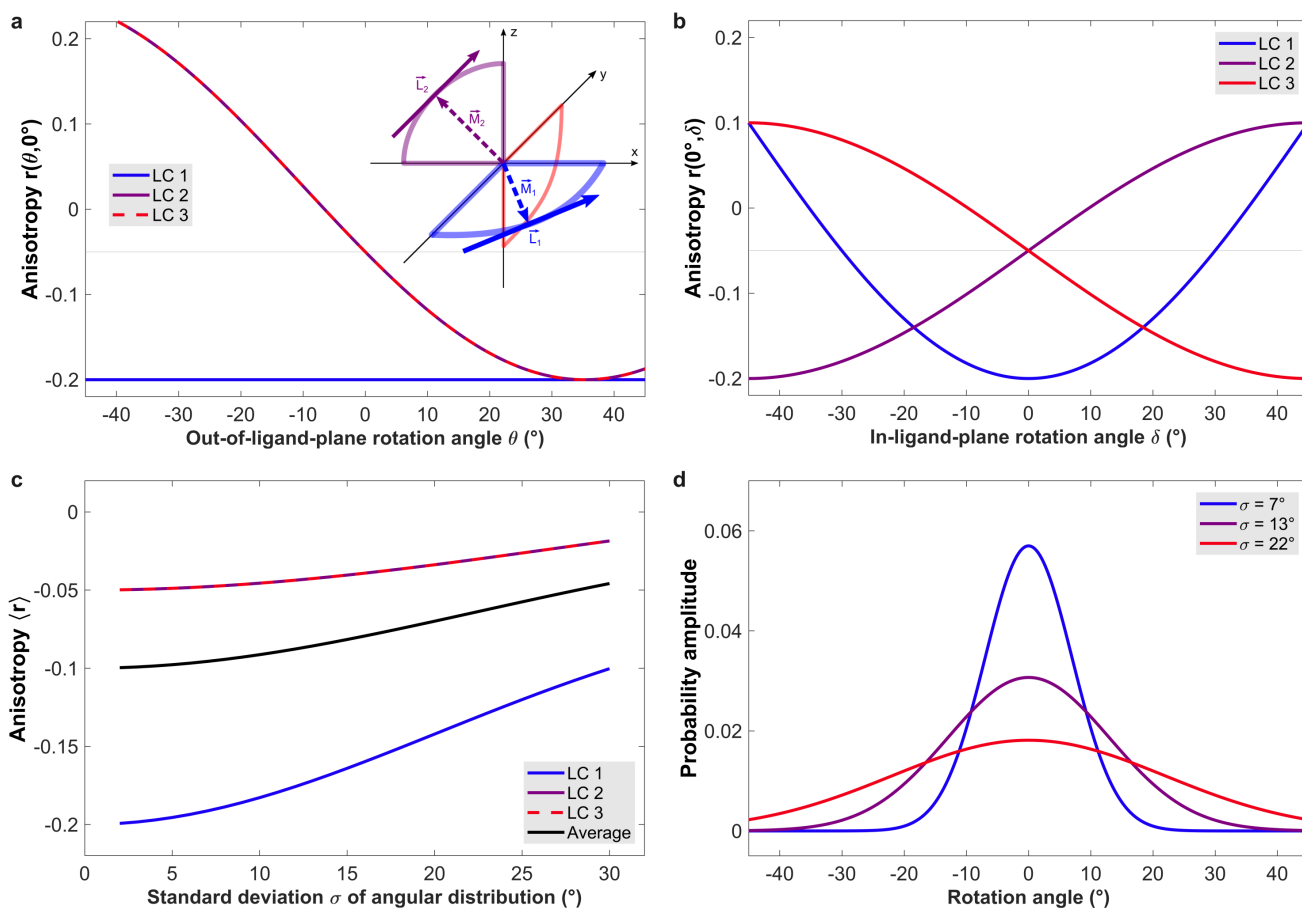


Figure S.13. Calculation of expected anisotropy values from the long-axis ligand centred (LC) transition dipoles of a tris-chelate complex photoexcited via one of its MLCT transitions (here: \vec{M}_1 on ligand 1). a) Anisotropy calculated for individual LC transition dipoles as a function of their out-of-ligand-plane rotation angle. The inset displays the employed coordinate system and the labelling of the transition dipoles. b) Anisotropy calculated for individual LC transition dipoles as a function of their in-ligand-plane rotation angle around the origin of the coordinate system. c) Anisotropy obtained from a conformational ensemble over the in- and out-of-ligand-plane rotation angles as a function of the standard deviation of the associated two-dimensional Gaussian distribution. The average anisotropy value (solid black line) corresponds to the value obtained in an experimental measurement. d) One-dimensional Gaussian distributions with selected standard deviations, illustrating the conformational ensembles associated with the anisotropy values measured in the presented experiments.

885 octahedral arrangement can now be expressed as:

$$r_i(\theta, \delta) = \frac{3[\vec{M}_1 \cdot \vec{L}_i(\theta, \delta)]^2 - 1}{5} \quad (7)$$

886 Fig. S.13a displays the resulting TAA values for all three LC transition dipoles as function of θ whilst

887 keeping $\delta = 0^\circ$. For ligand 1, any out-of-ligand-plane rotation of \vec{L}_1 preserves the perpendicular align-
 888 ment with \vec{M}_1 , such that $r_1(\theta, 0) = -0.2$, as expected. Due to the symmetry of the complex, we then
 889 obtain $r_2(\theta, 0^\circ) = r_3(\theta, 0^\circ)$, with $r_2(0^\circ, 0^\circ) = r_3(0^\circ, 0^\circ) = -0.05$ for the original octahedral arrangement.
 890 Importantly, we can directly see that $r_2(\theta, 0^\circ)$ and $r_3(\theta, 0^\circ)$ are not symmetric with respect to $\theta = 0^\circ$, such
 891 that $\frac{1}{2} \left(r_{2,3}(\theta, 0^\circ) + r_{2,3}(-\theta, 0^\circ) \right) > -0.05$ for the angular range plotted here ($|\theta| < 45^\circ$). This implies
 892 that any symmetric conformational distribution around $\theta = 0^\circ$ will lead to an increase in the average TAA
 893 measured from $\vec{L}_{2,3}$, with the TAA value obtained from \vec{L}_1 being unaffected by the distribution.

894 Fig. S.13b shows the analogous TAA values for all three LC transition dipoles as function of δ and
 895 keeping $\theta = 0^\circ$. For ligand 1, any in-ligand-plane rotation of \vec{L}_1 will move its orientation away from a
 896 perpendicular towards a parallel orientation with \vec{M}_1 . This implies that $\frac{1}{2} \left(r_1(0^\circ, \delta) + r_1(0^\circ, -\delta) \right) > -0.2$
 897 for the considered angular range ($|\delta| < 45^\circ$). Both $r_{2,3}(0^\circ, \delta)$ are now symmetric with respect to $\delta = 0^\circ$,
 898 such that $\frac{1}{2} \left(r_{2,3}(0^\circ, \delta) + r_{2,3}(0^\circ, -\delta) \right) = -0.05$ for the considered angular range. This implies that any
 899 symmetric conformational distribution around $\delta = 0^\circ$ will lead to an increase in the average TAA measured
 900 from \vec{L}_1 , with the TAA values obtained from $\vec{L}_{2,3}$ remaining unaffected by the distribution. Combined
 901 with the results obtained for out-of-plane rotations, we can summarize that any rotationally symmetric
 902 conformational ensemble around $\theta = \delta = 0^\circ$ will increase the measured TAA for each of the three LC
 903 transitions.

904 To gain further quantitative information, we calculated the TAA values for each LC transition, assuming
 905 a two-dimensional Gaussian distribution of rotation angles around $\theta = \delta = 0^\circ$ in each case. For the
 906 conformational averages of the resulting TAA values we then obtain:

$$\langle r_i \rangle(\sigma_\theta, \sigma_\delta) = \frac{1}{2\pi\sigma_\theta\sigma_\delta} \int_{-\theta_0}^{\theta_0} \int_{-\delta_0}^{\delta_0} r_i(\theta, \delta) \exp \left\{ - \left(\frac{\theta^2}{2\sigma_\theta^2} + \frac{\delta^2}{2\sigma_\delta^2} \right)^2 \right\} d\theta d\delta, \quad (8)$$

907 where $\sigma_\theta, \sigma_\delta$ denote the standard deviations of the Gaussian distribution and $[-\theta_0, \theta_0], [-\delta_0, \delta_0]$ the
 908 numerical integration boundaries for the calculation. We then calculated $\langle r_i \rangle(\sigma_\theta, \sigma_\delta)$ as a function of
 909 $\sigma_\theta = \sigma_\delta = \sigma$, setting $\theta_0 = \delta_0 = 90^\circ$ and $d\theta = d\delta = 0.25^\circ$ for the numerical integration. We then obtained
 910 the average TAA value measured in an experiment resulting from from all three ligands by assuming a

911 randomized excited state, such that:

$$\langle r \rangle(\sigma, \sigma) = \frac{1}{3} \left(\langle r_1 \rangle(\sigma, \sigma) + \langle r_2 \rangle(\sigma, \sigma) + \langle r_3 \rangle(\sigma, \sigma) \right) \quad (9)$$

912 Fig. S.13c displays the obtained conformational averages as a function of the standard deviation σ .
913 We observe that in an experiment, we would obtain $\langle r \rangle = -0.1$ for an infinitely narrow conformational
914 ensemble around the octahedral configuration of the tris-chelate complex. Increasing the width of the
915 conformational ensemble for each ligand then leads to a monotonous increase of $\langle r \rangle$, which reaches a
916 value of approximately -0.05 for $\sigma \approx 30^\circ$. Through this calculation we are now able to correlate the
917 initially measured anisotropy of the HS state with the standard deviation σ of the conformational ensemble
918 of its ligand system around an octahedral configuration. Recalling the experimentally determined values
919 $r_0^{\text{CIP}} = -0.96$, $r_0^{\text{SIP}} = -0.87$, and $r_0^{\text{RIP}} = -0.66$, we obtain $\sigma^{\text{CIP}} \approx 7^\circ$, $\sigma^{\text{SIP}} \approx 13^\circ$, and $\sigma^{\text{RIP}} \approx 22^\circ$. Fig.
920 S.13d then plots one-dimensional Gaussian angular distributions with these standard deviations for a
921 visual comparison. It is likely that the quantitative accuracy of the obtained conformational ensembles is
922 limited due to the simplicity of the presented calculations. Nevertheless, our calculations clearly show
923 that the chiral ion-pairing interaction strongly narrows the conformational distribution of the individual
924 ligands, such that Fe^{CIP} is best described as a nearly rigid complex in an octahedral configuration.

925 S.4 Time-resolved circular dichroism data and analysis

926 The experimental setup and measurement conditions for the time-resolved circular dichroism (TRCD)
927 experiments are reported in the Methods section. Here we report additional data sets and technical details
928 to support the discussion in the main article.

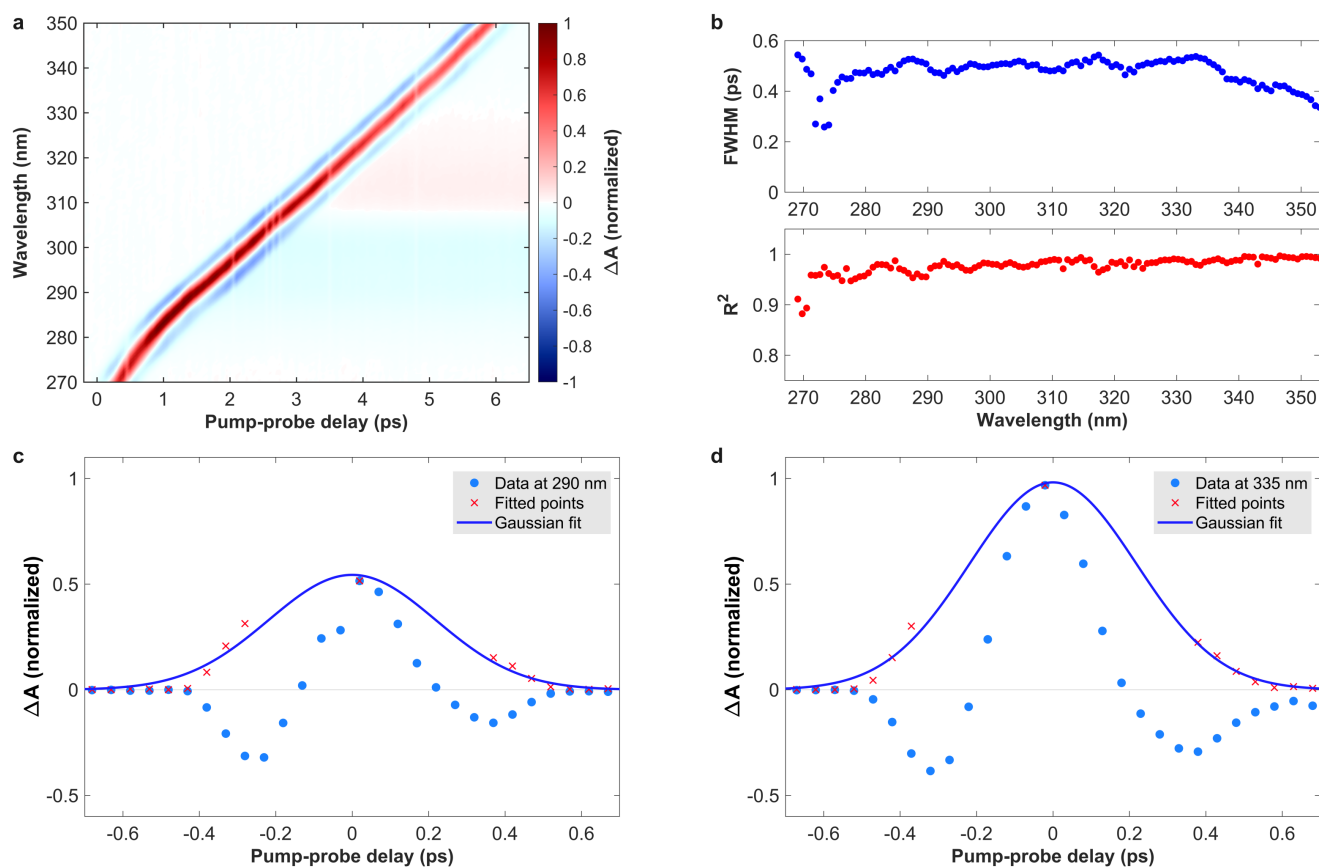


Figure S.14. Transient absorption in pure CHCl₃ excited at 530 nm, measured with left-circularly polarized probe pulses in the TRCD setup. a) Time-wavelength map of the obtained data without any chirp correction. b) Results of Gaussian fits of the kinetic traces at individual probe wavelengths, displaying the resulting full-width-at-half-maximum (FWHM) and R^2 value. c,d) Selected kinetic traces, selection of data to be fitted and the resulting Gaussian fits.

929 **Instrument response function.** The time resolution of the TRCD experiments was determined by
930 recording the instantaneous response of neat CHCl₃ in a 0.5 mm pathlength cell with ultrathin drilled
931 windows (Starna). Fig. S.14a displays the associated TA data, recorded with left-circularly polarized
932 probe pulses and a linearly polarized pump pulse. Due to the large amount of glass in the probe beam path,
933 the GVD of the probe pulses covers approximately 6 ps, with the arrival time of each probe wavelength
934 slice taking a nearly linear dependence with respect to the probe wavelength. Note that a very weak,

935 long-lived TA signal is observed that resembles the signal from the Fe^{II} complexes. This is attributed to
 936 minor impurities from the Fe^{II} samples remaining in the flow system after completion of the reported
 937 experiments. Following the fitting routine applied in section S.2, the IRF of the experiment was estimated
 938 via the width of the coherent artifact at each probe wavelength slice. Fig. S.14b displays the FWHM of
 939 the associated Gaussian fits as a function of probe wavelength and fig. S.14c,d display example fits at
 940 selected probe wavelengths. The performed fits show that the average IRF is approximately 0.5 ps across
 941 the probed wavelength window. However, for recording TRCD spectra at a pump-probe delay of 0.5 ps,
 942 the GVD correction procedure requires a sampling with time steps <0.5 ps over the first 6 ps covering
 943 the chirp of the probe pulse. Due to the long data acquisition (DAQ) time per data point, a time step of 1
 944 ps was chosen over the duration of the probe pulse chirp instead. After GVD correction, the first TRCD
 945 spectrum completely free of contributions from the coherent artifact corresponded to a pump-probe delay
 946 of 4 ps.

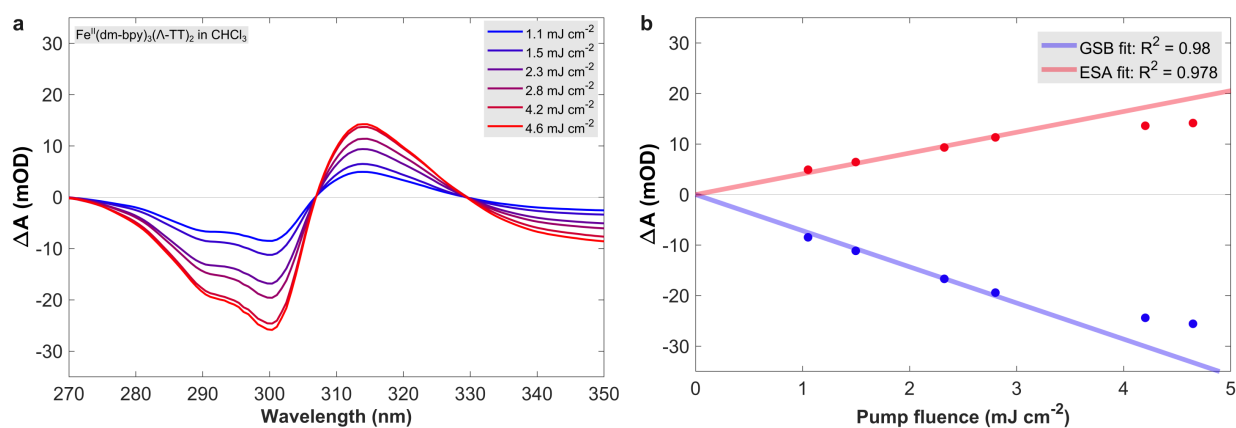


Figure S.15. a) Transient absorption of $\text{Fe}^{\text{II}}(\text{dm-bpy})_3(\Lambda\text{-TT})_2$ in CHCl_3 as a function of pump fluence at a pump-probe delay of 10 ps. b) Maximum transient absorption amplitude of the GSB and ESA band as a function of pump fluence including a linear fit of the data.

947 **Pump fluence dependence.** In order to ensure that the excitation of the MLCT transition takes place
 948 in a linear regime with respect to the pump fluence, we recorded TA spectra of Fe^{CIP} as a function of pump
 949 pulse energy. The pump-probe delay was fixed at 10 ps and the pump pulse energy E was converted to
 950 peak fluence F via $F = 8E/(w^2\pi)$, assuming a Gaussian beam with a diameter w at $1/e^2$ intensity. Here
 951 we used an average focal spot diameter of $w = 200 \mu\text{m}$. Fig. S.15a displays the acquired spectra, whereas
 952 fig. S.15b plots the maximum TA amplitude of the main GSB and ESA band averaged over a 2 nm wide

953 interval as a function of the pump fluence. One clearly observes a saturation of the TA signal for the two
954 highest fluence values. We thus performed a linear fit on the data taking into account only the four lowest
955 fluence values and setting the y-intercept to zero. We obtained an excellent correspondence with the data
956 as evidenced by the high R^2 values displayed in the figure. From this data set we estimated the maximum
957 peak fluence in the linear regime to be at 3.5 mJ cm^{-2} . For the reported TRCD experiments, we thus
958 employed a pump pulse energy of $1 \text{ }\mu\text{J}$ at an average focal spot diameter of $270 \text{ }\mu\text{m}$ at $1/e^2$ intensity in
959 order to maximize the measured TRCD signals.

960 **Measurement sensitivity.** The statistical noise of a TRCD spectrum recorded at a given pump-probe
961 delay mostly depends on the shot-noise of the probe spectrum, the accuracy of its referenced detection
962 and the number of averaged probe shots. For each TRCD experiment we determined the associated
963 standard error at a pump-probe delay of -0.1 ps (probe pulse arriving 0.1 ps before the pump pulse) as the
964 standard deviation of the measured TRCD amplitude over the number N of the acquired TRCD spectra,
965 divided by \sqrt{N} . For the TRCD experiments on the Λ configurations $N = 800$ and for those on the Δ
966 configurations $N = 600$. Fig. S.16 displays the recorded TRCD spectra with the obtained standard error
967 as a shaded area (second and third column of spectra). The data shows that for all TRCD experiments,
968 baseline deviations from zero are within $\pm 1 \cdot 10^{-5} \text{ OD}$, whereas the standard error is $< \pm 1 \cdot 10^{-5} \text{ OD}$.
969 However, it is well known that at positive pump-probe delays, the pump-induced anisotropy from the
970 photoexcited molecular ensemble may result in pronounced TRCD artifacts at signal levels exceeding any
971 artifact-free TRCD signals. Similar to TA spectroscopy, a magic angle configuration of the linear pump
972 polarization with respect to the plane of pump and probe beam propagation can be achieved^{si13, si14, si15}.
973 The precise angle depends on the static birefringence in the utilized optical elements and the polarization
974 sensitivity of the optical setup, for example through dispersive optics or polarizers^{si16, si17, si18}. As these
975 parameters are highly sensitive to the probe beam alignment and environmental conditions such as the
976 ambient temperature, we set the pump polarization prior to every TRCD experiment by minimizing the
977 TRCD signal in the racemic $\text{Fe}^{\text{II}}(\text{bpy})_3\text{Cl}_2$ in H_2O at a fixed pump-probe delay of 10 ps . Here any non-zero
978 signal must be attributed to polarization artifacts from pump-induced anisotropy. Fig. S.16 displays the
979 obtained TRCD spectra (solid red lines) associated with each of the reported TRCD experiments (first
980 column of spectra). In all cases, deviations from zero were determined to be within $\pm 1 \cdot 10^{-5} \text{ OD}$, which

981 thus represents the absolute sensitivity of the reported TRCD experiments. This highlights that TRCD
 982 measurements are typically not limited by the achievable noise floor, but by polarization artifacts. To
 983 the best of our knowledge, this is the highest measurement sensitivity that has thus far been reported for
 TRCD spectroscopy on ultrafast time scales.

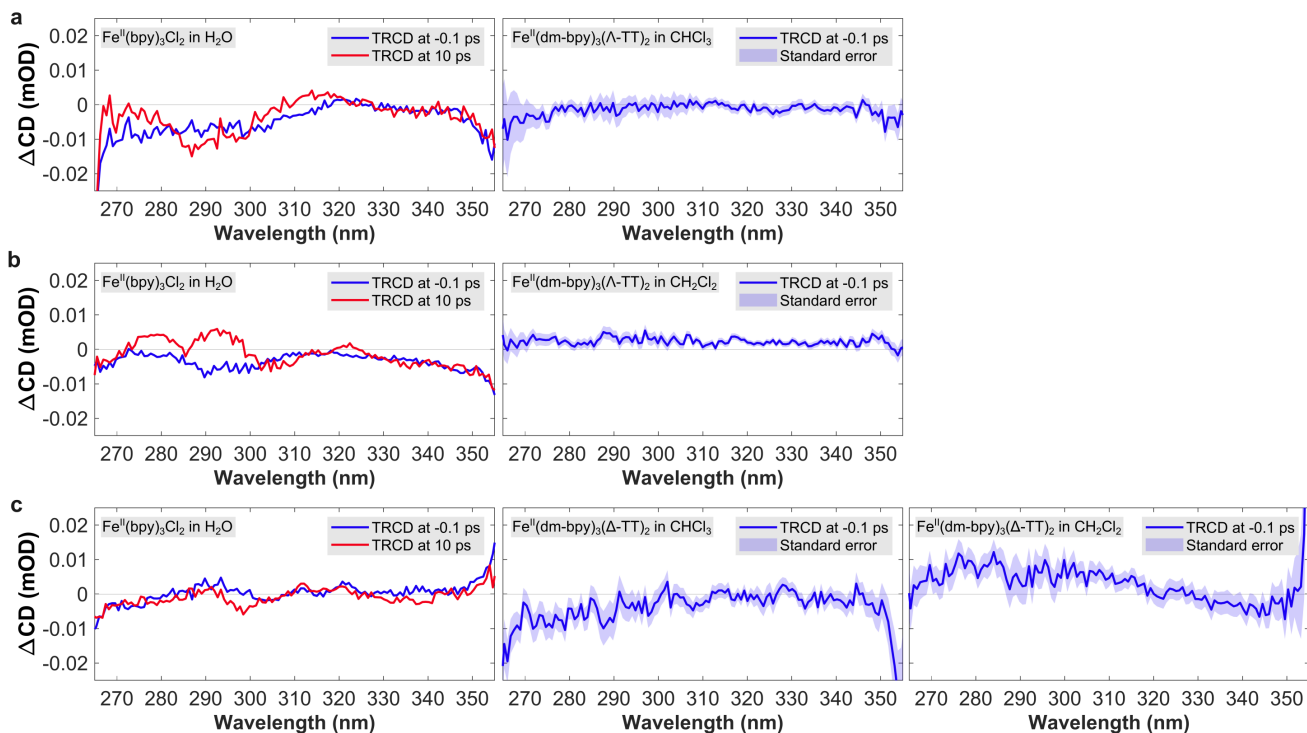


Figure S.16. Assessment of the sensitivity of the TRCD experiments and the suppression of polarization artifacts. The left-most panels display the TRCD spectrum at -0.1 ps and 10 ps for racemic $\text{Fe}^{\text{II}}(\text{bpy})_3\text{Cl}_2$ in H_2O , where any non-zero signal is attributed to polarization artifacts. These measurements were performed prior to each of the reported TRCD experiments: a) for $\Lambda\text{-Fe}^{\text{CIP}}$, b) for $\Lambda\text{-Fe}^{\text{SIP}}$, and c) for $\Delta\text{-Fe}^{\text{CIP}}$ and $-\text{Fe}^{\text{SIP}}$, which were measured back-to-back. The right panels display the TRCD spectra at -0.1 ps for each of the four samples, including the associated standard error as a shaded area.

984

985 **TRCD data.** Fig. S.17 displays the TRCD spectra of $\Lambda, \Delta\text{-Fe}^{\text{CIP}}$ and $-\text{Fe}^{\text{SIP}}$. As indicated in the
 986 Methods section, 30,000 probe shots were acquired per pump-probe delay to calculate a TRCD spectrum.
 987 For the Λ configurations, 30 pump-probe delays were recorded in a scan, which was repeated 800 times.
 988 In each scan, the chirp of the probe pulse was sampled with 1 ps steps, such that after GVD correction of
 989 the data the earliest recorded pump-probe delay free of any signal from the coherent artifact is 4 ps. Fig.
 990 S.17a,c thus displays 26 TRCD spectra with logarithmically increasing pump-probe delay, as indicated
 991 in the legend. To check the consistency of the results, the TRCD spectra for the Δ configurations were

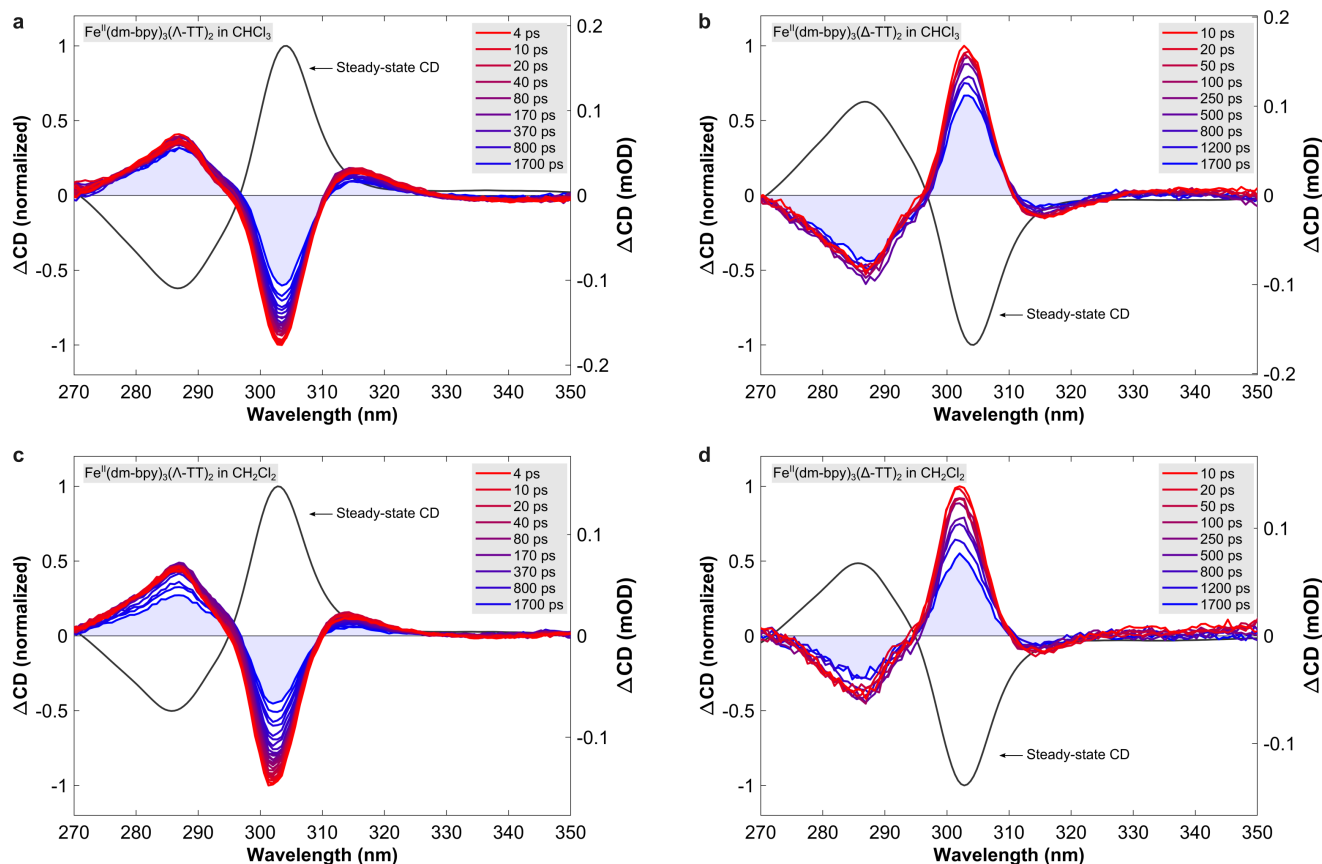


Figure S.17. TRCD spectra as a function of pump-probe delay for Λ -Fe^{CIP} (a), Δ -Fe^{CIP} (b), Λ -Fe^{SIP} (c), and Δ -Fe^{SIP} (d). For the Λ configurations a total of 26 pump-probe delays are displayed, whereas 9 pump-probe delays are displayed for the Δ configurations. For all samples, the maximum absorbance near 295 nm was approximately 0.7 OD in a 0.5 mm pathlength flow cell. The samples were photoexcited at 530 nm with a peak fluence of approximately 3.5 mJ cm^{-2} .

992 recorded at 10 pump-probe delays over 600 scans. Fig. S.17b,d displays the TRCD spectra for the 9
 993 acquired positive pump-probe delays corresponding to the values indicated in the legend. Note that the
 994 earliest pump-probe delay was 10 ps with respect to the coherent artifact at 270 nm, such that no GVD
 995 correction was performed. For all four samples, the TRCD spectra acquired at a negative pump-probe
 996 delay are displayed in fig. S.16. Starting with Λ -Fe^{CIP}, three bands can be observed: a positive GSB
 997 band centered at 285 nm, a negative GSB band centered near 305 nm, and a positive excited state CD
 998 band centered near 315 nm. Importantly, the two GSB bands do not display the same decay dynamics,
 999 which suggests that they are overlapping with an additional excited state CD band. Λ -Fe^{SIP} displays the
 1000 same GSB and excited state CD bands, but with significantly faster decay dynamics, which also results
 1001 in an observable decay of the GSB band at 285 nm. Despite its slightly reduced signal-to-noise and less

1002 recorded pump-probe delays overall, the TRCD spectra for Δ -Fe^{CIP} and Fe^{SIP} clearly display the same
1003 bands and decay dynamics as their counterparts, yet with an inverted sign, due to the inverted chiral
1004 symmetry. As TRCD spectroscopy is notoriously sensitive to polarization artifacts distorting the observed
1005 spectral dynamics, this is an important milestone. Together with the absolute sensitivity obtained from
1006 racemic samples in fig. S.16, it demonstrates that the reported TRCD experiments are not limited by
1007 polarization artifacts such that the observed spectral dynamics can be attributed safely to the molecular
1008 dynamics driving the SCO in the studied Fe^{II} complexes.

1009 **TRCD fitting procedure and HS CD evolution.** In order to develop a global fitting procedure for the
1010 TRCD data, we first determined the minimum number of Gaussians that are required to fit a representative
1011 TA and TRCD spectrum. To this end, we note that for each pump-probe delay, a TRCD measurement
1012 delivers both the TRCD spectrum and TA spectra measured with left- and right-circularly polarized probe
1013 pulses. Fig. S.18 displays the obtained data and fits for Λ -Fe^{CIP} at a pump-probe delay of 5 ps, whereas
1014 table S.4 shows the obtained fit parameters. We found that the TA spectrum can be decomposed into a
1015 GSB contribution scaled by an excitation density of $A_{\text{GSB}} = -0.1$ (10% of the molecules are excited) and
1016 a minimum of two Gaussian ESA bands. The R^2 value of the fit is excellent and the obtained fit residuals
1017 are an order of magnitude lower than the maximum TA signal. We thus attribute the dominant ESA band
1018 centered at 299.2 nm to the LC centered transition of the HS state and note that its spectral shape is well
1019 described by a single Gaussian band. For the TRCD spectrum, a successful fit requires two Gaussian HS
1020 CD bands, centered at 287.4 nm and 310.2 nm, respectively, resulting in an excitation density of 12%.
1021 This value agrees well with the excitation density obtained from the spectral decomposition of the TA
1022 spectrum, as required. Again, the R^2 value is excellent and the obtained residuals are more than an order of
1023 magnitude lower than the maximum TRCD signal. Taking into account the results from the decomposition
1024 of the TA spectrum, the obtained results are fully consistent with a scenario where the HS CD is caused by
1025 the excitonic coupling of the three LC transitions of the HS state: 1) the sign-pattern of the bisignate CD
1026 agrees with the ground state CD, and 2) its zero-crossing near 299 nm agrees very well with the center of
1027 the HS LC band obtained from the spectral decomposition of the TA spectrum. We therefore conclude
1028 that the HS CD spectrum is well described by a minimal model consisting of two Gaussian bands with
1029 opposite signs.

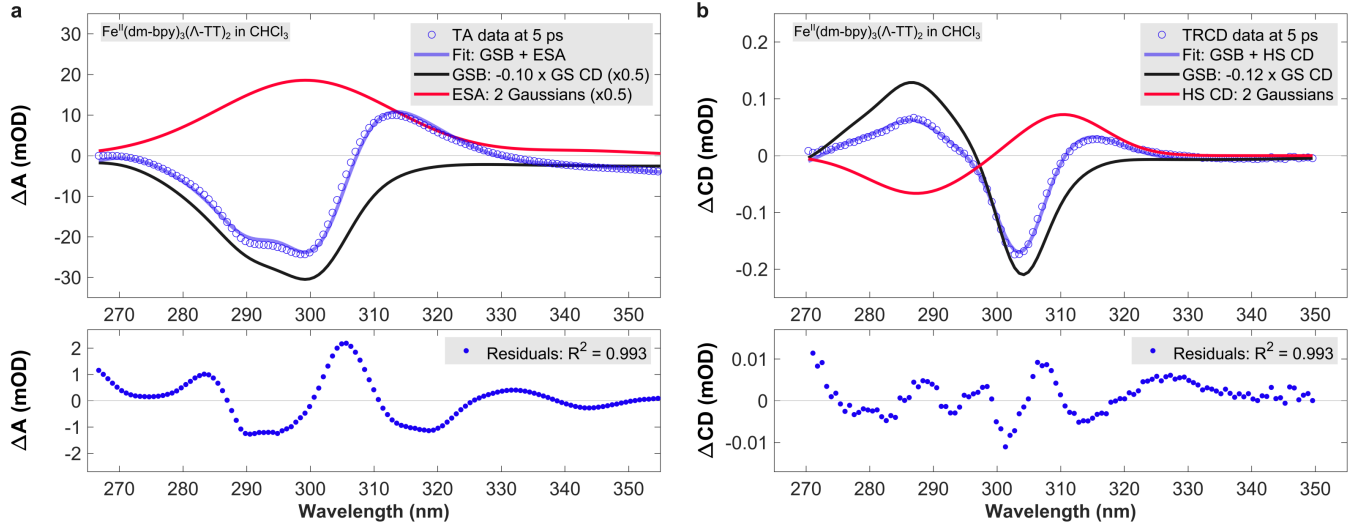


Figure S.18. Spectral decomposition of the simultaneously acquired TA (a) and TRCD (b) spectrum of Λ -Fe^{CIP} at 5 ps into a GSB and a HS state contribution consisting of Gaussian bands. Note that in (a) the GSB and ESA bands are scaled by a factor of 0.5 for a better comparison with the TA spectrum.

Spectrum	R ²	A _{GSB}	A ₁ (mOD)	λ ₁ (nm)	c ₁ (nm)	A ₂ (mOD)	λ ₂ (nm)	c ₂ (nm)
TA	0.993	-0.10	37.2	299.2	19.5	2.3	342.6	14.2
TRCD	0.993	-0.12	-0.067	287.4	10.9	0.073	310.2	9.2

Table S.4. Fit parameters obtained from the fits displayed in fig. S.18. A_n , λ_n , c_n are the amplitude, center wavelength, and width of the Gaussian functions ($n = 1, 2$) forming the ESA and HS CD.

1030 At each pump-probe delay t , we can now write the TRCD spectrum as a sum of the GSB and the
 1031 HS CD contribution. For this, we assume that the GSB takes the spectral shape of the inverted ground
 1032 state CD spectrum $CD(\lambda)$ scaled by the excitation density A_{GSB} at the earliest pump probe delay. The
 1033 time-dependent decay of the GSB is then given by the absolute value of the normalized transient absorption
 1034 $|TA_{GSB}(t)|$. The HS CD is described by two Gaussian bands, a high-energy band with the subscript h and
 1035 a low-energy band with the subscript l . A priori, all six of the resulting HS CD fit parameters may be time
 1036 dependent, resulting in the following functional form for a TRCD spectrum:

$$TRCD(\lambda, t) = -A_{GSB}|TA_{GSB}(t)|CD(\lambda) + A_h(t)\exp\left\{\left(\frac{\lambda - \lambda_h(t)}{c_h(t)}\right)^2\right\} + A_l(t)\exp\left\{\left(\frac{\lambda - \lambda_l(t)}{c_l(t)}\right)^2\right\} \quad (10)$$

1037 However, the large number of free fit parameters may distort the extracted time-dependent spectral
 1038 dynamics, if the only optimization criterion is the best fit with the data at each pump-probe delay. In

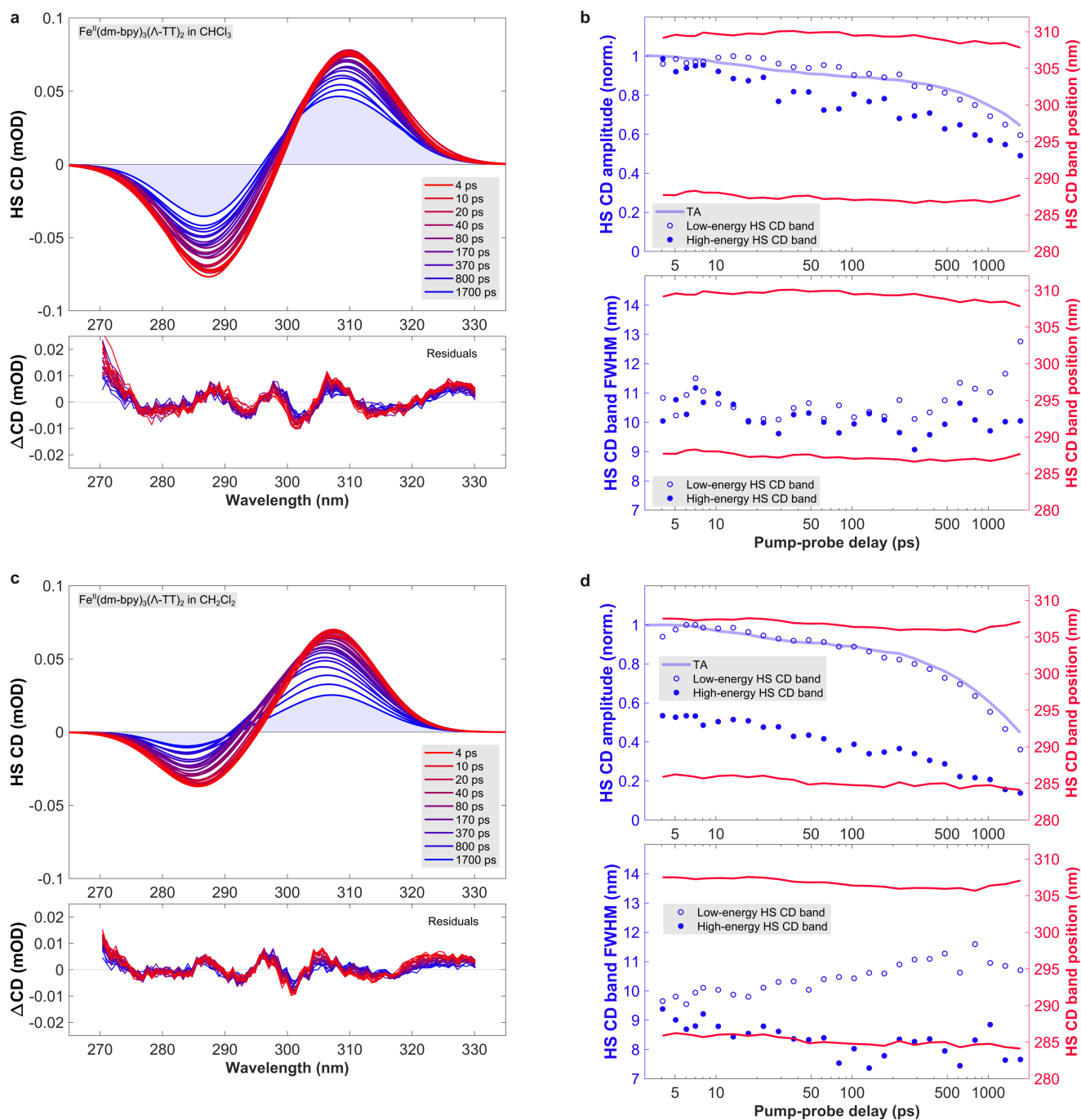


Figure S.19. Time evolution of the HS CD of Λ -Fe^{CIP} and Λ -Fe^{SIP}, obtained from a global fit of the respective TRCD data sets with all six HS CD parameters fit freely for each pump-probe delay. a, b) HS CD spectra, the associated residuals and the obtained HS CD fit parameters as a function of pump-probe delay for Λ -Fe^{CIP}, with c, d) displaying the analogous results obtained for Λ -Fe^{SIP}

1039 practice, this may for example lead to several fit parameters accounting for spectral changes that could
 1040 possibly be described accurately by the time-dependent evolution of a single parameter. In order to
 1041 determine the minimum number of time-dependent fit parameters that are required to achieve a robust

1042 fit of the recorded data sets, we first applied the developed fit function without any further constraints in
1043 order to identify trends in the spectral evolution of the HS CD. To this end, we focused on Λ -Fe^{CIP} and
1044 -Fe^{SIP}, due to their high signal-to-noise and large number of data points. Fig. S.19a,c displays the obtained
1045 HS CD spectra as a function of pump-probe delay including their respective residuals, whereas S.19b,d
1046 displays the obtained fit parameters as a function of pump-probe delay. First of all we note that for both
1047 data sets the residuals are found to be within $\pm 1 \cdot 10^{-5}$ OD for all pump-probe delays, which implies an
1048 excellent correspondence between the fit and the data. The evolution of the HS CD spectra of Λ -Fe^{CIP} is
1049 dominated by an asymmetric decay of the two HS CD bands: at the earliest pump-probe delay, the absolute
1050 amplitudes are mostly identical, whereas at the latest delay, the high-energy band has a significantly lower
1051 amplitude. Whilst the positions of the bands vary with pump-probe delay, a clear trend in their evolution
1052 is not observed. These observations are supported by the time evolution of the individual fit parameters
1053 displayed in fig. S.19b, where the HS CD band amplitudes were normalized to the maximum absolute
1054 value for better comparison. Whilst the amplitude of the low-energy HS CD band decays mostly like the
1055 TA signal (solid line), the high-energy band amplitude decays more strongly. The widths and positions of
1056 the two bands do not follow an observable trend, which suggests that these parameters may be suitable
1057 time independent constants in a constrained model fit.

1058 In direct comparison, the spectral evolution of the HS CD spectrum of Λ -Fe^{SIP} in fig. S.19c is more
1059 complex. The band amplitudes show a similar yet more pronounced evolution: at the earliest pump-probe
1060 delay, the high-energy band is already significantly weaker than the low-energy counterpart and it decays
1061 more strongly with increasing pump-probe delay. Furthermore the low-energy band displays a significant
1062 broadening at later times. Again, the time evolution of the individual fit parameters displayed in fig. S.19d
1063 supports these observations. Whilst the low-energy band amplitude follows the decay of the TA, the
1064 high-energy band amplitude displays different decay dynamics, which results in a significant reduction
1065 of the band amplitude ratio A_h/A_l . In addition, we now find a pronounced increase in the width of the
1066 low-energy band and a minor decrease in the band positions with increasing pump-probe delay. This
1067 suggests that in the case of Λ -Fe^{SIP} at least one additional time-dependent parameter is required together
1068 with the band amplitudes in order to describe the spectral evolution of the HS CD. However in both cases
1069 an asymmetric decay of the band amplitudes is observed to be the dominant effect.

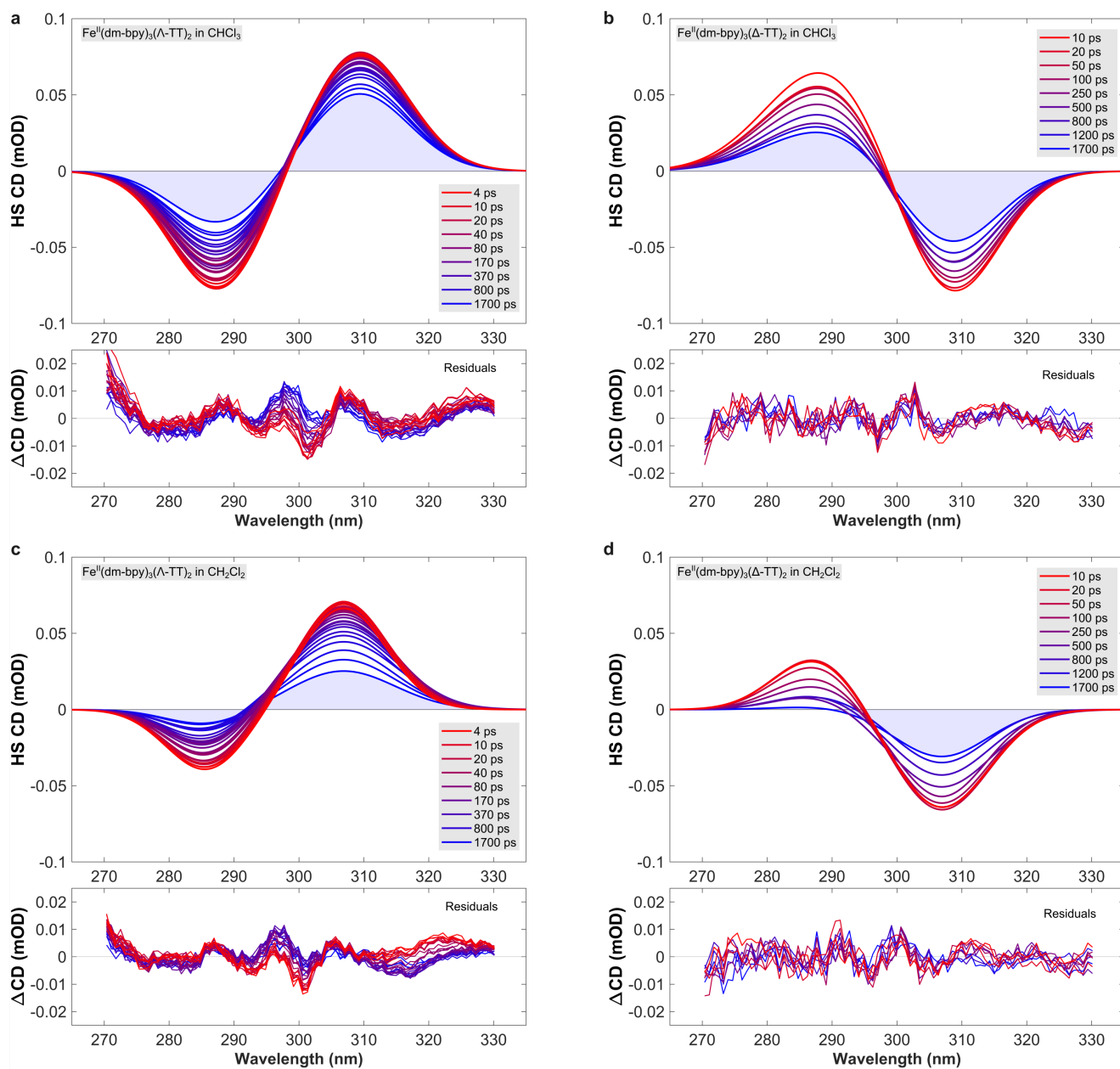


Figure S.20. Time evolution of the HS CD of Λ , Δ - Fe^{CIP} and $-\text{Fe}^{\text{SIP}}$, obtained from a constrained global fit of the respective TRCD data sets, as explained in the text. a,b) HS CD spectra and the associated residuals for Λ , Δ - Fe^{CIP} , with c,d) displaying the analogous results obtained for Λ , Δ - Fe^{SIP} .

1070 In the following we performed fits using the constrained fit functions proposed above. For Fe^{CIP} in
 1071 both its Λ and Δ configuration we obtained robust fits with $A_h(t)$ and $A_l(t)$ as the only time-dependent
 1072 fit parameters. The remaining parameters A_{GSB} , λ_h , λ_l , c_h and c_l were assumed to be constant for all
 1073 pump-probe delays and were thus fit globally across each data set. In the case of Fe^{SIP} , a fit function
 1074 with only the amplitudes as free parameters did not converge to a meaningful solution, confirming the

1075 previously made observation that the spectral dynamics are more complex compared to Fe^{CIP} . We found
1076 that robust fits could be achieved with either one of the widths as an additional time dependent parameter,
1077 with the solution employing $c_l(t)$ resulting in more robust fits across both the Λ and Δ configurations.
1078 Whilst we cannot exclude that minor a time-dependent evolution of the HS CD band positions may take
1079 place in $\Lambda, \Delta\text{-Fe}^{\text{SIP}}$, we note that it is not required for an accurate description of the data. We further stress
1080 that the observed asymmetric decay of the band amplitudes remains the dominant effect in the HS CD
1081 evolution with any additional change playing a comparatively minor role.

1082 Fig. S.20 displays the time evolution of the HS CD obtained from the constrained fits described above.
1083 For the Λ configurations of Fe^{CIP} and Fe^{SIP} we qualitatively observe the same spectral evolution as for
1084 the fit function with free fit parameters, demonstrating that the additional constraints do not distort the
1085 extracted HS CD dynamics. This is supported by the obtained residuals that display almost identical
1086 amplitudes within the range of $\pm 1 \cdot 10^{-5}$ OD, albeit with a minor time dependence. This shows that the
1087 additional constraints do not compromise the accuracy of the performed fits. As expected, the HS CD
1088 dynamics obtained for the Δ configurations display the same spectral evolution as their counterpart but
1089 with an inverted sign. Nevertheless, minor quantitative differences can be observed, which are assessed
1090 more closely in fig. S.21. Starting with Fe^{CIP} , one observes that the band positions obtained for the Λ
1091 and Δ configurations agree within ± 1.3 nm. Concerning the widths, the values obtained for c_l agree very
1092 well, whereas the values for c_h differ by about 20%. For the amplitudes, $A_l(t)$ follows the TA in both data
1093 sets, whereas $A_h(t)$ is shifted to lower values by about 20%. Whilst these are non-negligible quantitative
1094 deviations, we note that they do not have any impact on the interpretation of the experiments. In the case
1095 of Fe^{SIP} , the fit parameters obtained for the Λ and Δ configurations display an excellent correspondence.
1096 The only minor disagreement can be seen in $c_l(t)$ for the Δ configuration, which does not display a clear
1097 monotonous increase for larger pump-probe delays. We thus conclude that the spectral dynamics of the
1098 HS CD are well described by the constrained fit models, which lead to robust and consistent results across
1099 all data sets.

1100 In order to quantify the dynamics encoded in the HS CD amplitude decays, we performed multi-
1101 exponential fits on the values obtained for $A_h(t)$ and $A_l(t)$ from the constrained HS CD model fit. Fig.
1102 S.21 indicates that their time evolution contains the time-dependent decay of the the excited state given

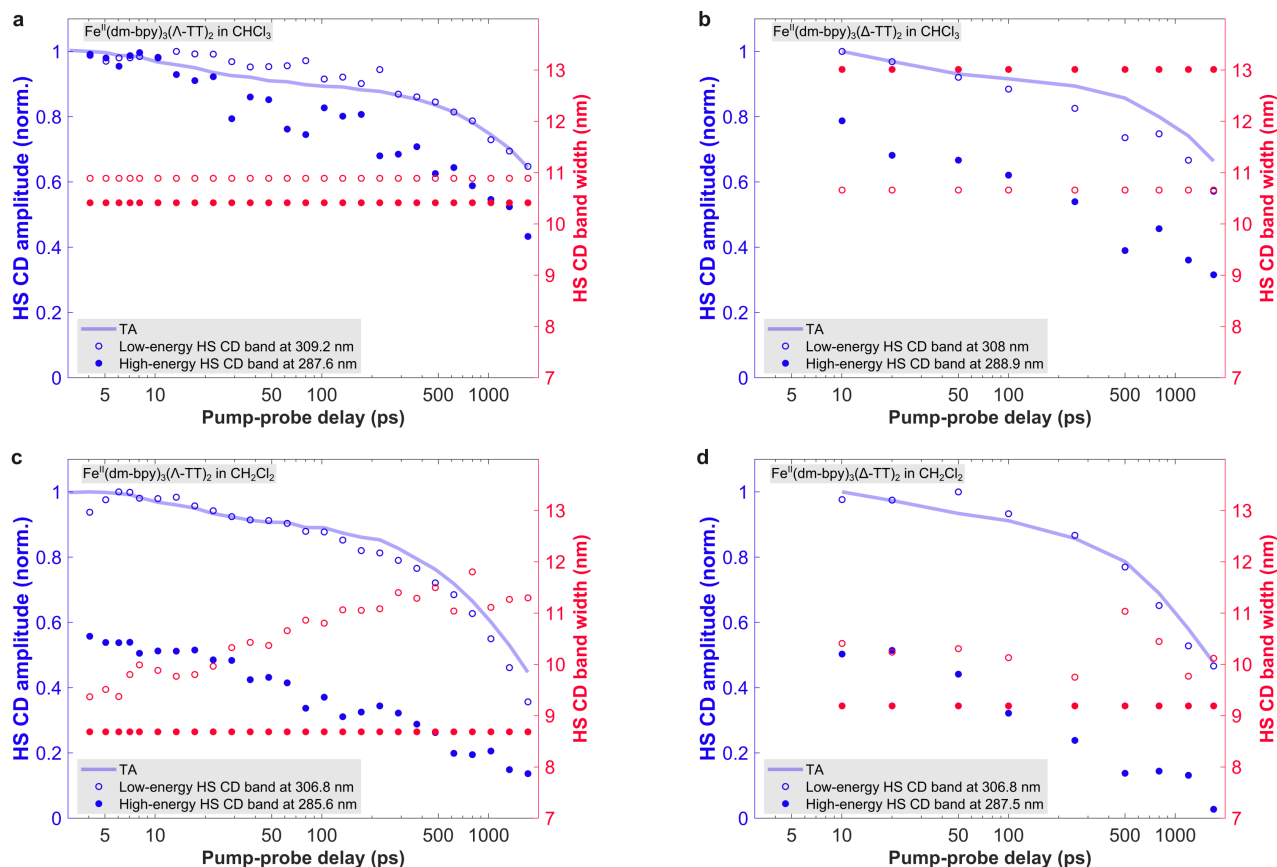


Figure S.21. Time evolution of the HS CD fit parameters of $\Lambda, \Delta\text{-Fe}^{\text{CIP}}$ and $-\text{Fe}^{\text{SIP}}$, obtained from a constrained global fit of the respective TRCD data sets, as explained in the text. a,b) Fit parameters for $\Lambda, \Delta\text{-Fe}^{\text{CIP}}$, with c,d) displaying the analogous results obtained for $\Lambda, \Delta\text{-Fe}^{\text{SIP}}$.

1103 by the TA dynamics. This is consistent with the fact that the HS CD must decay globally with the HS
 1104 state population. However, the more pronounced decay of $A_h(t)$ suggests the presence of at least one
 1105 additional decay component. On this basis, we used a fit function consisting of a sum of two exponential
 1106 decays, with one time constant fixed as τ_3 , the time constant associated with the electronic decay of the
 1107 HS state, obtained from the TA experiments. For each $\Lambda\text{-Fe}^{\text{CIP}}$ and $-\text{Fe}^{\text{SIP}}$, we simultaneously fitted $A_h(t)$
 1108 and $A_l(t)$ with this fit function, with fig. S.22 displaying the obtained fits and their residuals. We observe
 1109 an excellent agreement between the fit and the data, which is further supported by the low amplitude of
 1110 the residuals. The obtained fit parameters are displayed in table S.5. We found that the additional decay
 1111 components $\phi^{\text{CIP}} = 80 \pm 10$ and $\phi^{\text{SIP}} = 70 \pm 10$ agree within their error ranges. However, whilst their
 1112 contribution to the decay of $A_l(t)$ is about 10% for both samples, their contribution to $A_h(t)$ is significantly
 1113 more pronounced and displays a strong dependence on the ion-pairing interaction. In $\Lambda\text{-Fe}^{\text{CIP}}$, ϕ^{CIP}

1114 accounts for 28% of the decay of $A_h(t)$, whereas in Λ -Fe^{SIP}, this contribution rises to 43%.

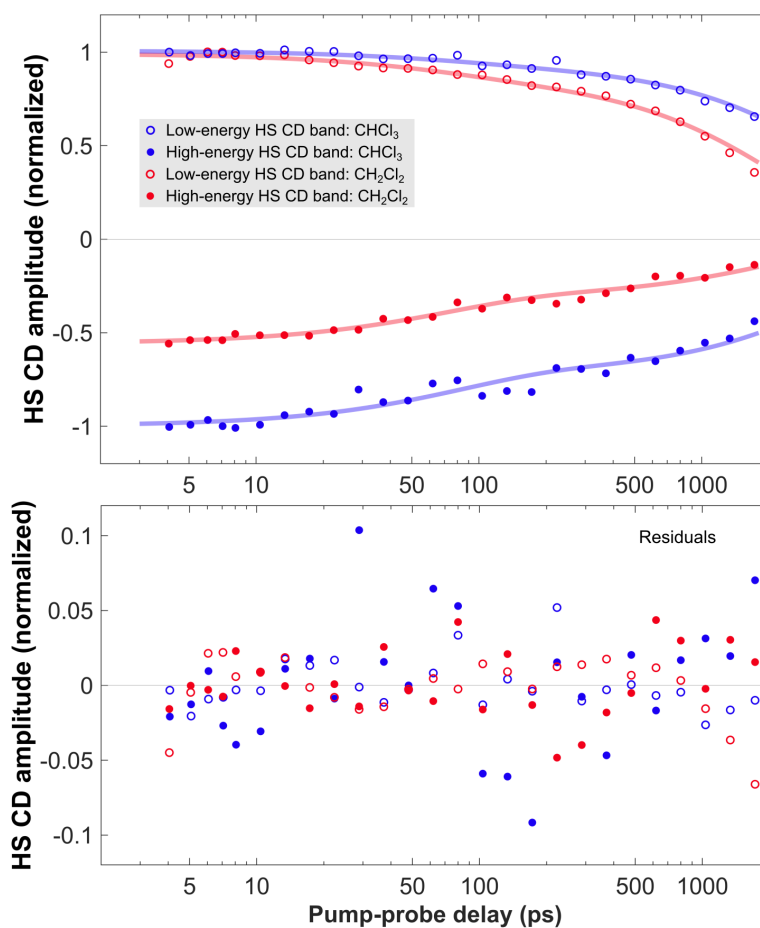


Figure S.22. Time evolution of the high- and low-energy HS CD band amplitudes for Λ -Fe^{CIP} and $-\text{Fe}^{\text{SIP}}$. The solid lines display the multi-exponential fits applied to the data points with the obtained fit parameters displayed in table S.5.

Sample	ϕ (ps)	A_l^ϕ	A_h^ϕ	τ_3 (ps)	A_l^τ	A_h^τ
Λ -Fe ^{CIP}	80 ± 10	0.07	-0.28	4970 (fixed)	0.94	-0.72
Λ -Fe ^{SIP}	70 ± 10	0.12	-0.24	2370 (fixed)	0.88	-0.32

Table S.5. Fit parameters obtained from simultaneously fitting a sum of two exponential functions to the time evolution of the high- and low-energy HS CD band amplitudes of Λ -Fe^{CIP} and $-\text{Fe}^{\text{SIP}}$.

1115 References Supporting Information

- 1116 [si1] Mason, S. F., Peart, B. J. & Waddell, R. E. Optical rotatory power of co-ordination compounds.
 1117 Part XVI. Intermediate exciton coupling in the circular dichroism of trisbipyridyl complexes. *J.*
 1118 *Chem. Soc. Dalton Transactions* **0**, 944–949, DOI: [10.1039/DT9730000944](https://doi.org/10.1039/DT9730000944) (1973). Publisher:
 1119 Royal Society of Chemistry.

- 1120 [si2] Castellucci, E., Salvi, P. R. & Foggi, P. Two-photon excitation spectra of the lowest electronic
1121 states of 2,2'-bipyridine. *Chem. Phys.* **66**, 281–291, DOI: [10.1016/0301-0104\(82\)88027-0](https://doi.org/10.1016/0301-0104(82)88027-0) (1982).
- 1122 [si3] Gawelda, W. *et al.* Ultrafast Nonadiabatic Dynamics of [FeII(bpy)3]2+ in Solution. *J. Am. Chem.*
1123 *Soc.* **129**, 8199–8206, DOI: [10.1021/ja070454x](https://doi.org/10.1021/ja070454x) (2007).
- 1124 [si4] Decurtins, S., Felix, F., Ferguson, J., Guedel, H. U. & Ludi, A. The electronic spectrum of
1125 tris(2,2'-bipyridine)iron(2+) and tris(2,2'-bipyridine)osmium(2+). *J. Am. Chem. Soc.* **5** (1980).
- 1126 [si5] Mason, S. F. The electronic spectra and optical activity of phenanthroline and dipyriddy metal
1127 complexes. *Inorganica Chimica Acta Rev.* **2**, 89–109, DOI: [10.1016/0073-8085\(68\)80016-6](https://doi.org/10.1016/0073-8085(68)80016-6)
1128 (1968).
- 1129 [si6] Bosnich, B. Application of exciton theory to the determination of the absolute configurations of
1130 inorganic complexes. *Accounts Chem. Res.* **2**, 266–273, DOI: [10.1021/ar50021a002](https://doi.org/10.1021/ar50021a002) (1969).
- 1131 [si7] Ruckebusch, C., Sliwa, M., Pernot, P., de Juan, A. & Tauler, R. Comprehensive data analysis of
1132 femtosecond transient absorption spectra: A review. *J. Photochem. Photobiol. C: Photochem. Rev.*
1133 **13**, 1–27, DOI: [10.1016/j.jphotochemrev.2011.10.002](https://doi.org/10.1016/j.jphotochemrev.2011.10.002) (2012).
- 1134 [si8] Graener, H., Zürl, R. & Hofmann, M. Vibrational Relaxation of Liquid Chloroform. *The J.*
1135 *Phys. Chem. B* **101**, 1745–1749, DOI: [10.1021/jp9624212](https://doi.org/10.1021/jp9624212) (1997). Publisher: American Chemical
1136 Society.
- 1137 [si9] Consani, C. *et al.* Vibrational Coherences and Relaxation in the High-Spin State of Aqueous
1138 [FeII(bpy)3]2+. *Angewandte Chemie Int. Ed.* **48**, 7184–7187, DOI: [10.1002/anie.200902728](https://doi.org/10.1002/anie.200902728)
1139 (2009).
- 1140 [si10] Auböck, G. & Chergui, M. Sub-50-fs photoinduced spin crossover in [Fe(bpy)3]2+. *Nat. Chem.* **7**,
1141 629–633, DOI: [10.1038/nchem.2305](https://doi.org/10.1038/nchem.2305) (2015).
- 1142 [si11] Slavov, C., Hartmann, H. & Wachtveitl, J. Implementation and Evaluation of Data Analysis
1143 Strategies for Time-Resolved Optical Spectroscopy. *Anal. Chem.* **87**, 2328–2336, DOI: [10.1021/
1144 ac504348h](https://doi.org/10.1021/ac504348h) (2015).
- 1145 [si12] Wallin, S., Davidsson, J., Modin, J. & Hammarström, L. Femtosecond Transient Absorption
1146 Anisotropy Study on [Ru(bpy)3]2+ and [Ru(bpy)(py)4]2+. Ultrafast Interligand Randomization of
1147 the MLCT State. *The J. Phys. Chem. A* **109**, 4697–4704, DOI: [10.1021/jp0509212](https://doi.org/10.1021/jp0509212) (2005).
- 1148 [si13] Che, D., Goldbeck, R. A. & Kliger, D. S. Theory of natural circular dichroism in molecules
1149 oriented by photoselection. *The J. Chem. Phys.* **100**, 8602–8613, DOI: [10.1063/1.466714](https://doi.org/10.1063/1.466714) (1994).
- 1150 [si14] Cho, M. Two-dimensional circularly polarized pump–probe spectroscopy. *The J. Chem. Phys.* **119**,
1151 7003–7016, DOI: [10.1063/1.1599344](https://doi.org/10.1063/1.1599344) (2003).
- 1152 [si15] Schott, S., Steinbacher, A., Buback, J., Nuernberger, P. & Brixner, T. Generalized magic angle for
1153 time-resolved spectroscopy with laser pulses of arbitrary ellipticity. *J. Phys. B: At. Mol. Opt. Phys.*
1154 **47**, 124014, DOI: [10.1088/0953-4075/47/12/124014](https://doi.org/10.1088/0953-4075/47/12/124014) (2014).
- 1155 [si16] Xie, X. & Simon, J. D. Picosecond circular dichroism spectroscopy: a Jones matrix analysis. *J.*
1156 *Opt. Soc. Am. B* **7**, 1673, DOI: [10.1364/JOSAB.7.001673](https://doi.org/10.1364/JOSAB.7.001673) (1990).
- 1157 [si17] Bjorling, S. C. *et al.* Analysis of optical artifacts in ellipsometric measurements of time-resolved
1158 circular dichroism. *The J. Phys. Chem.* **95**, 4685–4694 (1991).
- 1159 [si18] Oppermann, M. *et al.* Ultrafast broadband circular dichroism in the deep ultraviolet. *Optica* **6**,
1160 56–60, DOI: [10.1364/OPTICA.6.000056](https://doi.org/10.1364/OPTICA.6.000056) (2019).